

PICKUP IONS IN THE HELIOSPHERE

Dissertation
zur Erlangung des Doktorgrades
der Mathematisch-Naturwissenschaftlichen Fakultät
der Christian-Albrechts-Universität zu Kiel
vorgelegt von

ANDREAS TAUT

– Kiel, Januar 2018 –

Andreas Taut:
Pickup Ions in the Heliosphere,
© Januar 2018

ERSTER GUTACHTER (SUPERVISOR):
Prof. Dr. R. F. Wimmer-Schweingruber

ZWEITER GUTACHTER (ADVISOR):
Prof. Dr. H. Kersten

TAG DER MÜNDLICHEN PRÜFUNG:
26.03.2018

ZUM DRUCK GENEHMIGT:
26.03.2018

ABSTRACT

Particles that have been ionized from neutrals in the interplanetary space within the heliosphere are called PickUp Ions (**PUIs**). The freshly created ions are injected into the solar wind plasma with a characteristic non-Maxwellian Velocity Distribution Function (**VDF**) and carried outwards jointly with the solar wind and its embedded Interplanetary Magnetic Field (**IMF**). They mainly stem from two sources. On the one hand, interstellar **PUIs** are created from neutrals originating from the Local InterStellar Medium (**LISM**). These neutrals enter the heliosphere as an interstellar wind, because of the Sun's relative motion with respect to the **LISM**. On the other hand, inner-source **PUIs** are produced by a yet unidentified mechanism within 1 AU from the Sun.

The most likely candidates for a mechanism creating inner-source **PUIs** are related to the interaction of solar wind ions with interplanetary dust grains. The elemental composition of inner-source **PUIs** that is created by this process could be a key property to identify and understand the inner-source **PUI** production. Therefore, the composition of inner-source **PUIs** is investigated utilizing data provided by the Charge-Time-of-Flight (**CTOF**) sensor onboard the SOlar and Heliospheric Observatory (**SOHO**). Good agreement between the observed and the projected composition based on a specific production scenario could be demonstrated. Furthermore, an unexpected systematic variation of the composition as a function of solar wind speed is uncovered. This finding adds another strong restriction for possible inner-source **PUI** production mechanisms.

The interstellar wind, which constitutes the second major source for neutrals, enters the heliosphere from a defined direction and forms a symmetric flow about the Sun. As interstellar **PUIs** carry information about the velocity of their parent neutrals in their **VDF**, this symmetry can be exploited to derive the longitude of the interstellar flow by evaluating the measured **VDF**. In this thesis, we revisit a recent approach to determine this parameter from the measurement of the He⁺ **PUI VDF** with the Plasma and Suprathermal Ion Composition (**PLASTIC**) instrument on the Solar-TERrestrial RElations Observatory (**STEREO**) Ahead spacecraft. Various systematic errors of the original method are identified and removed. Additionally, an improved method to estimate the resulting errors is developed.

The **PUI VDF** has formerly been believed to be isotropic due to rapid pitch-angle scattering, but this understanding has been revised recently. Instead, it has been observed that the **VDF** of freshly injected **PUIs** exhibits an anisotropic torus structure in velocity space that strongly depends on the ambient **IMF** orientation. Utilizing **CTOF** data, we are able to confirm and complement on these observations. This anisotropy also introduces another well hidden systematic error in the determination of the interstellar flow longitude that we are able to identify. A corrected value for the interstellar flow longitude is presented, but also the limitations of the method are discussed.

ZUSAMMENFASSUNG

Pickup Ionen entstehen, wenn Neutralteilchen im interplanetaren Raum innerhalb der Heliosphäre ionisiert werden. Die frisch erzeugten Ionen werden mit einer charakteristischen Geschwindigkeitsverteilung in das Sonnenwindplasma injiziert und von diesem durch das mitbewegte interplanetare Magnetfeld hinausgetragen. Für die Neutralteilchen gibt es vorwiegend zwei Quellen. Einerseits entstehen interstellare Pickup Ionen aus Neutralteilchen, die aus dem lokalen interstellaren Medium stammen. Diese Neutralteilchen gelangen als interstellarer Wind in die Heliosphäre, da sich die Sonne relativ zum interstellaren Medium bewegt. Andererseits können Pickup Ionen auch innerhalb von 1 AU durch einen noch nicht genau identifizierten Prozess entstehen.

Wahrscheinlich entstehen die Pickup Ionen aus der inneren Quelle durch eine Wechselwirkung von Sonnenwindionen mit interplanetarem Staub. Durch diesen Prozess resultiert eine charakteristische elementare Zusammensetzung, die dabei helfen könnte den genauen Entstehungsprozess dieser Teilchen zu identifizieren und zu verstehen. Daher haben wir mithilfe des Charge-Time-of-Flight (**CTOF**) Sensors auf der SOlar and Heliospheric Observatory (**SOHO**) Raumsonde diese Zusammensetzung bestimmt. Es zeigte sich, dass unsere gemessene Zusammensetzung in guter Übereinstimmung mit der vorhergesagten Zusammensetzung ist, die aus einem der vorgeschlagenen Produktionsmechanismen resultiert. Außerdem konnte eine systematische Veränderung der Zusammensetzung in Abhängigkeit von der Sonnenwindgeschwindigkeit festgestellt werden. Diese Beobachtung schließt bestimmte Produktionsmechanismen als dominante Quelle kategorisch aus.

Der bereits erwähnte interstellare Wind strömt aus einer bestimmten Richtung in die Heliosphäre und erzeugt einen symmetrischen Fluss um die Sonne. Aus der Geschwindigkeitsverteilung von interstellaren Pickup Ionen kann man Rückschlüsse auf die Geschwindigkeit der Neutralteilchen, aus denen diese Ionen entstanden sind, ziehen. Indem nun die Symmetrie des Neutralteilchenflusses um die Sonne ausgenutzt wird, kann also mithilfe der Messung der Geschwindigkeitsverteilung von interstellaren Pickup Ionen auf die Einfallsrichtung des interstellaren Windes geschlossen werden. In dieser Arbeit greifen wir eine kürzlich veröffentlichte Methode auf, wie man mithilfe der Messung der He^+ Pickup Ionen Geschwindigkeitsverteilung mit dem Plasma and Suprathermal Ion Composition (**PLASTIC**) Instrument auf der Solar-TERrestrial RElations Observatory (**STEREO**) Ahead Raumsonde diesen Parameter bestimmen kann. Wir haben verschiedene systematische Fehler dieser Methode identifiziert und ausgebessert. Des Weiteren wurde eine verbesserte Methode zur Abschätzung der resultierenden Fehler entwickelt.

Früher wurde vermutet, dass die Geschwindigkeitsverteilung von Pickup Ionen isotrop ist, da angenommen wurde, dass Streuung effizient und auf kurzen Zeitskalen wirkt. Diese Annahme musste jedoch vor kurzer Zeit revidiert werden. Es wurde beobachtet, dass die Geschwindigkeitsverteilung von frisch injizierten Pickup Ionen einem Torus im Geschwindigkeitsraum ähnelt, dessen Orientierung

stark vom Magnetfeld am Ort der Messung abhängt. Mithilfe von [CTOF](#) Daten konnten wir diese Beobachtungen bestätigen und ergänzen. Diese Anisotropie der Geschwindigkeitsverteilung führt auch zu einem weiteren systematischen Fehler in der Bestimmung der Einfallsrichtung des interstellaren Windes. Da wir diesen Fehler identifizieren konnten, geben wir ein bereinigtes Ergebnis für die Einfallsrichtung an und diskutieren weitere mögliche systematische Fehlerquellen.

PUBLICATIONS

PEER REVIEWED JOURNALS

Composition of inner-source heavy pickup ions at 1 AU: SOHO/CELIAS/CTOF observations - Implications for the production mechanisms

A. Taut, L. Berger, C. Drews and R. F. Wimmer-Schweingruber, *Astronomy & Astrophysics*, 576:A55 (2015), DOI: [10.1051/0004-6361/201425139](https://doi.org/10.1051/0004-6361/201425139)

Challenges in the determination of the interstellar flow longitude from the pickup ion cutoff

A. Taut, L. Berger, C. Drews, E. Möbius, V. Heidrich-Meisner, D. Keilbach, M. A. Lee and R. F. Wimmer-Schweingruber, *Astronomy & Astrophysics*, accepted: 20 November 2017, DOI: [10.1051/0004-6361/201731796](https://doi.org/10.1051/0004-6361/201731796)

Short-term variability of inner-source pickup ions at 1 AU - SOHO/CELIAS observations

L. Berger, C. Drews, A. Taut and R. F. Wimmer-Schweingruber, *Astronomy & Astrophysics*, 576:A54 (2015), DOI: [10.1051/0004-6361/201425116](https://doi.org/10.1051/0004-6361/201425116)

2D He^+ pickup ion velocity distribution functions: STEREO PLASTIC observations

C. Drews, L. Berger, A. Taut, T. Peleikis and R. F. Wimmer-Schweingruber, *Astronomy & Astrophysics*, 575:A97 (2015), DOI: [10.1051/0004-6361/201425271](https://doi.org/10.1051/0004-6361/201425271)

Anisotropy of the He^+ , C^+ , N^+ , O^+ , and Ne^+ pickup ion velocity distribution functions

C. Drews, L. Berger, A. Taut and R. F. Wimmer-Schweingruber, *Astronomy & Astrophysics*, 588:A12 (2016), DOI: [10.1051/0004-6361/201527603](https://doi.org/10.1051/0004-6361/201527603)

PEER REVIEWED CONFERENCE PROCEEDINGS

Observations of the He^+ pickup ion torus velocity distribution function with SOHO/CELIAS/CTOF

A. Taut, L. Berger, P. Bochsler, C. Drews, B. Klecker and R. F. Wimmer-Schweingruber, *AIP Conference Proceedings*, 1720, 050001 (2016), DOI: [10.1063/1.4943835](https://doi.org/10.1063/1.4943835)

High-time resolution measurements of solar wind heavy ions with SOHO/CELIAS/CTOF

N. P. Janitzek, A. Taut, L. Berger, P. Bochsler, C. Drews, B. Klecker and R. F. Wimmer-Schweingruber, *AIP Conference Proceedings*, 1720, 040006 (2016),
DOI: [10.1063/1.4943817](https://doi.org/10.1063/1.4943817)

Heavy pickup ion w-spectra at 1 AU with SOHO/CELIAS/CTOF

L. Berger, C. Drews, A. Taut and R. F. Wimmer-Schweingruber, *AIP Conference Proceedings*, 1539, 386 (2013), DOI: [10.1063/1.4811066](https://doi.org/10.1063/1.4811066)

On the anisotropy of the He^+ velocity distribution function

C. Drews, L. Berger, A. Taut, T. Peleikis and R. F. Wimmer-Schweingruber, *AIP Conference Proceedings*, 1720, 090001 (2016), DOI: [10.1063/1.4943853](https://doi.org/10.1063/1.4943853)

CONTENTS

1	INTRODUCTION	1
1.1	Motivation and Structure of this Thesis	2
1.2	The Local Interstellar Medium	4
1.3	Boundary to the Heliosphere	4
1.4	The Solar Wind	6
1.4.1	Stream Interaction Regions	7
1.4.2	Coronal Mass Ejections	8
1.5	The Interplanetary Magnetic Field	8
1.6	Pickup Ions	9
1.6.1	Inner-source Pickup Ions	9
1.6.2	Interstellar Pickup Ions	13
1.6.3	Pickup Ion Velocity Distribution Functions	14
2	INSTRUMENTATION	17
2.1	The CTOF sensor onboard SOHO	18
2.1.1	SOHO	18
2.1.2	CELIAS	18
2.1.3	CTOF	19
2.1.4	Wind/MFI	24
2.2	The PLASTIC sensor onboard STEREO	25
2.2.1	STEREO	25
2.2.2	PLASTIC	26
2.2.3	IMF Data from IMPACT	29
3	COMPOSITION OF INNER-SOURCE PICKUP IONS	31
3.1	Brief Summary of the Publication	31
3.2	Publication	32
3.3	Follow-up Investigations	43
3.3.1	Identification of Mg ²⁺	43
3.3.2	Modeling of the Inner Source	45
3.3.3	Summary	47
4	THE PICKUP ION TORUS VDF OBSERVED WITH CELIAS/CTOF	49
4.1	Brief Summary of the Publication	50
4.2	Publication	50
5	THE INTERSTELLAR FLOW LONGITUDE DERIVED FROM THE PICKUP ION CUTOFF	55
5.1	Brief Summary of the Publication	57
5.2	Publication	58
5.3	Follow-up Investigations	71
5.3.1	Additional Observational Constraints	71
5.3.2	Explanation for the Observed Effect	72
5.3.3	Improved Result for λ_{flow}	78
6	CONCLUSIONS & OUTLOOK	83
	BIBLIOGRAPHY	87

LIST OF FIGURES

Figure 1	Illustration of the heliospheric boundaries adapted from Treumann and Jaroschek (2008). The supersonic solar wind flows in the light blue area; the heliosheath is displayed in cyan. The solid red line depicts the termination shock and the solid yellow line marks the heliopause. The dark blue area corresponds to the undisturbed LISM; the orange and red areas correspond to compressed interstellar plasma. The yellow arrows display the interstellar neutral flow vector \vec{v}_{ISN} ; the cyan arrows display the orientation of the interstellar magnetic field lines. The trajectories of the two Voyager spacecraft (V1 & V2) and the solar planetary system (SPS) are sketched.	5
Figure 2	Illustration of an SIR after Pizzo (1978) with in-situ data from PLASTIC and IMPACT from STEREO A showing an example SIR around DoY 193, 2007. In the sketch on the left-hand side also the Parker spiral structure of the IMF can be seen. On the right-hand side, the top three panels show 30-min mean values of the solar wind speed v_{sw} , the proton density n_p , and the proton thermal speed v_{th} all derived from Maxwellian fits of the 1 min distributions. The bottom panel shows the IMF magnitude $ B $ from the magnetometer of IMPACT. For further details about the instruments see Chapter 2. The stream interface is marked with the vertical dashed black line.	7
Figure 3	Illustration of the proposed inner-source PUI production scenarios summarized in Allegrini et al. (2005).	11
Figure 4	Illustration of the inner-source PUI production scenario proposed by Schwadron and McComas (2010). Interstellar PUIs and PUIs created by dust interactions in the Kuiper Belt charge-exchange in the heliosheath and re-enter inner heliosphere as Energetic Neutral Atoms (ENAs). The energetic neutrals can come close to the Sun and then be re-ionized creating inner-source PUIs.	12
Figure 5	Illustration of the interstellar neutral flow through the heliosphere. The heliosphere moves towards the right-hand side with respect to the LISM. Thus, neutral particles enter the heliosphere, which are deflected by the Sun's gravitational potential. Two regions with enhanced PUI flux are observed: the focusing cone on the upwind side and the crescent on the downwind side of the Sun.	14

Figure 6	<i>Left:</i> 3D representation of the velocity space trajectory (green line) of a PUI created from a neutral at rest under an IMF configuration perpendicular to the solar wind velocity within the ecliptic plane. For every other IMF orientation, the trajectory lies on the yellow spherical shell. <i>Right:</i> 2D cut of the velocity space corresponding to the ecliptic plane with the configuration on the left hand side. The intersection of the velocity space trajectory with the considered plane is displayed by the green dots. Furthermore, the main processes modifying the initial PUI VDF are illustrated.	15
Figure 7	Photograph of the CTOF sensor. The ions enter the sensor through the aperture, which is closed with the red cap. Afterwards, a 180° hemispherical electrostatic analyzer has to be passed and subsequently the ions are subjected to a post-acceleration voltage. The ToF measurement is obtained within the ToF chamber, which is behind the aperture in the picture. At the end of the ToF chamber an SSD measures the residual energy. The picture is taken from http://www.-ieap.uni-kiel.de/et/soho/celias/gallery.html	19
Figure 8	Illustration of CTOF's principle of ion detection. After the entrance of the ion through the ion-optical system (not displayed) the hemispherical E/Q filter is passed, which is followed by a post-acceleration voltage. Afterwards, the ions have to pass through a Carbon foil to enter the ToF chamber. During the passage, secondary electrons are emitted from the foil that are guided to an MCP by an electrostatic mirror. This MCP triggers the START signal of the ToF measurement. At the end of the ToF chamber the ions hit an SSD, where the residual energy is measured and again secondary electrons are emitted. These electrons are also guided to another MCP, which triggers the STOP signal.	22
Figure 9	2D histogram of the ToF in channel numbers vs. E/Q step number for 80 days of CTOF data from DoY 150 to 230, where the post-acceleration voltage was constant. The counts are normalized to the maximum of counts within each E/Q step. The dashed white lines correspond to the calibration results for various ion species. The plot is taken from Taut (2014).	23
Figure 10	Illustration of the orbits of STA and STB taken from Kaiser (2005). For STA, the mean distance to the Sun is smaller than the mean distance of Earth, which results in a shorter orbital period. Consequently, STA is ahead of Earth and, vice versa, STB is trailing Earth. Each year the angular distance between each spacecraft and Earth increases by 22°	25

Figure 11	Photograph of the PLASTIC sensor. Due to its aperture spanning almost 360° , it looks substantially different than CTOF . On top of the electrostatic analyzer, the entrance slits of the Main- and the Small-Channel of the Solar Wind Section can be seen. The picture is taken from Galvin et al. (2008)	26
Figure 12	a) Illustration of the three parts of PLASTIC 's aperture. The Solar Wind Section is pointing towards the Sun at any time. The Wide Angle Partition is divided into a partition with SSD 's (WAPSSD) and a partition without SSD 's (WAPNOSSD). Both partitions are itself divided into eight position bins, wherein two are blocked within the WAPSSD . b) Schematic illustration of the ToF chamber within the PLASTIC sensor. Similar to CTOF secondary electrons are emitted at the beginning and the end of the ToF path, which trigger the START and STOP signals of the measurement. In contrast to CTOF , the electrons are guided by a complex deflection system onto the same MCP . Both figures are taken from Drews (2013)	27
Figure 13	2D histogram of the ToF in channel numbers vs. E/Q step number for 30 days of PLASTIC data starting from 1 st June 2007. The counts are normalized to the maximum of counts within each E/Q step. The dashed white lines correspond to the calibration results for various ion species. This is analog to Fig. 9, but for PLASTIC data.	28
Figure 14	Identification of Mg^{2+} by evaluating the triple coincidence efficiency. <i>Left panel:</i> M/Q histograms of all data with $w_{\text{C}^+} > 1.1$ and sorted for counts that triggered an SSD signal with the same condition. The M/Q boxes utilized for the ion identification are illustrated. <i>Right panel:</i> Derived SSD efficiencies for C^+ , Mg^+ and the counts that we anticipate to be Mg^{2+} as singly- and doubly-charged ion.	43
Figure 15	EPREM simulation results for the C^+ (left panel) and O^+ (right panel) VDF at 1 AU from various production mechanisms compared to the measured VDF of the corresponding ion species derived from CTOF data.	45
Figure 16	Simulated C^+/O^+ abundance ratio in the speed range $0.8 < w < 1.2$ as a function of solar wind speed for various inner-source PUI production mechanisms. For comparison also the observed ratios presented in Taut et al. (2015) are displayed.	46
Figure 17	IBEX results for the flow speed, $v_{\text{isn},\infty}$, and temperature, T_{LISM} , as a function of flow longitude, λ_{flow} , from various studys. The plot is taken from Schwadron et al. (2015) . The uncertainties of the parameters (including flow latitude β_{flow}) are coupled and leave a 4D parameter tube.	56

Figure 18	Further observational constraints related to the variation of the λ_{flow} result with IMF orientation, Φ_{GC} . a) Utilizing data sorted for solar wind speed: comparatively slow solar wind ($v_{\text{sw}} < 400 \text{ km s}^{-1}$) is displayed in black, faster solar wind ($v_{\text{sw}} > 400 \text{ km s}^{-1}$) in red. b) Utilizing data sorted for IMF variability: comparatively calm IMF ($\sigma_B < 5.4^\circ$) is displayed in black, variable IMF ($\sigma_B > 5.4^\circ$) in red.	71
Figure 19	Analysis of the λ_{flow} result as a function of selected IMF orientation with two different FoVs : In black with the full FoV (all available position bins), in red a restricted FoV (position bins 12 to 20, see Fig. 20).	71
Figure 20	Velocity space sketch of the FoV of PLASTIC's SWS and its position bin resolution in azimuthal direction. Inside this FoV PLASTIC can distinguish between 32 position bins. An example of an ideal torus VDF is illustrated (torus created from neutral at rest) and the angle Φ_{GC} is depicted, which follows from the IMF orientation. Thus for IMF orientations with $0^\circ < \Phi_{\text{GC}} < 22.5^\circ$ the ideal torus VDF would fall into position bins < 16	72
Figure 21	Illustration of longitudinal transport that is supposed to lead to the observed shift of the λ_{flow} result with IMF orientation. The middle panels show velocity space sketches for two given IMF orientations. As the PUI motion is bound to the IMF , the guiding center velocities in v_y direction are positive in the white hemisphere and negative in the grey hemisphere, which leads to longitudinal transport. The coverage of the FoV of these two areas depends on the IMF orientation, which may lead to the observation of a transport effect.	73
Figure 22	Illustration of an alternative mechanism that could lead to the observed shift of the λ_{flow} result with IMF orientation, which is not related to transport. The signature, which is commonly called the torus VDF , is smeared out and it has a non-zero angular width. Due to the tangential injection velocity, the location of the torus signature varies in location. Therefore, more or less PUIs from the torus VDF are sampled depending on ecliptic longitude. The ratio of measured torus VDF and isotropic background affects the determined cutoff speed. At ecliptic longitudes, where the tangential injection speed shifts the torus more inside of the FoV (for example the green torus signature in the top middle panel) a higher cutoff speed is determined and vice versa. This introduces an asymmetry in the cutoff speeds, which leads to a shift of the determined λ_{flow}	74

Figure 23	2D He ⁺ count histograms as a function of V_r and the IMF orientation. The counts have been normalized to the maximum counts in each bin of IMF orientation. The ecliptic longitude has been restricted to $230^\circ < \lambda < 280^\circ$ and acceleration sites have been excluded from the data for both figures. The solid black line shows the cutoff speed in each IMF orientation bin determined from a tanh-fit of the histogram. a) Here, IMF orientation lying approximately within the ecliptic plane are chosen and the variation of Φ_{GC} is considered. Thus, the torus is running through the aperture in azimuthal direction (see also Fig. 20). b) IMF orientations approximately normal to the ecliptic plane are chosen and the variation of Θ_{GC} is considered. The torus is running through the aperture in latitudinal direction.	75
Figure 24	Measurements of the location of the torus VDF signature in velocity space. The panel on the left-hand side, shows the theoretical radial and tangential velocities of neutral helium at the orbit of STA as a function of ecliptic longitude calculated from Eqn. 5 of Taut et al. (2018) ($\lambda_{flow} = 75^\circ$, $v_{ISN,\infty} = 26.2 \text{ km s}^{-1}$). The top two panels show the results for the 2D He ⁺ probability density in velocity space for different IMF orientations from the analysis developed by Drews et al. (2015). The red dashed line depicts the expected orientation of the torus VDF of freshly injected PUIs. The bottom panel shows a 1D projection of the panels above for the speed range $-30 \text{ km s}^{-1} < V_r < 60 \text{ km s}^{-1}$ plotted as a function of β , the azimuthal incident angle in the solar wind frame. The red and black curve correspond to the ranges of ecliptic longitude marked in the figure on the left-hand side.	77
Figure 25	2D count histogram of He ⁺ in parallel IMF orientations ($ \Phi_{GC} > 50^\circ$) as a function of E/Q step and position bin. Furthermore accelerated He ⁺ has been excluded $V_r < 60 \text{ km s}^{-1}$ and solar wind background is suppressed.	78
Figure 26	a) Example of IMF orientation occurrences as a function of Φ'_{GC} in the range $-10^\circ < \Phi'_{GC} < 10^\circ$ for IMF fulfilling the <i>ecliptic</i> condition (see Tab. 4). For the λ_{flow} determination, it is required that every Φ'_{GC} value occurs equally often. To ensure this, time periods are excluded randomly from the data set. b) λ_{flow} result as a function of width in the Φ'_{GC} range. $\Phi'_{GC,limit} = 1^\circ$ corresponds to the range $-1^\circ < \Phi'_{GC} < 1^\circ$ and so on.	80
Figure 27	Results for λ_{flow} as a function of Φ'_{GC} . A third order polynomial is fit to the data and the $1-\sigma$ confidence interval is calculated.	81

LIST OF TABLES

Table 1	Elemental and charge state composition of the LISM taken from Frisch et al. (2011) . PPM: Parts per million, Fraction of the corresponding element in: I: Neutral state, II: Singly ionized state, III: Doubly ionized state.	4
Table 2	CTOF parameter values taken from Hovestadt et al. (1995) and Hefti (1997) . The post-acceleration voltage and the thickness of the carbon foil had to be adapted in the in-flight calibration. The values displayed here are the original values from the instrument paper and the housekeeping data before the in-flight calibration.	20
Table 3	Compilation of proposed inner-source PUI scenarios vs. observational constraints these scenarios need to explain adapted from Allegrini et al. (2005) . The table has been expanded for scenario 5 proposed by Schwadron and McComas (2010) and the three new observational constraints reported in Berger et al. (2015) , Taut et al. (2015) , and Drews et al. (2016)	48
Table 4	Conditions of the IMF angle Θ with respect to the normal direction to divide the utilized data set into two basic orientations. In the <i>ecliptic</i> case, the IMF lies approximately inside the ecliptic plane and the torus VDF intersects with this plane at two locations. In the <i>normal</i> case, the IMF is normal to the ecliptic plane and the torus VDF lies inside the ecliptic plane therefore covering all azimuthal position bins.	79
Table 5	Compilation of selected results for λ_{flow} for comparison with the results obtained in this work utilizing PUIs . All other results were obtained from direct neutral particle measurements by detectors on the IBEX and Ulysses spacecraft.	81

ACRONYMS

ACE	Advanced Composition Explorer
CELIAS	Charge, EElement, and Isotope Analysis System
CIR	Corotating Interaction Region
CME	Coronal Mass Ejection
CTOF	Charge-Time-of-Flight
DoY	Day of Year

- EMMREM Earth-Moon-Mars Radiation Environment Module
EPREM Energetic Particle Radiation Environment Module
FoV Field of View
HSTOF Highly Suprathermal Time-Of-Flight
IBEX Interstellar Boundary EXplorer
IMF Interplanetary Magnetic Field
IMPACT In-situ Measurements of Particles and CME Transients
LISM Local InterStellar Medium
MCP Micro Channel Plate
MESSENGER MErcury Surface, Space ENvironment, GEochemistry and Ranging
MFI Magnetic Field Instrument
MTOF Mass-Time-Of-Flight
PLASTIC Plasma and Suprathermal Ion Composition
PM Proton Monitor
PUI PickUp Ion
SSD Solid State Detector
SIR Stream Interaction Region
SOHO SOlar and Heliospheric Observatory
STA STEREO Ahead
STB STEREO Behind
STEREO Solar-TERrestrial RElations Observatory
STOF Suprathermal Time-Of-Flight
SWICS Solar Wind Ion Composition Spectrometer
SWS Solar Wind Section
ToF Time-of-Flight
TRIM Tracking and Range of Ions in Matter
VDF Velocity Distribution Function
WAP Wide Angle Partition
WAPSSD Wide Angle Partition with SSDs
WAPNOSSD Wide Angle Partition without SSDs

INTRODUCTION

The laboratory that this thesis is set in is the heliosphere, which is basically a plasma bubble that is carved out of the Local InterStellar Medium (**LISM**) by the solar wind emanating from the Sun. In this environment, neutral particles that originate from inside or outside of the heliosphere can be ionized, which leads to the creation of PickUp Ions (**PUIs**). These ions are then accelerated and swept outwards by the Interplanetary Magnetic Field (**IMF**) which is embedded in and co-moving with the solar wind.

PUIs are commonly distinguished based on their origin. **PUIs** created from neutrals with an origin outside of the heliosphere, more specifically in the **LISM**, are called interstellar **PUIs** ([Möbius et al., 1985](#)), while ions created from neutrals that originate from a source within the inner heliosphere are called inner-source **PUIs**. In fact, neutrals can originate from various local sources like comets or planetary bodies within the heliosphere. But there is also another source, whose nature is not completely understood, that creates neutrals globally throughout the heliosphere ([Geiss et al., 1995a](#)). In the context of this thesis, the term "inner-source" refers to the latter, global source and not the various local sources. A more explicit distinction is given in the corresponding section (Sec. [1.6](#)).

Multiple mechanisms have been proposed that were meant to explain the production of neutrals inside the inner heliosphere that are observed as inner-source **PUIs** ([Allegrini et al. \(2005\)](#) and references therein, [Schwadron and McComas \(2010\)](#)). The most promising candidates of these mechanisms involve the interaction of solar wind ions with interplanetary dust grains. However, none of these mechanisms has been able to explain all observed properties of inner-source **PUIs** conclusively. Therefore, the detailed production mechanism of inner-source **PUIs** remains puzzling and further observational constraints are required to understand this ion population.

Especially interstellar **PUIs** show a characteristic, non-Maxwellian Velocity Distribution Function (**VDF**), which is a consequence of the pickup process, where the ions are injected into the solar wind with an anisotropic initial **VDF** that has the shape of a torus in velocity space. This **VDF** is then gradually modified by various processes within the solar wind. Formerly, it has been assumed that such an anisotropic initial **VDF** in the solar wind plasma is subjected to pitch-angle scattering by self-generated waves (e.g. [Wu and Davidson \(1972\)](#)). This would lead to an instantaneous isotropization of the initial torus **VDF** ([Vasyliunas and Siscoe, 1976](#)). However, recent studies reported on persistent anisotropies observed in **PUI VDFs** ([Oka et al., 2002; Gershman et al., 2014; Drews et al., 2015](#)), which contradict such a rapid isotropization. Therefore, the evolution of the **PUI VDF** is not entirely understood to this date.

Interstellar **PUIs** can also serve as a diagnostic tool for the **LISM** as in-situ information about this medium is carried by **PUIs**. The parameters of the **LISM** are crucial to model and understand the global structure of the heliosphere and, in particular, its

boundaries. However, the derivation of **LISM** parameters from **PUI** measurements is challenging. The **PUI** flux and especially their **VDF** is modulated by the turbulent solar wind which makes it complex to reconstruct information about the **LISM** from **PUI** measurements. Recent approaches to derive the ecliptic longitude of the interstellar neutral flow vector from the **PUI** flux (Drews et al., 2012) have been shown to be influenced by a systematic error that is due to longitudinal transport of the **PUIs** along the average **IMF** (Chalov and Fahr, 1999; Quinn et al., 2016). A more recent approach by Möbius et al. (2015) which solely exploits the measured **PUI VDFs** claims to minimize such transport effects. But as mentioned above, the evolution of the **PUI VDF** is not entirely understood, which means that it is likely that also this method is affected by possible systematic errors.

1.1 MOTIVATION AND STRUCTURE OF THIS THESIS

In the investigations described within this thesis, we are aiming to find answers with respect to the following questions:

1. What is the nature of the inner source for **PUIs**?
2. What is the 3D **VDF** of **PUIs** at 1 AU and what are the implication for the stability of a torus **VDF** within the dynamic solar wind?
3. How can we utilize the **PUI VDF** to find the interstellar neutral flow longitude?

In the following sections of this chapter, the reader is introduced in more detail into the fundamental principles of heliospheric physics with respect to the study of **PUIs**. The surroundings of the heliosphere, the **LISM**, is described which also constitutes one of the sources of neutral particles within the heliosphere. The main driver that delimits the heliosphere from the **LISM** is the solar wind. The solar wind is an energetic magnetized plasma that is accelerated within the solar corona. The magnetic field which is carried with the solar wind is called the **IMF** in this thesis. After the environment, in which the studies of this thesis is set, is explained, **PUIs** itself, their two different main sources, and their characteristic **VDF** are introduced and discussed in more detail.

For all the three questions above, we make use of data provided by two Time-of-Flight (**ToF**) mass spectrometers measuring **PUIs** in-situ. These two sensors are on-board two spacecraft: the Charge-Time-of-Flight (**CTOF**) sensor on the SOlar and Heliospheric Observatory (**SOHO**), and the Plasma and Suprathermal Ion Composition (**PLASTIC**) instrument on the Solar-TERrestrial RElations Observatory (**STEREO**). In Chapter 2, these two sensors and the two spacecraft missions are described and further data sets that have been utilized are introduced.

All three questions are related to the publications presented in this thesis. Thus, we present in each chapter one publication. First, a brief summary is given followed by the publication itself. Then, an outlook including follow-up investigations is provided. While the first publication, Taut et al. (2015), strictly focuses on Question 1, both the findings from the second and third publication, Taut et al. (2016) and Taut et al. (2018) respectively, contribute to investigations related to Question 2. Then again Question 3 is solely related to the third publication and the additional material presented in this thesis.

In Chapter 3, the analysis of CTOF data to determine the composition of inner-source heavy PUIs is presented. In Sec. 1.6.1 it is indicated that the composition of inner-source PUIs has been utilized to argue for or against certain production mechanisms. Thus, a good knowledge of the inner-source PUI composition may help to distinguish between individual production mechanisms. As CTOF provides a sufficient mass-per-charge resolution combined with a large geometry factor, it is well suited for the detection of heavy PUIs. In Taut et al. (2015), we describe our analysis of the CTOF data, present results for the inner-source heavy PUI composition and draw implications for the production mechanism. In the outlook, a more detailed identification of Mg^{2+} , which was taken into account for the first time, is given. Furthermore, 1D heavy PUI VDFs are compared to simulation results provided by P. Quinn from the University of New Hampshire, who utilized the Earth-Moon-Mars Radiation Environment Module (EMMREM) (Schwadron et al. (2010)).

In Chapter 4 the PUI VDF is studied using He^+ data collected by CTOF. In the compact *Solar Wind 14* conference proceeding Taut et al. (2016), we present observations of anisotropies of the He^+ PUI VDF related to the IMF orientation that contradict the theory of a rapid isotropization after the injection of PUIs. Instead, our observations are consistent with a torus VDF whose orientation depends on the ambient IMF orientation. For this purpose, the IMF orientation had to be extrapolated from the Wind spacecraft to the position of SOHO, because SOHO itself does not carry a magnetometer.

Chapter 5 contains our investigation and improvement of a method to obtain the longitude of the interstellar neutral flow vector from the measurement of the PUI VDF introduced in Möbius et al. (2015) that is published in Taut et al. (2018). For this publication we have used data from the PLASTIC sensor onboard STEREO Ahead (STA). After the improvement of the original method, we were able to show that this method is affected by a systematic error which is related to the mix of IMF orientations, which is observed in the utilized data. In the publication itself no conclusive explanation for this systematic error is given. However, in a follow-up investigation we provide data that indicates that the orientation and location of the torus VDF in velocity space combined with a limited Field of View (FoV) of the sensor is the main driver of this systematic error. With the help of this understanding, we derive best guess values of the interstellar flow longitude.

Finally, all findings of this thesis are summarized and evaluated in the context of current research. An outlook discussing future research in PUI related heliospheric physics completes this thesis.

1.2 THE LOCAL INTERSTELLAR MEDIUM

The [LISM](#) is the partially ionized magnetized plasma which surround the heliosphere. It has a temperature of $T_{\text{LISM}} \approx 7000$ K and a density of $n_{\text{LISM}} \approx 0.3 \text{ cm}^{-3}$ ([Frisch et al., 2011](#)). Direct neutral atom measurements performed by the Interstellar Boundary EXplorer ([IBEX](#)) obtain a relative motion of $v_{\text{ISN}} = (25.4 \pm 1.1) \text{ km s}^{-1}$ in the direction of $\lambda_{\text{flow}} = (75.6 \pm 1.4)^\circ$ in ecliptic longitude and $\beta = (-5.12 \pm 0.27)^\circ$ in latitude ([Schwadron et al., 2015](#)).

Compared to the inner heliosphere, the [LISM](#) has a substantially different elemental and ionic composition, which is displayed in Tab. 1. The [LISM](#) is not of solar origin, which is reflected in the elemental composition. The ionization state is of course dominated by the low ionization rates which result from the very low radiation intensity. Hydrogen, helium, nitrogen, and oxygen are most abundant in their neutral state, while especially carbon, magnesium, and silicon exist almost exclusively in an ionized state ([Frisch et al., 2011](#)).

The magnetic field embedded in the [LISM](#) has a strength of $B_{\text{LISM}} \approx 0.2 - 0.3 \text{ nT}$ and is tilted about 60° with respect to the ecliptic plane, which can be inferred from IBEX measurements (utilizing the ribbon feature, see [Schwadron et al. \(2009\)](#)) or radio emission and energetic particle measurements performed by the Voyager spacecraft ([Opher et al., 2007](#)).

Table 1: Elemental and charge state composition of the [LISM](#) taken from [Frisch et al. \(2011\)](#).
 PPM: Parts per million, Fraction of the corresponding element in: I: Neutral state,
 II: Singly ionized state, III: Doubly ionized state.

Element	PPM	I	II	III
H	10^6	0.776	0.224	-
He	10^5	0.611	0.385	$4.36 \cdot 10^{-3}$
C	661	$2.68 \cdot 10^{-4}$	0.975	0.0244
N	46.8	0.720	0.280	$8.52 \cdot 10^{-5}$
O	331	0.814	0.186	$4.71 \cdot 10^{-5}$
Ne	123	0.196	0.652	0.152
Na	2.04	$1.47 \cdot 10^{-3}$	0.843	0.155
Mg	6.61	$1.98 \cdot 10^{-3}$	0.850	0.148
Si	8.13	$4.21 \cdot 10^{-5}$	0.999	$8.02 \cdot 10^{-4}$

1.3 BOUNDARY TO THE HELIOSPHERE

The space that is dominated by the solar wind plasma is called the heliosphere. In Fig. 1 an illustration of the boundaries of the heliosphere is given. They are described from inward to outward in the following.

The solar wind in the inner heliosphere flows at supersonic speed, which means that it moves faster than the propagation speed of any disturbance. However, at some point the solar wind must be decelerated to subsonic speeds as it approaches the [LISM](#). The consequence is the formation of the so-called termination shock.

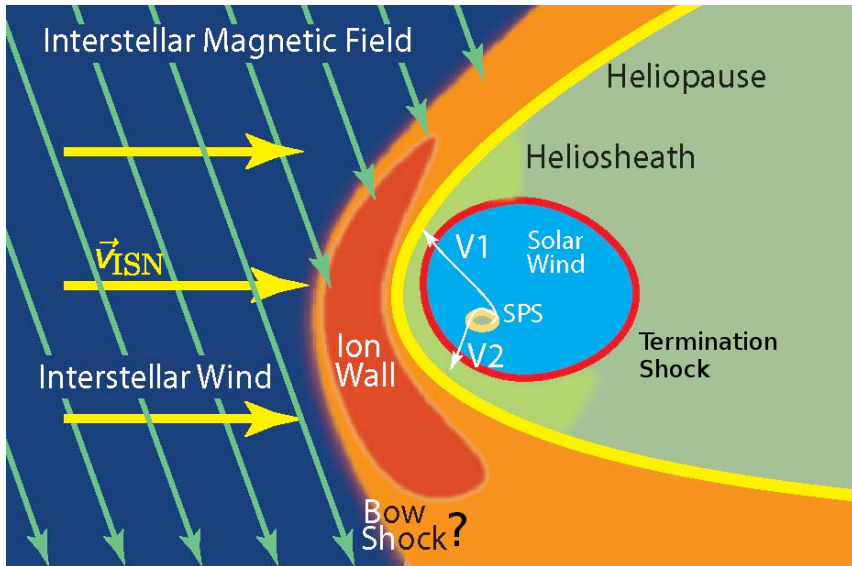


Figure 1: Illustration of the heliospheric boundaries adapted from Treumann and Jaroschek (2008). The supersonic solar wind flows in the light blue area; the heliosheath is displayed in cyan. The solid red line depicts the termination shock and the solid yellow line marks the heliopause. The dark blue area corresponds to the undisturbed LISM; the orange and red areas correspond to compressed interstellar plasma. The yellow arrows display the interstellar neutral flow vector \vec{v}_{ISN} ; the cyan arrows display the orientation of the interstellar magnetic field lines. The trajectories of the two Voyager spacecraft (V1 & V2) and the solar planetary system (SPS) are sketched.

Voyager 1 passed through the termination shock in Dec. 2004 at a distance of about 94 AU (Stone et al., 2005), while Voyager 2 crossed the termination shock in late August 2007 at a distance of about 84 AU (Stone et al., 2008), which implies that the distance of the termination shock is not constant with time and location.

Beyond this shock the solar wind is compressed and heated. This region is commonly called the heliosheath. Due to the relative motion of the heliosphere through the LISM the dynamic pressure exerted by the LISM creates an asymmetry: the heliosheath is thinner in the direction of relative motion than in the opposite direction, where a comet-like tail might be created. However, the shape of the heliosphere is still subject to current research (see e.g. Galli et al. (2017); Dialynas et al. (2017)) and alternative models (e.g. a "croissant-shaped" heliosphere) have already been proposed (Opher et al., 2016).

The outermost boundary of the heliosphere is the heliopause, which marks the end of the solar wind's influence. As two magnetized plasmas cannot permeate each other, the LISM plasma is also compressed forming an ion wall due to the relative motion. The existence of a bow shock in the LISM is still under debate (e.g. McComas et al. (2012); Scherer and Fichtner (2014); Ratkiewicz and Kotlarz (2016)). For the existence of such a shock, the interstellar flow speed must exceed the magnetosonic speed in the LISM. The magnetosonic speed, v_{mgs} in the LISM can be calculated by (see e.g. Scherer and Fichtner (2014)):

$$v_{\text{mgs}}^2 = \frac{1}{2} \left[v_A^2 + v_s^2 \pm \sqrt{(v_A^2 + v_s^2)^2 - 4v_A^2 v_s^2 \cos \theta} \right], \quad (1)$$

with v_A and v_s being the Alfvén- and the sound-speed, which can be approximated considering a proton-electron plasma by:

$$v_A = \frac{B_{\text{LISM}}}{\sqrt{4\pi n_p m_p}} \quad (2)$$

$$v_s^2 = \frac{\gamma k T_{\text{LISM}}}{m_p}. \quad (3)$$

Equation 1 obtains the speed of fast (+) and slow (−) magnetosonic waves. The angle θ denotes the angle between the magnetic field and the wave's propagation direction, n_p and m_p are the proton density and mass, $\gamma = \frac{5}{3}$ and k is the Boltzmann constant. Thus, the magnetosonic speed in the LISM apparently depends on the magnitude of the embedded magnetic field, B_{LISM} , the proton density, n_p , and temperature T_{LISM} . As the LISM actually is a multi-component plasma, additional terms considering the other ion species would need to be added in Eqn. 2 and 3. Additionally, to decide whether a shock evolves or not, the flow speed v_{ISN} needs to be compared to the magnetosonic speed. So far, all these parameters have not been determined with sufficient precision, which does not allow a firm statement about the existence of this shock.

1.4 THE SOLAR WIND

The solar wind is the continuous, supersonic stream of plasma emerging from the Sun which fills and creates the heliosphere. In this thesis, only a phenomenological summary of the solar wind is given. For more detailed information about the origin and the acceleration of the solar wind and solar wind models the reader is referred for example to [Aschwanden \(2006\)](#), [Geiss et al. \(1995b\)](#), and [Cranmer \(2012\)](#).

The solar wind mainly consists of $\sim 97\%$ H^+ and $\sim 3\%$ He^{2+} ([Bochsler and Murdin, 2000](#)). Additionally, it contains a small fraction of heavy ions ($\sim 0.1\%$). The mean composition of the solar wind (excluding H^+) determined by [von Steiger et al. \(2000\)](#) and [Shearer et al. \(2014\)](#) is given in Tab. 4 of [Taut et al. \(2015\)](#) and in Chapter 3 of this thesis. Furthermore, the charge states and the VDF of these heavy ions can be used to investigate the dynamic processes that accelerate the solar wind ([Bochsler, 2007](#)).

Historically, the solar wind has been classified in terms of speed into the slow solar wind and the fast solar wind (e.g. [Bame et al. \(1977\)](#)). The slow solar wind has bulk speeds of $v_{\text{sw}} \approx 400 \text{ km s}^{-1}$ a proton density of $n_p \approx 6 \text{ cm}^{-3}$ and a proton temperature of $T_p \approx 10^5 \text{ K}$. The origin of the slow solar wind is not completely understood to this date. In contrast to that, the fast solar wind is believed to originate in coronal holes with open magnetic field lines. The fast solar wind has typical speeds of $v_{\text{sw}} \approx 700 \text{ km s}^{-1}$, is with $n_p \approx 2 \text{ cm}^{-3}$ less dense, and with $T_p \approx 2.5 \cdot 10^5 \text{ K}$ significantly hotter than the slow solar wind ([Ebert et al., 2009](#)). Due to the different origins of fast and slow solar wind that are related to different coronal temperatures, also the charge state composition of slow and fast solar wind is substantially different ([Geiss et al., 1995b](#)). Anyhow, in the light of recent observations the historical categorization into two solar wind types seems to be oversimplified as the categorization into solar wind types and their corresponding origins appear to be more complex (e.g. [Xu and Borovsky \(2015\)](#) and references therein).

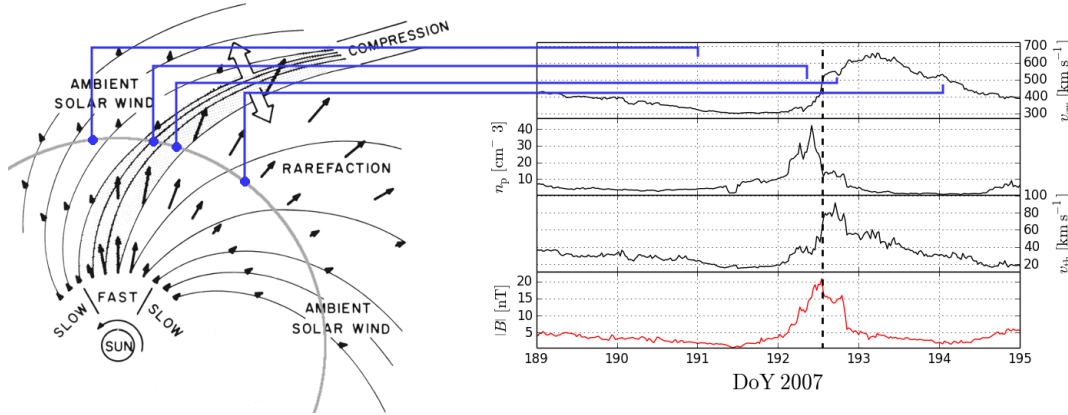


Figure 2: Illustration of an **SIR** after Pizzo (1978) with in-situ data from **PLASTIC** and **IMPACT** from **STEREO A** showing an example **SIR** around DoY 193, 2007. In the sketch on the left-hand side also the Parker spiral structure of the **IMF** can be seen. On the right-hand side, the top three panels show 30-min mean values of the solar wind speed v_{sw} , the proton density n_p , and the proton thermal speed v_{th} all derived from Maxwellian fits of the 1 min distributions. The bottom panel shows the **IMF** magnitude $|B|$ from the magnetometer of **IMPACT**. For further details about the instruments see Chapter 2. The stream interface is marked with the vertical dashed black line.

1.4.1 Stream Interaction Regions

The speed of the solar wind plasma which emerges from the Sun is variable and the Sun itself rotates. A consequence of this is, that solar wind plasma originating from different locations on the Sun may interact. For example, if a stream of slow solar wind is followed by a stream of fast solar wind, the fast solar wind will run into the slow solar wind at some point. This situation is sketched in Fig. 2 and in-situ solar wind parameters are shown for such a situation. Both streams constitute a magnetized plasma, which means that they cannot penetrate each other as magnetic field lines cannot be crossed. The result of this process is a compression of both the fast wind and the slow wind stream, which is commonly called a Stream Interaction Region (**SIR**). After this compression, a rarefaction region with decreasing solar wind speed and low proton density follows. These compression regions can be stable for several solar rotations. **SIRs** which persist for more than one solar rotation are also called Corotating Interaction Regions (**CIRs**).

In the observable solar wind parameters, **SIRs** can be identified by a set of conditions (Jian et al., 2006). First, the solar wind speed must be continuously increasing as this is the fundamental condition for such a region to form. In the solar wind density and **IMF** magnitude also a steep increase is observed, which is due to the compression of the plasma, which also leads to heating. All this leads to a characteristic signature of the total perpendicular pressure, P_t , as a function of observation time. This pressure can be estimated as:

$$P_t = \frac{B}{2\mu_0} + \sum_i n_i k T_{\perp,i} . \quad (4)$$

In this equation B is the ambient **IMF** magnitude, μ_0 is the vacuum permeability, n_i is the particle density of the various particle species (mainly protons, α particles,

and electrons), and k is the Boltzmann constant. The temperature of the particle species perpendicular to the magnetic field is denoted with $T_{\perp,i}$.

At the stream interface, which reflects the boundary between the slow and fast plasma stream (Gosling et al., 1978), this pressure reaches a maximum. The pattern of P_t together with a continuously increasing solar wind speed can be used to identify an SIR. Next to these criteria, also the entropy of the plasma or the charge state composition can be utilized to identify an SIR and, in particular, the stream interface (Wimmer-Schweingruber et al., 1997; Pagel et al., 2004).

1.4.2 Coronal Mass Ejections

Coronal Mass Ejections (CMEs) are impulsive ejections of plasma from the solar corona into interplanetary space. They are often but not always related to the presence of a solar flare, which is a sudden increase in radiation intensity on the Sun's photosphere (Gosling et al., 1975). These phenomena occur due to local disturbances within the solar magnetic field. By the reconnection of twisted magnetic field lines, large amounts of energy can be released that result in such an impulsive release of plasma and magnetic field into the interplanetary medium (Chen, 2011). The frequency of these events depends on solar activity: the more active the Sun is, the more CMEs are commonly observed (see e.g. Cane and Richardson (2003)).

CMEs that move faster than the ambient magnetosonic speed cause a shock wave within the solar wind plasma. Shock waves itself are known to be efficient accelerators of suprathermal ions including PUIs due to first-order Fermi acceleration (e.g. Lee et al. (2012)).

1.5 THE INTERPLANETARY MAGNETIC FIELD

According to Alfvén's theorem (Alfvén, 1942), the magnetic field lines of the Sun are frozen-in into the highly conductive solar wind plasma. Consequently, the Sun's magnetic field is swept outwards by the solar wind, which fills the heliosphere with the IMF.

In the absence of magnetic reconnection, this has the consequence that the IMF lines always stay connected to their corresponding footpoints on the Sun. As the Sun itself performs a rotation with a period of ~ 24.5 days at its equator, this leads to a characteristic structure of the IMF throughout the heliosphere called the Parker spiral (see also Fig. 2). Of course, this structure varies with solar wind speed. The so-called Parker angle of the IMF with respect to the radial direction in the ecliptic plane, Φ_P , can be calculated by:

$$\tan(\Phi_P) = \frac{\omega R}{v_{sw}} \quad (5)$$

Here, ω denotes the angular speed of the Sun's rotation and R is the heliocentric distance. For slow and fast solar wind this yields a Parker angle at 1 AU of about 45° and 30° , respectively. For larger heliocentric distances the Parker angle approaches 90° . Due to fluctuations of the IMF and turbulence within the dynamic solar wind, the Parker angle only corresponds to the average IMF and in general,

every IMF orientation may be possible at 1 AU. However, IMF orientation near the Parker angle occur more frequently (e.g. Forsyth et al. (1996)).

1.6 PICKUP IONS

In general, PUIs are former neutrals that become ionized inside the heliosphere. Neutrals inside the heliosphere are only subjected to gravitational forces and radiation pressure and thus do not feel any of the electromagnetic forces exerted by the solar wind. This changes immediately after the neutral is ionized. Due to the Lorentz force, the freshly created ion interacts with the IMF that is embedded in the solar wind, which leads to a gyration about the field line. As the field line, which is bound to the solar wind plasma, moves itself with solar wind speed, the ion is accelerated and swept outwards. The term *pickup ion* is due to this process: the solar wind is literally picking up the newly created ion.

The neutrals mainly originate from two global sources: the interstellar medium (Sec. 1.6.2) and an inner source, which is believed to be close to the Sun and is most likely related to the interaction of solar wind ions and interplanetary dust but up to date is still not fully understood (Sec. 1.6.1). Next to these sources, there are multiple local point-like sources like comets (Gloeckler et al., 2000b) or planets (Grünwaldt et al., 1997) that can also inject neutrals into interplanetary space that can be observed as PUIs. However, this thesis focuses on the global neutral particle sources.

The neutrals can become ionized by multiple processes (see e.g. Bzowski et al. (2013) and references therein):

- Photoionization by solar extreme ultra-violet radiation.
- Charge-exchange with solar wind protons, which results in an energetic neutral H atom and a PUI.
- Electron impact ionization.

One can distinguish PUIs from solar wind ions by a set of characteristics. Firstly, for elements heavier than hydrogen one can distinguish PUIs from solar wind ions by their almost exclusive single charge state (e.g. He⁺, C⁺, O⁺ etc.). Solar wind ions originating from the Sun that are accelerated through the hot corona are usually highly charged or fully stripped of electrons (e.g. He²⁺, C⁵⁺, O⁶⁺ etc.). Secondly, the pickup process results in a characteristic non-Maxwellian VDF (Sec. 1.6.3) that is clearly distinguishable from every solar wind VDF. Thus, also pickup protons can be identified (Schwadron et al., 2000). Lastly, the spatial density pattern (see Sec. 1.6.2) of interstellar PUIs is a clear indicator that these ions cannot be of solar origin (e.g. Möbius et al. (1995), Drews et al. (2010)).

1.6.1 Inner-source Pickup Ions

The inner source of PUIs is not completely understood to this date. In Geiss et al. (1995a) the observation of a globally distributed population of C⁺ PUIs marked the discovery of the so-called inner-source PUIs. As carbon is almost exclusively charged within the LISM (see Tab. 1), only a very small fraction of neutral carbon

atoms can penetrate into the heliosphere. However, it was found that the abundance of carbon to oxygen PUIs is approximately the same ($O^+/C^+ \approx 1$), which means that there has to be at least one other dominant global source for neutrals somewhere in the inner heliosphere.

Inner-source PUIs have been studied with the help of multiple spacecraft and instruments since then and various production mechanisms for inner-source neutrals have been proposed. Allegrini et al. (2005) summarizes the characteristics identified up to this date:

1. a composition similar to the solar wind (Gloeckler et al., 2000a; Allegrini et al., 2005),
2. a VDF, which is similar to a thermal distribution peaked at $w \approx 1$ (Geiss et al., 1995a; Schwadron et al., 2000),
3. a global production rate in the order of $2 \cdot 10^6 \text{ g s}^{-1}$ (Geiss et al., 1995a),
4. a randomly distributed flux (Geiss et al., 1995a; Allegrini et al., 2005),
5. no systematic flux variation with the solar cycle (Allegrini et al., 2005).

It has been argued that Characteristic 1 indicates that somehow the solar wind must be involved in the production of the neutrals. Characteristic 2 has commonly been assigned to a source close to the Sun, so that the PUIs had sufficient time to thermalize with the solar wind plasma. However, for this argument the implicit assumption that the PUIs are created from neutrals approximately at rest compared to the solar wind speed has been made. A consequence of Characteristic 3 is, that the process creating the neutrals must be comparatively efficient, while Characteristic 4 indicates that the source must be randomly distributed around the Sun. Finally, Characteristic 5 suggests that solar activity related phenomena like CMEs do not affect the inner source PUI flux. Recently, three new characteristics have been added that any scenario describing the inner source neutral production must fulfill: Berger et al. (2015) found that the inner-source O^+ flux is significantly correlated with the solar wind O^{6+} flux. This finding strongly indicates that the solar wind itself must be the primary source of the inner-source neutrals. Another newly found property is a systematic variability with solar wind speed that has been observed in the inner-source composition in Taut et al. (2015). The implications of this finding are more complex and will be discussed in Sec. 3.3.2. Finally, a very recent result from Drews et al. (2016), who investigated the anisotropy of heavy PUI VDFs with respect to the IMF orientation, suggests that a fraction of C^+ must be produced locally at 1 AU.

Allegrini et al. (2005) also discuss the production mechanisms that have been proposed to this date. In Fig. 3 an illustration of each scenario is displayed:

1. Solar wind recycling (Gloeckler et al., 2000a; Schwadron et al., 2000): Solar wind ions are implanted into dust grain near the Sun until the dust is saturated with solar wind ions. Then, the neutralized atoms are released into interplanetary space again, where they can be ionized and picked up by the solar wind.

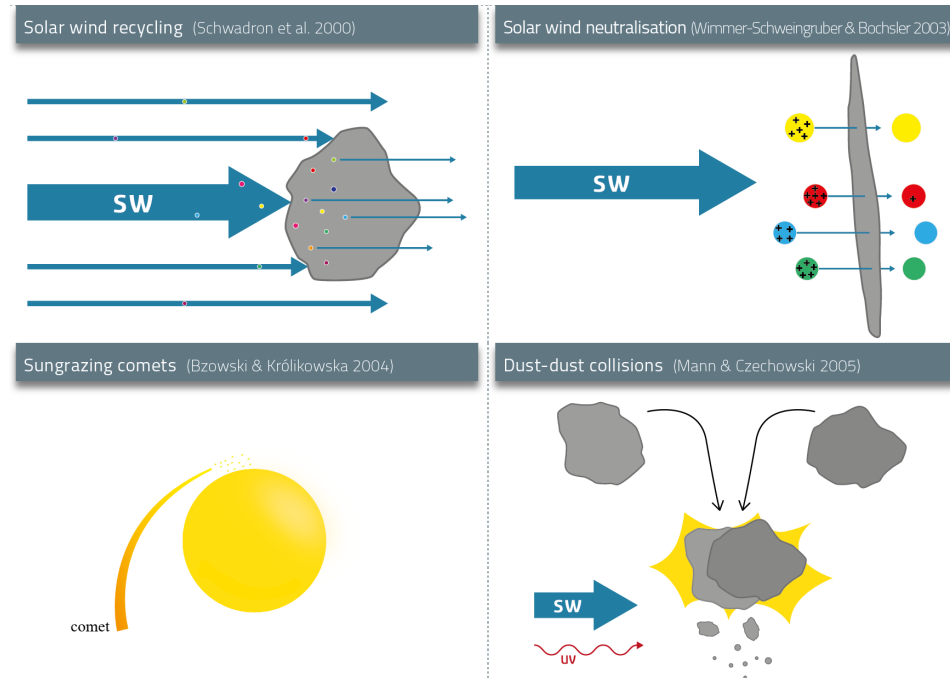


Figure 3: Illustration of the proposed inner-source PUI production scenarios summarized in Allegrini et al. (2005).

2. Solar wind neutralization (Wimmer-Schweingruber and Bochsler, 2003): Solar wind ions penetrate through tiny, nanometer-sized dust grains. During the passage, they lose (most of) their charge and a fraction of their energy.
3. Sungrazing comets (Bzowski and Królikowska, 2005): Comets can pass close to the Sun, where they can release neutral material or even dismantle completely. This material may serve as the neutral source population of inner-source PUIs.
4. Dust-dust collisions (Mann and Czechowski, 2005): While spiraling inward towards the Sun, interplanetary dust grains undergo a cascade of collisions. At some point, collisional vaporization may produce heavy neutrals in the interplanetary medium that can be ionized.

None of these scenarios can conclusively explain all observed features of inner-source PUIs. Scenario 3, which is the only scenario not related to interplanetary dust, would not result in an elemental composition similar to the solar wind as the composition of comets is observed to be substantially different (e.g. Bockelée-Morvan (2011)). Furthermore, the observation of a randomly distributed flux is highly unlikely within this scenario. Scenario 4 also fails in the expectation of a solar wind like elemental composition of inner-source PUIs. Interplanetary dust grains are supposed to show a strong enrichment in carbon and silicon and very low abundances of volatile elements like neon (Anders and Grevesse, 1989). In Scenario 1 and 2 the solar wind itself is the primary source of the inner-source neutrals, which is why an elemental composition similar to the solar wind is expected. It is not necessarily equal to the solar wind composition as the different ionization probabilities of the various elements may alter the observed inner-source composi-

tion. Anyhow, Scenario 1 is a comparatively inefficient process, which means that an inner-source PUI production rate about two orders of magnitude below the observed rate is expected. Also in this scenario sputtering of the dust itself may play a role, which would strongly favor the production of C⁺ and O⁺ ions. Scenario 2 requires tiny nanometer-sized dust particles that are believed to get trapped and swept outwards with CMEs as dust particles also acquire a charge with time. Consequently, it is argued that a solar cycle dependence of the inner-source PUI flux would be expected from this scenario.

In summary, it is likely that the production mechanism of inner-source PUIs is somehow connected to interplanetary dust, as Scenario 1 clearly fails to predict two of the key observations. The problem with the implications of the dust-related scenarios is that the nature of the interplanetary dust population is not sufficiently understood and quantified. For example, for Scenario 4 the solar wind must not necessarily interact with only nanometer-scaled dust, if the dust itself has a complex and fractal structure. Then it would also be possible for solar wind ions to penetrate through heavier dust grains, which may be substantially less affected by CMEs.



A more recently proposed Scenario 5 argues that inner-source PUIs could also be created from energetic neutrals (Schwadron and McComas, 2010). These neutrals are created by charge-exchange in the heliosheath from interstellar PUIs and PUIs created within an outer population of interplanetary dust in the Kuiper Belt. Once the PUIs are neutralized they may travel back towards the Sun and could get ionized in the inner heliosphere again. This process is illustrated in Fig. 4. However, Bochsler and Möbius (2010) showed that the expected VDF of the PUIs created by this scenario would resemble more the VDF of the interstellar PUI component. Furthermore, almost no Si⁺ ions would be expected from this scenario, because high ionization rates would prevent neutral silicon to reach the inner heliosphere without being ionized. An overview over all inner-source PUI characteristics and their relation to the different proposed production scenarios will be given in the end of Chapter 3. Finally, it is well possible that multiple scenarios contribute significantly to the production of inner-source PUIs.

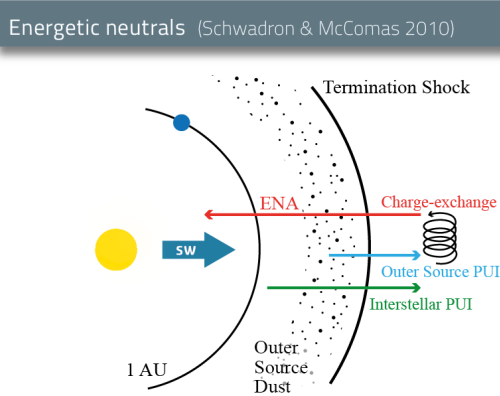


Figure 4: Illustration of the inner-source PUI production scenario proposed by Schwadron and McComas (2010). Interstellar PUIs and PUIs created by dust interactions in the Kuiper Belt charge-exchange in the heliosheath and re-enter inner heliosphere as Energetic Neutral Atoms (ENAs). The energetic neutrals can come close to the Sun and then be re-ionized creating inner-source PUIs.

1.6.2 Interstellar Pickup Ions

As the [LISM](#) is a partially ionized plasma, a population of neutral atoms can be found in it (see Tab. 1). Due to the relative motion of the heliosphere against the [LISM](#) a continuous stream of neutrals enters the heliosphere with a defined speed and direction, that can be combined in the interstellar neutral flow vector, \vec{v}_{ISN} . The neutral component of the [LISM](#) is unimpeded by electromagnetic forces exerted by the plasma interactions at the boundaries of the heliosphere. Therefore, these boundaries are not of any relevance for the interstellar neutral flow (also called interstellar wind). Consequently, the interstellar neutrals can penetrate into the heliosphere, where the only forces they are exerted to are the Sun's gravity and radiation pressure. The latter is most relevant for interstellar hydrogen, which leads to a substantial depletion of hydrogen in the inner heliosphere (see e.g. [McComas et al. \(2004\)](#)). Furthermore, hydrogen suffers far more ionization losses on its way into the inner heliosphere than helium due to charge-exchange and photoionization (e.g. [Kallenbach et al. \(2000\)](#)). Therefore, He^+ is the most abundant [PUI](#) species at 1 AU, even if hydrogen outnumbers helium by a factor of ~ 10 in the [LISM](#) (see Tab. 1 and [Frisch et al. \(2011\)](#)).

This population of neutral particles that fills the heliosphere is of course also subjected to ionization processes, which leads to the creation of interstellar [PUIs](#). Interstellar [PUIs](#) were already predicted by [Fahr \(1968\)](#) and their first observation was reported by [Möbius et al. \(1985\)](#). When considering a fixed distance from the Sun in the ecliptic plane (e.g. 1 AU), there are two regions in ecliptic longitude, where an enhanced [PUI](#) flux is observed: On the one hand the focusing cone ([Möbius et al., 1995](#)) directly at the downwind side of the Sun, on the other hand the so-called crescent ([Drews et al., 2012](#)), which is located in the upwind direction of the Sun. Both regions and example trajectories of interstellar neutrals are illustrated in Fig. 5. The focusing cone is a consequence of the gravitational focusing of the neutral particle trajectories after passing the Sun. Due to this focusing, an enhanced density of neutral particles is created. The [PUI](#) production rate is, of course, directly coupled to the abundance of neutral particles, which is why this enhancement in the neutral particle density can be translated into an enhanced [PUI](#) flux. The focusing cone is a comparatively local structure as it extends only over an angular range of about $\pm 15^\circ$. The crescent on the upwind side of the Sun is also coupled to the density of neutral particles. Again, considering a circular orbit around the Sun, the path of an interstellar neutral to reach a given distance is shortest at the ecliptic longitude, which corresponds to the upwind direction. Thus, these particles have been subjected to ionization processes for the shortest time, which means that more neutrals arrive at the given distance without being ionized. Leaving the upwind direction, the path, and therefore also the time the neutrals need to get there, gets longer. This leads to an increased fraction of neutrals that get ionized before reaching the given distance. Due to this effect, a steady increase in neutral particle density can be observed when approaching the upwind direction in longitude, which again translates into an increased [PUI](#) flux. Both regions are supposed to be aligned with the interstellar flow vector. Therefore, the interstellar [PUI](#) flux has been utilized to determine the interstellar flow longitude λ_{flow} , which has been performed in [Drews et al. \(2012\)](#). However, it has been shown, that this technique

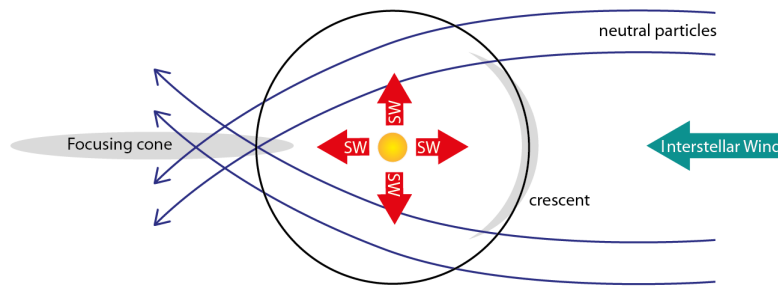


Figure 5: Illustration of the interstellar neutral flow through the heliosphere. The heliosphere moves towards the right-hand side with respect to the LISM. Thus, neutral particles enter the heliosphere, which are deflected by the Sun's gravitational potential. Two regions with enhanced PUI flux are observed: the focusing cone on the upwind side and the crescent on the downwind side of the Sun.

is subject to a systematic error, which is due to the preferred longitudinal transport of PUIs along the Parker spiral (Chalov and Fahr, 1999; Quinn et al., 2016). In Chapter 5 another method to determine λ_{flow} from interstellar PUI measurements utilizing the characteristic VDF is investigated that was introduced in Möbius et al. (2015). This method is supposed to be substantially less affected by these transport mechanisms.

1.6.3 Pickup Ion Velocity Distribution Functions

It is commonly assumed that PUIs are created from neutrals with a speed v_n significantly lower than the solar wind speed, v_{sw} . For inner-source PUIs this is not necessarily true, because of the unknown production mechanism, but for interstellar PUIs this assumption is definitely justified. Interstellar neutrals enter the heliosphere with a speed of about $v_{n,\infty} \approx 25.4 \text{ km s}^{-1}$, which means that they can reach a maximum speed of $v_n \approx 50 \text{ km s}^{-1}$ at 1 AU due to the gravitational attraction of the Sun. This is, of course, much lower than the average solar wind speed of $v_{\text{sw}} \approx 400 \text{ km s}^{-1}$. Consequently, the considerations in this section will focus on interstellar PUIs.

For simplicity, we consider a resting neutral that becomes ionized by one of the possible ionization processes and an IMF embedded into the solar wind, which is perpendicular to the radial direction. The relative velocity between the freshly created ion and the IMF corresponds in this case to \vec{v}_{sw} with $\vec{B} \perp \vec{v}_{\text{sw}}$ assuming a strictly radial solar wind flow. Thus, the ion is forced onto a gyro-orbit about the IMF line with a gyration speed equal to v_{sw} . As the IMF itself moves with v_{sw} , the speed of the PUI alternates between $2v_{\text{sw}}$ and 0 in a resting spacecraft frame

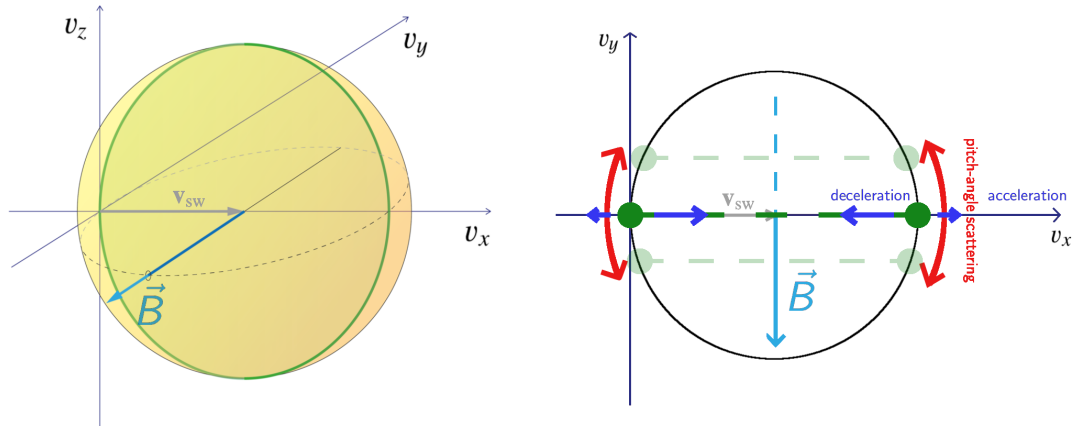


Figure 6: *Left:* 3D representation of the velocity space trajectory (green line) of a PUI created from a neutral at rest under an IMF configuration perpendicular to the solar wind velocity within the ecliptic plane. For every other IMF orientation, the trajectory lies on the yellow spherical shell. *Right:* 2D cut of the velocity space corresponding to the ecliptic plane with the configuration on the left hand side. The intersection of the velocity space trajectory with the considered plane is displayed by the green dots. Furthermore, the main processes modifying the initial PUI VDF are illustrated.

of reference. Of course, if the IMF is not perpendicular to the radial direction, the maximum speed of the PUI is decreased as only the component of the relative velocity that is perpendicular to the IMF is crucial for the gyration speed. However, we can also consider the gyration of a freshly injected PUI in velocity space. For a formerly resting neutral and a perpendicular IMF, the velocity space trajectory after injection is a circle perpendicular to \vec{B} with a radius of v_{sw} as shown in Fig. 6. Assuming an arbitrary IMF orientation, the advantage of the consideration in velocity space is that every possible velocity space trajectory lies on a spherical shell centered on \vec{v}_{sw} with radius v_{sw} . This means that the speed of freshly injected PUIs is always equal to v_{sw} in the solar wind frame of reference, independent of the IMF orientation. In the case of a non-resting neutral, the shell in velocity space grows or shrinks according to the relative motion of interstellar neutral and solar wind (see Chapter 5).

If we are not considering a single PUI, but an ensemble of PUIs that is continuously injected into the solar wind, the VDF that evolves corresponds to a torus in velocity space, which is commonly called the PUI torus VDF (Oka et al., 2002). In the dynamic solar wind this VDF is subjected to multiple processes that modify this initial VDF. Due to pitch-angle scattering by resonant wave-particle interactions the highly anisotropic torus VDF can be gradually transformed into an isotropic VDF. Initially, pitch-angle scattering has been assumed to be an efficient process, which leads to an instantaneous isotropization of the VDF (Vasyliunas and Siscoe, 1976). However, firstly Gloeckler et al. (1995) reported on H^+ VDF observations that do not fit an isotropic PUI VDF. Then, after the observation of significant anisotropies in the He^+ PUI VDF related to the IMF orientation (Möbius et al., 1998), it was argued that pitch-angle scattering is only effective for scattering the pitch-angle up to 90° , which means that only one hemisphere in velocity space would become isotropic rapidly (Isenberg, 1997). Recent observations, however, have shown that

the reason for the persisting anisotropy is that the PUI torus VDF is stable on longer timescales than previously assumed (Drews et al., 2015; Oka et al., 2002; Gershman et al., 2014).

Other processes that act on the PUI VDF involve deceleration and acceleration. While they are swept outward together with the solar wind, the initial PUI VDF diffuses in velocity in the solar wind frame of reference. The main driver of deceleration for an isotropic VDF, which implies a high pitch-angle scattering rate, has been assumed to be similar to the adiabatic cooling of an expanding ideal gas. Anyhow, as it has been proven that is very unlikely for the PUI VDF to be isotropic, this idea needs to be revised. On the other hand, PUIs experience a focusing effect due to the decreasing magnitude of the IMF with increasing heliocentric distance due to the conservation of the magnetic moment. This, in principle, means that the perpendicular component of the PUI velocity, v_{\perp} , decreases with distance. Furthermore, also the parallel component, v_{\parallel} decreases due to the conservation of the second complex Ginzburg-Landau invariant (Fahr, 2008). In total, this leads to a cooling of the VDF that is only due to the decrease of the IMF magnitude and which is therefore called magnetic cooling. There have been several investigations studying which is the dominant PUI cooling process (Saul et al., 2009; Chen et al., 2013), but all of these assumed an isotropic PUI VDF, which is not justified in the light of recent observations (see above for references).

Acceleration of PUIs in the solar wind can also occur due to several processes. First, interplanetary shock waves are known to efficiently accelerate PUIs via a first-order Fermi mechanism. These shock waves can occur as part of a CME (e.g. Lee et al. (2012)) or an SIR (Fisk and Lee, 1980). In the latter case, a shock rarely evolves within 1 AU, but is more likely to be present at larger distances from the Sun. Nevertheless, accelerated PUIs that can be related to an SIR are frequently observed at 1 AU. This is due to the turbulence that is created because of the compression of the fast solar wind. Within this turbulent region, PUIs can be accelerated via a second-order Fermi process, which is also called statistical acceleration (Schwadron et al., 1996). Apart from these local acceleration mechanisms that can be traced to special events on the Sun or structures in the solar wind, there seems to be an ubiquitous mechanism that continuously accelerates not only PUIs even within the quiet solar wind. The VDF of the accelerated particles commonly exhibits a power-law curve with a spectral index of -5 (see Fisk and Gloeckler (2007) and references therein). Multiple acceleration mechanisms have been proposed to this date (e.g. Fisk and Gloeckler (2012)), but still this acceleration poses a challenge for current research.

2

INSTRUMENTATION

In this chapter, a description of the measurement techniques and instruments used for the studies presented in Chapters 3, 4, and 5 is given. The focus lies on the sensors with the ability to measure PUIs utilized in this thesis, which is the Charge-Time-of-Flight (CTOF) sensor onboard the SOlar and Heliospheric Observatory (SOHO) spacecraft for Chapters 3 and 4, and the Plasma and Suprathermal Ion Composition (PLASTIC) instrument onboard the Solar-TERrestrial RElations Observatory (STEREO) spacecraft for Chapter 5. Both of these sensors are Time-of-Flight (ToF) mass spectrometers that are based on the same measurement concept. In detail, the sensors differ significantly in measurement capabilities, resolution, and performance. As the design of CTOF is more straight-forward compared to PLASTIC, the general concept of a ToF mass spectrometer is explained using this example. Based on that, PLASTIC and its additional capabilities are described.

As mentioned in the preceding chapter, PUIs are strongly coupled to the ambient solar wind plasma. Therefore, any conclusive measurement of PUIs requires knowledge of the ambient solar wind speed. Furthermore, the direction of the IMF vector has a significant impact on the PUI injection and accordingly on the resulting VDF. Consequently, additional instruments measuring the different properties of the interplanetary conditions are required to investigate PUIs. In the case of CTOF, solar wind speed measurements performed by the Proton Monitor (PM), which is integrated into the Mass-Time-Of-Flight (MTOF) sensor, are utilized. Furthermore, for the study performed in Chapter 4, IMF measurements are required that are taken from the Magnetic Field Instrument (MFI) onboard the Wind spacecraft, because no magnetometer is mounted on SOHO. In contrast to that, STEREO is equipped with a magnetometer that is part of the In-situ Measurements of Particles and CME Transients (IMPACT) instrument and solar wind properties can directly be derived from PLASTIC measurements. The solar wind parameter and IMF data are taken from pre-processed data provided by NASA's Coordinated Data Aanalysis Web¹. Thus, these measurements are not described in detail, but a brief presentation of the instruments is given.

¹ <https://cdaweb.sci.gsfc.nasa.gov/>

2.1 THE CTOF SENSOR ONBOARD SOHO

2.1.1 SOHO

The [SOHO](#) spacecraft was launched on 2nd December 1995 into a halo orbit around the first Lagrangian point, L1. It is located on the Sun-Earth line in a distance of about 0.99 AU from the Sun co-rotating together with Earth. Due to the reduced gravitational potential of the Sun due to Earth's gravity, a body at this point has the same orbital period around the Sun as Earth. It is well outside of Earth's magnetosphere, which means that solar wind unaffected by Earth's magnetic field can be sampled. [SOHO](#) is a three-axis stabilized spacecraft continuously pointing towards the Sun. The nominal mission lifetime was set to three years. Up to now, this lifetime has been extended seven times with the last extension agreeing on operation until the end of 2020.

[SOHO](#), and more precisely its 12 mounted instruments, were designed for three main scientific objectives, which are summarized in [Fleck \(1995\)](#). Firstly, it aims to investigate the structure and dynamics of the solar interior by means of helioseismology. The second main objective is the outstanding problem of the formation and heating of the solar corona. This objective is pursued by multiple solar atmosphere remote sensors. Lastly, [SOHO](#) was built to enhance our understanding of the origin and acceleration of the solar wind. For this purpose, the Charge, Element, and Isotope Analysis System ([CELIAS](#)) detector package and two other instrument suites that mainly consist of in-situ particle detectors are included in the [SOHO](#) payload.

2.1.2 CELIAS

As indicated in the previous section, the [CELIAS](#) detector package was designed to extend our understanding of the origin and acceleration of the solar wind. This scientific objective has been broken down to four scientific goals that are supposed to be reached with the different sensors. An overview about the purpose and the design of the [CELIAS](#) package may be found in [Hovestadt et al. \(1995\)](#).

Firstly, [CELIAS](#) aims to determine the isotopic composition of the solar wind. [MTOF](#) is the corresponding sensor for this objective, because it provides the highest mass resolution of all [CELIAS](#) sensors. This is achieved by a special isochronous arrangement of electrodes which decouples the ion's [ToF](#) from its energy. On the other hand, any information about the charge state is lost. Furthermore, the [PM](#) measuring a reduced velocity vector of the bulk solar wind, its density, and its temperature is included in this instrument.

The next scientific goal is the measurement of the composition and energy distribution of suprathermal particles. From these measurements, one can draw conclusions about the acceleration processes occurring in the solar corona. The Suprathermal Time-Of-Flight ([STOF](#)) and Highly Suprathermal Time-Of-Flight ([HSTOF](#)) sensors were designed to measure these particles. These sensors share the same [ToF](#) chamber, but show differences in their entrance systems. In general, their principle of operation is similar to the one of [CTOF](#) with the difference that they cover higher energies and a larger energy range.

Finally, **CTOF** was designed to determine the elemental and ionic composition of the solar wind as well as the composition of interstellar **PUIs**. From the elemental and in particular from the ionic composition, the temperature profile of the solar corona can be derived (see e.g. Aellig et al. (1998); Hefti et al. (2000)). The composition of interstellar **PUIs** is unrelated to the main scientific objective of **CELIAS**. However, in-situ measurements of the velocity and temperature of the local interstellar medium could improve our understanding of the heliospheric boundaries.

2.1.3 CTOF

CTOF is a linear **ToF** mass spectrometer. In Fig. 7 a photograph of the sensor is shown. It combines an electrostatic deflection system, a **ToF** chamber, and a Solid State Detector (**SSD**). Thus, three quantities of an incident ion are determined: the energy-per-charge E/Q , **ToF** τ , and the residual energy E_{SSD} . From these quantities, the mass M , charge Q , and energy E of the ion can be deduced. From the measurement of an ensemble of ions, their projected 1D **VDF** can be reconstructed.

Unfortunately, on Day of Year (**DoY**) 230, 1996, one of the transistors controlling the high voltage power supply broke, which resulted in a stopping of the E/Q stepping. After another failure of a similar transistor connected to the post-acceleration voltage, it was decided to set the post-acceleration voltage to a constant low level of 4 keV, which is too low for the measurement of heavy ions and **PUIs**. As the nominal operation of the sensor started on **DoY** 82 in the same year, only 148 days of data are available, which can be utilized for **PUI** studies.

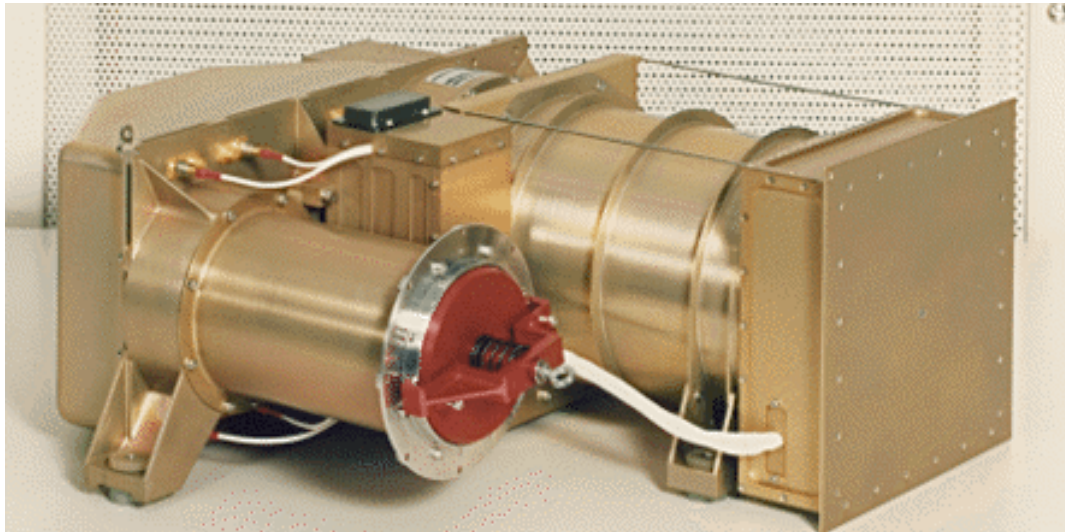


Figure 7: Photograph of the **CTOF** sensor. The ions enter the sensor through the aperture, which is closed with the red cap. Afterwards, a 180° hemispherical electrostatic analyzer has to be passed and subsequently the ions are subjected to a post-acceleration voltage. The **ToF** measurement is obtained within the **ToF** chamber, which is behind the aperture in the picture. At the end of the **ToF** chamber an **SSD** measures the residual energy.

The picture is taken from <http://www.ieap.uni-kiel.de/et/soho/celias/gallery.html>.

2.1.3.1 Principle of Operation

An example trajectory of an ion inside **CTOF** together with a schematic depiction of the measurement sections is given in Fig. 8. Firstly, ions enter the aperture through an ion optical system which results in an opening angle of $\pm 25^\circ$ in-ecliptic and $\pm 15^\circ$ out-of-ecliptic. Then they pass through the electrostatic analyzer, which is a hemispherical capacitor with an applied voltage, U_c , which allows only ions within a defined range of E/Q to pass. The voltage U_c is stepped through in 116 logarithmic steps in a cycle of 5 min. The conversion function from step number, i , to E/Q is

$$(E/Q)_i = U_0 \cdot r^{s_{\max} - i}. \quad (6)$$

The quantities U_0 and s_{\max} correspond to the minimum E/Q value and the maximum number of steps, respectively. All parameter values for this and the following formulae, Eqn. 7 and 8, are summarized in Tab. 2. There, also the bandwidth of each E/Q step is given.

Table 2: **CTOF** parameter values taken from [Hovestadt et al. \(1995\)](#) and [Hefti \(1997\)](#). The post-acceleration voltage and the thickness of the carbon foil had to be adapted in the in-flight calibration. The values displayed here are the original values from the instrument paper and the housekeeping data before the in-flight calibration.

Parameter	Value
Minimum E/Q value U_0	0.331095 kV
Maximum step number s_{\max}	116
Scaling factor r	1.040926
E/Q bandwidth	5.5%
Post-acceleration voltage U_{pa} ¹	$\begin{cases} 18.83 \text{ kV for DoY } 82 - 146 \\ 22.69 \text{ kV for DoY } 146 - 230 \end{cases}$
Area density of Carbon foil ρ ²	2.5 $\mu\text{g cm}^2$
Thickness of Carbon foil d ²	200 Å
ToF pathlength	70.5 mm

It is worth noting, that the E/Q is stepped through from high to low values. Low E/Q steps may correspond to the energy of the bulk solar wind protons that are far more abundant than heavy solar wind ions and pickup ions, for which the sensor was designed. If a defined flux is detected in the sensor, the electrostatic analyzer aborts stepping, which prevents the sensor from damage due to high particle flux. With the help of this concept, **CTOF**'s large geometry factor and high collection power is established.

After passing the electrostatic analyzer, the ion is accelerated by a so-called post-acceleration voltage, U_{pa} . This is necessary, because a carbon foil constitutes the entrance of the **ToF** chamber and without a post-acceleration voltage, the ions would

¹ Taken from the sensor's housekeeping data.

² Taken from [Hovestadt et al. \(1995\)](#).

not have sufficient energy to penetrate through the foil. Within this process, electrons are emitted from the foil that are guided to a Micro Channel Plate ([MCP](#)) triggering the START signal for the [ToF](#) measurement. After a pathlength l the ions hit an [SSD](#), where also secondary electrons are released that trigger the STOP signal. With a measured [ToF](#) τ , and energy-per-charge E/Q , the mass-per-charge M/Q of the incident ion can be calculated:

$$M/Q = 2 \frac{\tau^2}{l^2} (E/Q + U_{pa}) \cdot \eta(i, E_{post}) \quad (7)$$

The parameter $\eta(i, E_{post})$ is connected to the energy loss, $\Delta E(i, E_{post})$, of the ion during the passage of the carbon foil. It obviously depends on the considered element, i , and the ion's energy after post acceleration, $E_{post} = (E/Q + U_{pa}) \cdot Q$. More precisely, $\eta(i, E_{post})$ yields the fraction of energy that is transmitted through the foil, thus $\eta(i, E_{post}) = \frac{E_{post} - \Delta E(i, E_{post})}{E_{post}}$.

The residual energy of the ion is measured in the [SSD](#). Combining this measurement with the preceding ones, one can determine the ion's mass:

$$M = \frac{\tau^2}{l^2} \frac{E_{SSD}}{\beta(i, E_{tot})}. \quad (8)$$

The parameter $\beta(i, E_{tot})$ corresponds to the pulse height defect of the [SSD](#), which means that not the entire energy of the ion is converted into an electric signal. This is partly due to the dead layer of the detector, which causes energy loss that is not converted into a signal, and partly due to the creation of phonons that also do not contribute to the creation of a signal. The pulse height defect again depends on the considered element and now the energy after the passage of the carbon foil.

Using the M/Q and M information, an ion can be identified. Then the ion's energy and speed can be obtained from the E/Q information.

2.1.3.2 In-Flight Calibration

The in-flight calibration of the [CTOF](#) sensor has been performed in two complementary Master theses: [Janitzek \(2014\)](#) and [Taut \(2014\)](#). In [Janitzek \(2014\)](#) the mass determination (Eqn. 8) has been optimized; in [Taut \(2014\)](#) the M/Q conversion has been developed. As we only need the M/Q information here, we only provide a brief summary of the methods utilized in [Taut \(2014\)](#) and review the results.

From Eqn. 7 one can see that at a given E/Q step ions with the same M/Q should trigger a similar [ToF](#) signal. This means, that the [ToF](#) information can be converted into a M/Q value. For the identification of heavy [PUIs](#), which is needed in Chapter 3, and of He^+ at the energies considered in Chapter 4, the M/Q identification is sufficient. On the one hand, heavy [PUIs](#) like C^+ and O^+ have a uniquely high M/Q that does not occur among solar wind ions. On the other hand, the [VDF](#) of pickup He^+ extends to higher energies than the thermalized solar wind ions, which makes it easy to identify He^+ at the speeds considered in Chapter 4.

The main idea of the in-flight calibration is to adapt Eqn. 7 to the data collected in-flight. The variable parameters are U_p and η , or more precisely the thickness of the carbon foil, d . For this purpose, prominent ion species are selected that can be identified by their abundance and approximated [ToF](#) position: He^+ , He^{2+} , O^{6+} ,

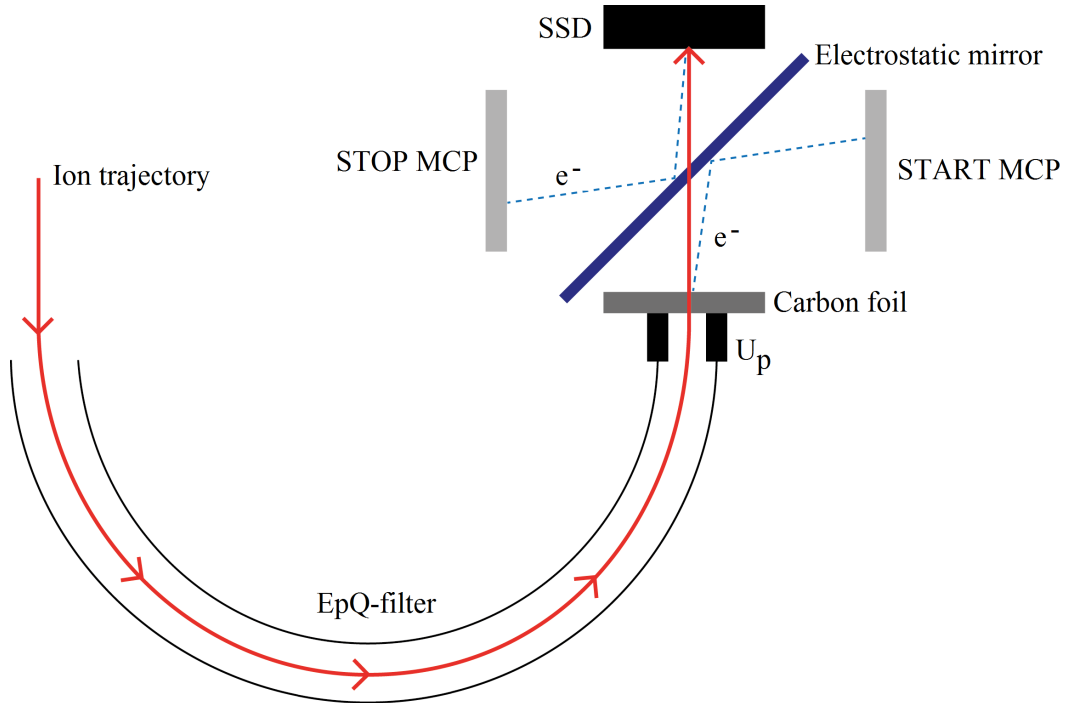


Figure 8: Illustration of CTOF's principle of ion detection. After the entrance of the ion through the ion-optical system (not displayed) the hemispherical E/Q filter is passed, which is followed by a post-acceleration voltage. Afterwards, the ions have to pass through a Carbon foil to enter the ToF chamber. During the passage, secondary electrons are emitted from the foil that are guided to an MCP by an electrostatic mirror. This MCP triggers the START signal of the ToF measurement. At the end of the ToF chamber the ions hit an SSD, where the residual energy is measured and again secondary electrons are emitted. These electrons are also guided to another MCP, which triggers the STOP signal.

Fe^{10+} , Fe^{11+} , C^+ , and O^+ . As the energy loss in the carbon foil at the beginning of the ToF chamber is a process with statistical nature, the ions form a distinct distribution around their most probable ToF values. A fit of these distributions has been performed to determine the most probable ToF value, τ_{ch} , at each E/Q given in channel numbers. These values have been compared to the physical values (in ns) expected from Eqn. 7. The most probable energy loss in the carbon foil has been determined with the help of simulations utilizing the Tracking and Range of Ions in Matter (TRIM) software (Ziegler and Biersack, 2008). As there has to be a unique and linear transformation from channel numbers into ns, the physical values, τ_{ns} , over the fitted values, τ_{ch} , must result in a straight line. The parameters U_p and d have been optimized to minimize the deviation between the data points and a least-squares fit of these with a straight line. The resulting parameters are:

$$U_p = \begin{cases} 20.04 \text{ kV for DoY } 82 - 146 \\ 24.07 \text{ kV for DoY } 146 - 230 \end{cases} \quad (9)$$

$$d = 240 \text{ \AA} \quad (10)$$

Eqn. 7 with the optimized U_{pa} together with η determined from TRIM simulations using a carbon foil thickness of $d = 240 \text{ \AA}$ constitutes the in-flight calibration of the ToF information. Now, each ToF value at a given E/Q can be translated to an M/Q value and, vice versa, for every ion species its expected ToF in channel numbers at a given E/Q can be calculated. This has been performed in Fig. 9, where a 2D histogram of ToF vs. E/Q step number normalized to each E/Q step is shown.

Note that the parameter η differs depending on the ion species. Consequently, the conversion from ToF into M/Q only works precisely for the considered ion species. In Chapter 3 the energy loss of C^+ is utilized for the conversion into M/Q and the ion identification, while in Chapter 4 only He^+ is considered and, of course, the energy loss of He^+ is utilized for the conversion into M/Q. The M/Q values of the other ion species calculated with the conversion function using this energy loss, are shifted with respect to the difference in energy loss in the foil. A more detailed discussion of this issue can be found in Taut et al. (2015) and Taut (2014).

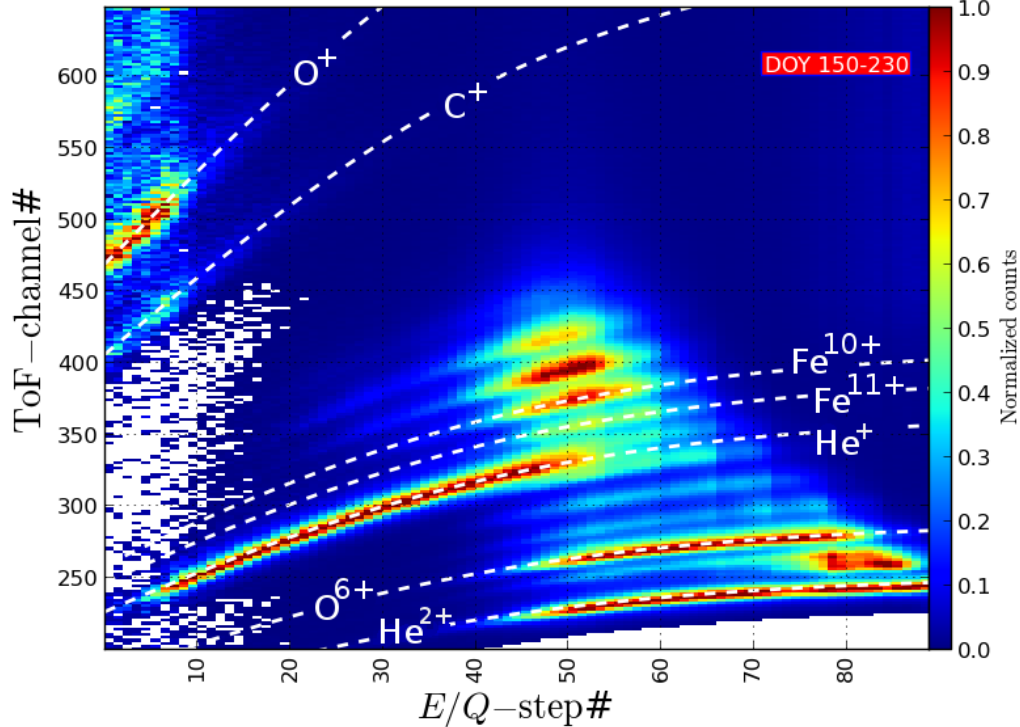


Figure 9: 2D histogram of the ToF in channel numbers vs. E/Q step number for 80 days of CTOF data from DoY 150 to 230, where the post-acceleration voltage was constant. The counts are normalized to the maximum of counts within each E/Q step. The dashed white lines correspond to the calibration results for various ion species. The plot is taken from Taut (2014).

2.1.4 Wind/MFI

As [SOHO](#) does not carry a magnetometer, but [IMF](#) data is required to investigate the [PUI VDF](#) as it is performed in Chapter 4, we need to use an extrapolation of [IMF](#) data measured onboard the Wind spacecraft.

The Wind spacecraft is part of NASA's Global Geospace Science program and was launched on 1st November, 1994. Wind went through different mission stages and as a result its orbit has been changed from time to time. But at the time of the [CTOF](#) measurements, Wind and [SOHO](#) were both orbiting L1.

The magnetometer experiment that Wind carries is the [MFI](#) and consists of two triaxial fluxgate magnetometers ([Lepping et al., 1995](#)). A fluxgate magnetometer basically measures the magnetic field strength through the saturation of a magnetically susceptible coil core. As one of these cores can only measure the field strength in one direction, a triaxial fluxgate magnetometer consists of three of these measuring the magnetic field strength in every dimension of space. To estimate the effect of the spacecraft-generated magnetic field, one magnetometer is deployed at the end of the 12-m spacecraft boom, while the other magnetometer is mounted approximately in the middle of the boom.

In this configuration, the [IMF](#) vector is sampled with a frequency of about 10.9 Hz. From this data, one can determine the mean [IMF](#) on larger timescales, which is then used to extrapolate the [IMF](#) vector to the location of [SOHO](#). This issue is discussed in more detail in [Taut et al. \(2016\)](#), which is presented in Chapter 4.

2.2 THE PLASTIC SENSOR ONBOARD STEREO

2.2.1 STEREO

The [STEREO](#) mission consists of two identical spacecraft, [STEREO Ahead \(STA\)](#) and [STEREO Behind \(STB\)](#), that were launched in late October 2006 ([Kaiser et al., 2008](#)). Both spacecraft were brought into a heliocentric orbit: [STA](#) with a slightly smaller distance to the Sun compared to Earth, [STB](#) with a slightly larger distance (see Fig. 10). Due to this configuration, [STA](#) is orbiting the Sun ahead of Earth, while [STB](#) is trailing Earth. The angular distance as seen from the Sun between the two spacecraft and Earth is thus increasing yearly by $\sim 22^\circ$. The advantage of such a multi-spacecraft mission is the possibility to have a synchronized observation of heliospheric phenomena like [CMEs](#) at different locations. Especially the transport of energetic particles through the heliosphere can be investigated with this setup, e.g. how energetic particles which are produced in a solar flare fill the heliosphere (e.g. [Dresing et al. \(2014\)](#)).

Each spacecraft carries identically constructed scientific instruments including optical, radio, and in-situ particle sensors. The main scientific objectives of the [STEREO](#) mission are to understand and characterize the formation and propagation of [CMEs](#), to discover solar energetic particle acceleration mechanisms, and to find a global model of the [IMF](#) and solar wind. Furthermore, the [STEREO](#) spacecraft are used for space weather forecasts.

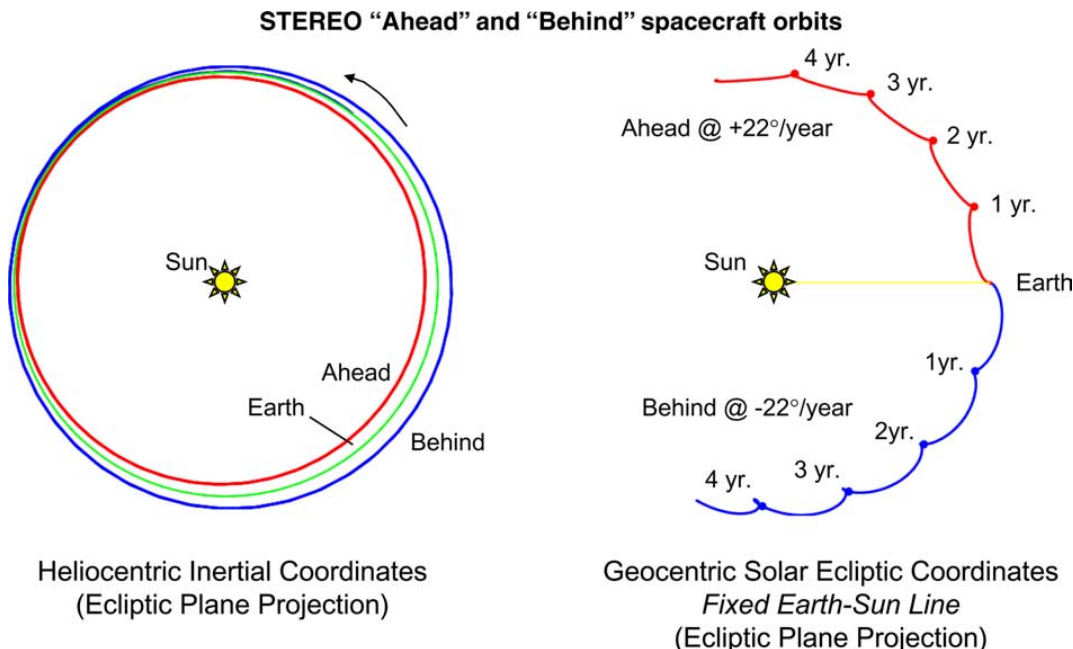


Figure 10: Illustration of the orbits of [STA](#) and [STB](#) taken from [Kaiser \(2005\)](#). For [STA](#), the mean distance to the Sun is smaller than the mean distance of Earth, which results in a shorter orbital period. Consequently, [STA](#) is ahead of Earth and, vice versa, [STB](#) is trailing Earth. Each year the angular distance between each spacecraft and Earth increases by 22° .

2.2.2 PLASTIC

Similar to CTOF on SOHO, PLASTIC is a linear ToF mass spectrometer combining an electrostatic analyzer, a ToF chamber, and an SSD measurement. Thus, the principle of ion detection and identification is the same as the one explained in Sec. 2.1.3.1 in the context of CTOF. However, in the following the difference between these two sensors is discussed. More detailed information about the design of PLASTIC and its scientific objectives may be found in Galvin et al. (2008). In Fig. 11 a photograph of the instrument is displayed.

Firstly, PLASTIC covers a higher energy range than CTOF: $0.3 \text{ keV/q} - 80 \text{ keV/q}$. Furthermore, one of the main unique features of PLASTIC is that it provides almost complete angular coverage in azimuthal direction. For this purpose, PLASTIC's aperture is divided into three sectors: The Solar Wind Section (SWS), the Wide Angle Partition with SSDs (WAPSSD), and the Wide Angle Partition without SSDs (WAPNOSSD). In Fig. 12 a an illustration of these sectors is provided.

2.2.2.1 The Solar Wind Section

As its name indicates, the SWS points towards the Sun at any time to sample solar wind ions. Its total FoV covers $\pm 22.5^\circ$ in azimuthal direction (inside the ecliptic plane) and $\pm 20^\circ$ in latitudinal direction. This section itself is divided into two channels, the Main- and the Small-Channel. The difference between these two channels is that the Main-Channel provides a ~ 5000 times larger geometric factor than the Small-Channel. The idea behind this is that PLASTIC can measure both rare heavy solar wind and PUIs, and far more abundant bulk solar wind protons and He^{2+} . In detail, this works as follows: The electrostatic analyzer is stepped through from high to low E/Q. As at high E/Q no bulk solar wind protons or He^{2+} ions are expected to be measured, the Main-Channel is used at the beginning of each measurement cycle. When approaching lower E/Q values, the relevant parts of the VDF of the heavy solar wind ions and PUIs are covered, as the ion speed is related to the E/Q step by the ion's M/Q (see Eq. 7). When approaching the bulk of the He^{2+} and H^+ VDFs, the ion flux in the instrument increases significantly. When a certain count rate is reached, PLASTIC switches to the Small-Channel.

Additionally, the SWS can distinguish between 32×32 incident angles of a detected ion. The measurement of the angle in latitudinal and azimuthal direction is

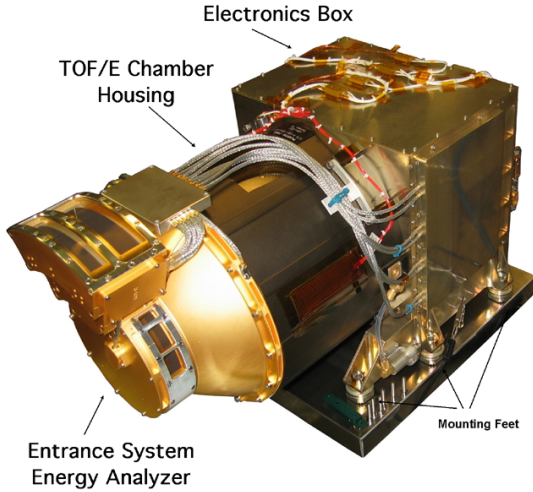


Figure 11: Photograph of the PLASTIC sensor. Due to its aperture spanning almost 360° , it looks substantially different than CTOF. On top of the electrostatic analyzer, the entrance slits of the Main- and the Small-Channel of the Solar Wind Section can be seen. The picture is taken from Galvin et al. (2008).

performed by two independent systems. Each system provides 32 linearly spaced bins of angular incidence. In latitudinal direction, an additional deflection voltage is stepped through every 435 ms. In azimuthal direction, the angle of incidence is reconstructed by evaluating a resistive anode.

In Chapter 5 of this thesis, pulse height analysis data is utilized for the analysis of He^+ PUIs. Additionally, PLASTIC provides solar wind parameters like the solar wind speed, v_{sw} , the solar wind proton density, n_p , or the proton thermal speed, v_{th} . In contrast to the PUI data, these data products are taken from pre-processed data that utilized a Maxwellian fit of the proton distributions provided by the University of New Hampshire.

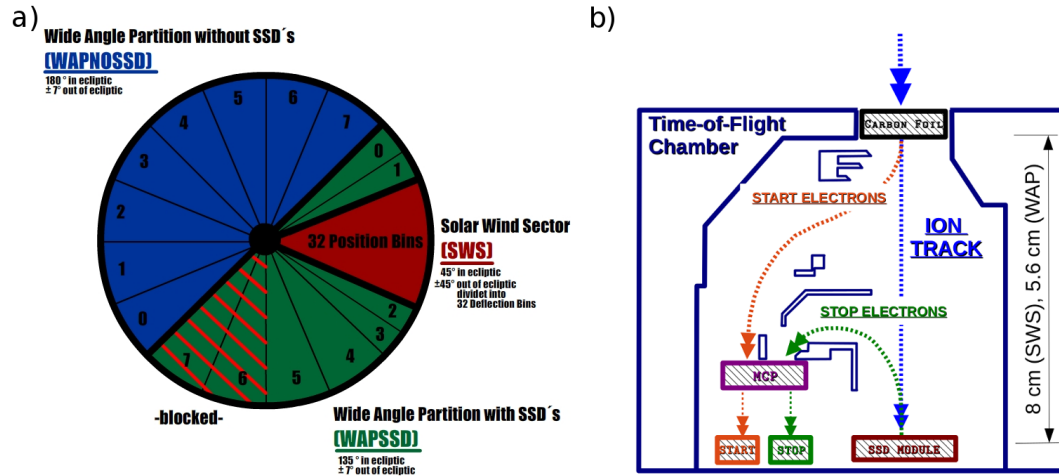


Figure 12: a) Illustration of the three parts of PLASTIC's aperture. The Solar Wind Sector is pointing towards the Sun at any time. The Wide Angle Partition is divided into a partition with SSD's (WAPSSD) and a partition without SSD's (WAPNOSSD). Both partitions are itself divided into eight position bins, wherein two are blocked within the WAPSSD. b) Schematic illustration of the ToF chamber within the PLASTIC sensor. Similar to CTOF secondary electrons are emitted at the beginning and the end of the ToF path, which trigger the START and STOP signals of the measurement. In contrast to CTOF, the electrons are guided by a complex deflection system onto the same MCP.

Both figures are taken from Drews (2013).

2.2.2.2 The Wide Angle Partition

The Wide Angle Partition (WAP) consists of 16 separate position bins that cover a total angle in the ecliptic of 315° . The polar acceptance range of all position bins is $\pm 7^\circ$ and no polar angle of incidence is measured. This configuration results in a large geometry factor, which is suited for the measurement of rare suprathermal particles.

The WAP is divided into the WAPSSD and the WAPNOSSD. Each partition consists of eight position bins. Within the WAPSSD an energy signal for a measured ion can be acquired. This partition spans an angular range of 135° . In the WAPNOSSD, which covers an angular range of 180° , the measured ions directly hit an MCP for triggering a STOP signal for the ToF measurement. In contrast to the WAPSSD section, where also the mass M of a measured ion can be determined due to the

residual energy measurement, only the M/Q information can be determined for ions that are measured in the [WAPNOSSD](#) section (see Eqn. 7 and 8).

2.2.2.3 In-Flight Calibration

The in-flight calibration of the PLASTIC sensor has been performed in [Drews \(2009\)](#) and it has been successfully utilized for He^+ in [Drews et al. \(2010, 2012, 2015\)](#) and for heavy PUIs in [Drews et al. \(2016\)](#). An extensive summary of the calibration is provided in [Drews \(2013\)](#). In general, the procedure of the in-flight calibration of PLASTIC is analog to the one utilized for the calibration of [CTOF](#). The expected [ToF](#) of prominent ions calculated from a simplified model of the sensor have been compared to the measured [ToF](#) peak positions at each E/Q step and finally the model has been adapted to match the in-flight measurements. In Fig. 13 the M/Q calibration is displayed in a 2D histogram of all measured counts in a 30 day timerange beginning on 1st June 2007 as a function of [ToF](#) channel and E/Q step. As in Fig. 9, the expected [ToF](#) has been calculated for various ion species at each E/Q step (see Eqn. 7). In particular, at low E/Q steps, which corresponds to high ion speeds, He^+ can be separated well from the other ion species. But also He^{2+} and O^{6+} show pronounced signatures, while the iron ions as well as other heavy solar wind ions cannot be identified by eye. One can also surmise a signature of O^+ ions, while almost no clear abundance of C^+ is observed. Anyhow, it is worth noting that due to the complicated [ToF](#) path of the electrons in the sensor head (see Fig. 12 b), the resolution in [ToF](#) is reduced compared to [CTOF](#) (cf. Fig. 9 and 13). Due to that, despite [CTOF](#)'s comparatively short operation time, it is suited

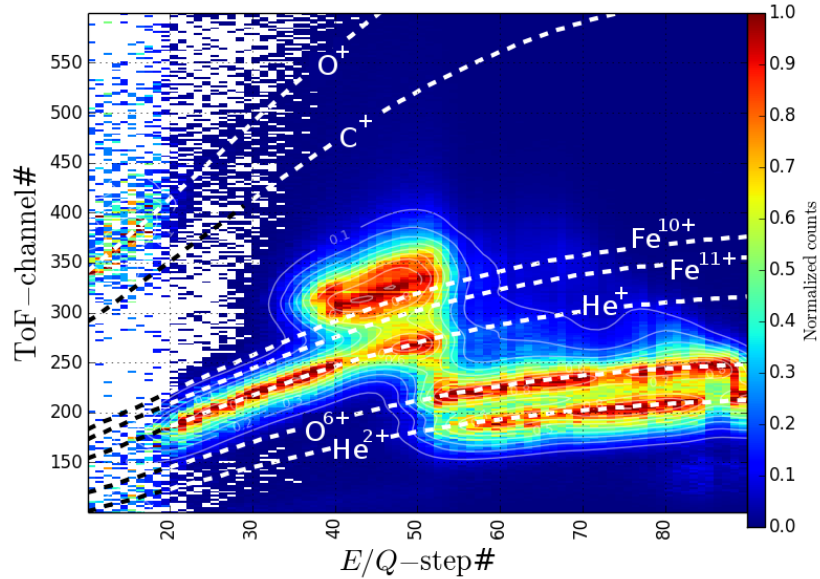


Figure 13: 2D histogram of the [ToF](#) in channel numbers vs. E/Q step number for 30 days of [PLASTIC](#) data starting from 1st June 2007. The counts are normalized to the maximum of counts within each E/Q step. The dashed white lines correspond to the calibration results for various ion species. This is analog to Fig. 9, but for [PLASTIC](#) data.

better for the investigation of heavy PUIs. This in turn does not mean that it is impossible to study heavy PUIs with PLASTIC (Drews et al., 2016). Accordingly, He^+ and He^{2+} can be identified well by a simple box rate approach. This means that at a given E/Q step, the ion species is assigned by a specified range in ToF, which is directly connected to the M/Q.

2.2.3 IMF Data from IMPACT

The IMPACT instrument package consists of six particle sensors covering various energy ranges and one magnetometer. Its main scientific focus lies on the investigation of CMEs.

Anyhow, for the investigation of PUIs, and in particular, their VDF we utilize the IMF data provided by IMPACT's magnetometer (Acuña et al., 2008). This is a single triaxial fluxgate magnetometer mounted 3 m away from the spacecraft body on the deployable boom. It provides measurement of the IMF vector with a frequency of 8 Hz in standard mode and for selected time periods where enhanced resolution is required up to 32 Hz in burst mode. As PLASTIC offers a time resolution of 5 min, the standard mode data is sufficient to derive the mean IMF.

COMPOSITION OF INNER-SOURCE PICKUP IONS

This chapter aims to contribute to the answer to Question 1: *What is the nature of the inner source for PUIs?* The observation of a randomly distributed flux of C⁺ PUIs with a similar abundance than O⁺ and an VDF peaked at $w \approx 1$ cannot be explained by interstellar neutrals. Consequently, there must be a source for PUIs somewhere in the inner heliosphere. As indicated in Sec. 1.6.1, multiple ideas have been proposed that could explain the existence of inner-source PUIs, but the detailed nature of the production mechanism is still unknown. One of the criteria that a possible inner-source PUI production scenario must fulfill is, that it must predict a composition similar to the solar wind. The composition of inner-source PUIs has been determined by Gloeckler et al. (2000a) utilizing data from Solar Wind Ion Composition Spectrometer (SWICS) on the Ulysses spacecraft and Allegrini et al. (2005) utilizing SWICS data from the Advanced Composition Explorer (ACE). However, both studies have in common that they rely on a very limited number of counts: 800 and 250, respectively. The only two production scenarios that would result in such a composition are the solar wind recycling and the solar wind neutralization scenario, which are therefore the most promising candidates for the main driver of the inner-source PUI production.

In this chapter, we go beyond the statement of a composition similar to the solar wind. We aim to find a precise measure for the composition by utilizing CTOF data. As CTOF ceased operation after only ~ 150 days, its data set has been widely neglected up to this point, even though it had a high collection power due to a large geometry factor. Together with the in-flight calibration developed in Taut (2014), which enables the identification of heavy PUIs, we have been able to determine the composition of inner-source PUIs with a data set providing about one order of magnitude more statistics than the data utilized in the former studies. Then, we test how this composition is compatible with the expectations of an inner-source PUI composition from the solar wind neutralization scenario.

3.1 BRIEF SUMMARY OF THE PUBLICATION

After the introduction of the context and the aims of this paper, the utilized data set for the determination of the inner-source PUI composition is described. This is followed by a detailed description of the method that has been developed to find the composition. The ion identification is obtained from a fit of M/Q count histograms in several energy ranges. For the fit of the peaks of the individual ion species, a method to predict the peak shape based on TRIM simulations of the ions passing through the sensor's carbon foil has been developed. The determined composition is presented and compared to former results. Additionally, a systematic dependence of the O⁺/C⁺ ratio on solar wind speed is discovered, that is consistent with the former studies and explains the deviations from those to each other.

Then, we introduce a toy model, which obtains the expected inner-source PUI composition from the solar wind neutralization scenario. For this, a few simplifying assumptions had to be made, which are discussed. The results from this model are compared to the determined composition and deviations are reviewed with respect to systematic errors in the data analysis.

Overall, we find that there is a comparatively good correspondance between the determined composition and the model results. Furthermore, the systematic trend of the O⁺/C⁺ ratio with solar wind speed depicts a new characteristic of the inner-source PUI production that must be predicted by any possible production scenario. We have been able to reproduce this trend qualitatively with our model and provide arguments that the solar wind recycling scenario would predict a trend reversed to the observation. This, in summary, means that the solar wind neutralization scenario is likely to be the main driver of the inner-source PUI production.

3.2 PUBLICATION

The following article is reproduced from Taut et al. (2015) with permission from Astronomy & Astrophysics, ©ESO.

Composition of inner-source heavy pickup ions at 1 AU: SOHO/CELIAS/CTOF observations - Implications for the production mechanisms

A. Taut, L. Berger, C. Drews and R. F. Wimmer-Schweingruber, *Astronomy & Astrophysics*, 576:A55 (2015), DOI: 10.1051/0004-6361/201425139

Own contribution: 80%

Composition of inner-source heavy pickup ions at 1 AU: SOHO/CELIAS/CTOF observations

Implications for the production mechanisms

A. Taut, L. Berger, C. Drews, and R. F. Wimmer-Schweingruber

Institut für Experimentelle und Angewandte Physik, Christian-Albrechts-Universität zu Kiel, 24098 Kiel, Germany
e-mail: taut@physik.uni-kiel.de

Received 10 October 2014 / Accepted 22 January 2015

ABSTRACT

Context. Pickup ions in the inner heliosphere mainly originate in two sources, one interstellar and one in the inner solar system. In contrast to the interstellar source that is comparatively well understood, the nature of the inner source has not been clearly identified. Former results obtained with the Solar Wind Ion Composition Spectrometer on-board the Ulysses spacecraft revealed that the composition of inner-source pickup ions is similar, but not equal, to the elemental solar-wind composition. These observations suffered from very low counting statistics of roughly one C^+ count per day.

Aims. Because the composition of inner-source pickup ions could lead to identifying their origin, we used data from the Charge-Time-Of-Flight sensor on-board the Solar and Heliospheric Observatory. It offers a large geometry factor that results in about 100 C^+ counts per day combined with an excellent mass-per-charge resolution. These features enable a precise determination of the inner-source heavy pickup ion composition at 1 AU. To address the production mechanisms of inner-source pickup ions, we set up a toy model based on the production scenario involving the passage of solar-wind ions through thin dust grains to explain the observed deviations of the inner-source PUI and the elemental solar-wind composition.

Methods. An in-flight calibration of the sensor allows identification of heavy pickup ions from pulse height analysis data by their mass-per-charge. A statistical analysis was performed to derive the inner-source heavy pickup ion relative abundances of N^+ , O^+ , Ne^+ , Mg^+ , Mg^{2+} , and Si^+ compared to C^+ .

Results. Our results for the inner-source pickup ion composition are in good agreement with previous studies and confirm the deviations from the solar-wind composition. The large geometry factor of the Charge-Time-of-Flight sensor even allowed the abundance ratios of the two most prominent pickup ions, C^+ and O^+ , to be investigated at varying solar-wind speeds. We found that the O^+/C^+ ratio increases systematically with higher solar-wind speeds. This observation is an unprecedented feature characterising the production of inner-source pickup ions. Comparing our observations to the toy model results, we find that both the deviation from the solar-wind composition and the solar-wind-speed dependent O^+/C^+ ratio can be explained.

Key words. solar wind – Sun: heliosphere – Sun: abundances

1. Context and aims

Pickup ions (PUIs) are former neutrals in the heliosphere that get ionised either by solar extreme ultra-violet radiation, charge exchange with solar-wind protons, or electron impact. The neutral atoms might originate in the interstellar medium or in a source in the inner heliosphere that is presently not completely understood.

Interstellar PUIs were first observed *in situ* by Möbius et al. (1985). These ions are created from neutrals in the interstellar wind that can penetrate deeply into the heliosphere. Owing to gravitational focusing of their trajectories, a region of enhanced interstellar PUI density evolves on the downwind side of the Sun, which is called the focusing cone (Möbius et al. 1985; Drews et al. 2010). On the upwind side of the Sun, a comparable region called the crescent evolves that is a consequence of a geometric effect combined with ionisation probabilities (Drews et al. 2012). Owing to the very low speeds of the interstellar neutrals compared to the solar-wind speed, the pickup process manifests itself in a highly suprathermal, characteristic velocity distribution function (VDF).

In contrast to the PUIs created from interstellar neutrals, inner-source PUIs show a VDF that has the shape of a thermal distribution with the maximum located approximately at the solar-wind bulk speed (Geiss et al. 1995). The established interpretation for this is that these ions are produced very close to the Sun between 10–50 R_\odot (Schwadron et al. 2000), thermalise with the solar wind, and cool adiabatically like an ideal gas due to the spatial expansion. These inner-source PUIs were studied predominantly with the Solar Wind Ion Composition Spectrometer (SWICS) on-board Ulysses, which revealed further characteristics: The source seems to be distributed randomly in space and time (Geiss et al. 1996), is stable over the solar cycle (Allegrini et al. 2005), and has a production rate of $\sim 10^6$ g s⁻¹ (Geiss et al. 1996). Furthermore, the inner-source PUI composition resembles the solar-wind composition (Gloeckler et al. 2000) and the inner-source PUI flux of one element is correlated with the solar-wind ion flux of this element, which is shown in the companion paper by Berger et al. (2015). Especially the last findings point towards an ion production somehow related to the solar wind.

Overall, four possible production scenarios have been proposed (Bzowski & Królikowska 2004; Schwadron et al. 2000; Wimmer-Schweingruber & Bochsler 2003; Mann & Czechowski 2005) that have been checked for their compatibility with the observed characteristics (Allegri et al. 2005). None of the proposed scenarios could conclusively explain all observations, but the two scenarios involving the interaction of dust grains with the solar wind (Schwadron et al. 2000; Wimmer-Schweingruber & Bochsler 2003) remain the most promising. Schwadron et al. (2000) and Geiss et al. (1995) posit that μm -sized interplanetary dust grains are immersed in the solar wind and that solar-wind ions are implanted in the surface of these grains. The former ions can then be re-emitted as atoms or molecules, for example by sputtering of the surface or thermal release. The weaknesses of this scenario are that it fails to reproduce the rather high inner-source PUI flux (Allegri et al. 2005) and that one would expect much more sputtered grain material in the composition (Wimmer-Schweingruber & Bochsler 2003). Wimmer-Schweingruber & Bochsler (2003) propose a different neutral particle production mechanism involving solar-wind ions passing through nm-sized dust grains. During the passage they lose a part to all of their charge and exit the dust grain as neutrals or low-charged ions. However, this scenario predicts differences in the inner-source PUI flux in solar minimum and maximum, because nm-sized dust grains are supposed to get trapped in coronal mass ejections (Allegri et al. 2005). Since there are still uncertainties in both the observed characteristics and the implications of the proposed scenarios, inner-source PUIs merit more detailed investigation.

PUIs with masses heavier than helium, which we call heavy PUIs, are very rare compared to ordinary heavy ion abundances in the solar wind. Previous heavy PUI studies, performed with the SWICS instrument on-board Ulysses, had to deal with very low counting statistics of roughly one C^+ count per day (cf. Geiss et al. 1996), which could be compensated for to some extent by its long operation time. The Charge-Time-Of-Flight sensor (CTOF) of the Charge-EElement-and-Isotope Analysis System (CELIAS) on-board the SOlar and Heliospheric Observatory (SOHO) spacecraft at L1 combines a high mass-per-charge resolution with a large geometry factor. From this data we derived the inner-source heavy PUI composition and compared it to the composition one would expect from the production scenario proposed by Wimmer-Schweingruber & Bochsler (2003). Thanks to CTOF's high counting statistics it was also possible to investigate the measured O^+/C^+ ratio with respect to varying solar-wind speeds.

2. Methods

CTOF combines the measurement of energy-per-charge, time-of-flight, and residual energy to derive an ion's mass, charge, and energy. The detailed principle of ion detection is described in Hovestadt et al. (1995). For our study the raw pulse-height analysis (PHA) words have been used as they contain the whole measurement information.

The energy-per-charge, E/Q , and time-of-flight, τ , measurements are sufficient to determine the mass-per-charge, M/Q , and velocity, v_{ion} , of an ion. The M/Q information alone is sufficient to identify heavy PUIs and to distinguish them from solar-wind ions. The M/Q range of these single- or low-charged ions ($M/Q \geq 12 \text{ amu e}^{-1}$) is far above the M/Q range of ordinary solar-wind ions (for example $M/Q(\text{Fe}^{7+}) = 8 \text{ amu e}^{-1}$). Furthermore, because of their small charge, heavy PUIs rarely have enough energy to trigger the solid-state detector that is

needed to determine their mass. In contrast, heavy solar-wind ions, such as iron with their higher charges, almost always lead to an energy measurement. To suppress background counts caused by heavy solar-wind ions, we constrained our analysis to data where no energy signal was measured.

To determine the M/Q from the raw pulse-height analysis data, we performed an in-flight calibration of the CTOF sensor (Taut 2014). The time-of-flight positions of the He^+ , He^{2+} , O^{6+} , Fe^{10+} , and Fe^{11+} peaks at given E/Q values were compared to theoretical values based on a physical model of the sensor. A conversion function from E/Q and τ to M/Q values was derived from this. This resulting function is based on the energy loss, ΔE , of C^+ in CTOF's carbon foil. This means that the peak of C^+ appears at $M/Q = 12 \text{ amu e}^{-1}$, while other peaks may appear shifted with regard to their nominal M/Q , for example O^+ at $M/Q = 16.2 \text{ amu e}^{-1}$. The PUI species-dependent energy loss even allows distinguishing between PUIs with the same M/Q . At the same E/Q value, Mg^{2+} loses significantly less energy per mass than C^+ while passing the carbon foil. Thus it is shifted towards a peak position of $M/Q \approx 10.7 \text{ amu e}^{-1}$.

2.1. Time period

We used PHA data from March 22 until August 17, 1996 when CTOF ceased nominal operation. A post-acceleration voltage increase on May 25 is considered in the in-flight calibration. On June 13, 1996 CTOF measured O^+ ions originating in Venus' atmosphere (Grünwaldt et al. 1997). We removed this time period from the present analysis because this work focuses on ordinary inner-source PUIs. We therefore analysed all available data from March 22 until August 17, 1996 with the only exclusion being June 13, 1996.

2.2. General approach

PUIs of interstellar and inner-source origins have quite different VDFs. We use $w = v_{\text{ion}}/v_{\text{sw}}$ as the ordering parameter, where v_{ion} is the speed of an individual ion and v_{sw} is the solar-wind bulk speed as determined by the SOHO/CELIAS Proton Monitor (PM). Observations revealed that the inner-source PUI contribution dominates the interstellar contribution at $w < 1.2$ (Berger et al. 2013). To determine the inner-source heavy PUI composition, we therefore derived the relative abundances of N^+ , O^+ , Ne^+ , Mg^+ , Mg^{2+} , and Si^+ compared to C^+ between $w = 0.8$ and $w = 1.2$.

The upper limit of $w = 1.2$ sets a boundary to the usable solar-wind speeds due to the E/Q coverage of the sensor. The maximum speed of Si^+ that can be measured is $v_{\text{max}}(\text{Si}^+) = 487 \text{ km s}^{-1}$, which results in a maximum solar-wind speed of $v_{\text{sw,max}} = 406 \text{ km s}^{-1}$ to guarantee that the instrument covers the whole w -range equally for all ions.

Owing to the stochastic nature of the energy loss in the carbon foil, the measured M/Q of heavy PUIs is smeared out. The time-of-flight (and therefore the M/Q) distribution of a single ion species (e.g., O^+) is clearly peaked but has a certain width. Thus ions whose time-of-flight peaks in the immediate neighbourhood (e.g., C^+) contaminate the original distribution. This makes it impossible to uniquely identify an individual time-of-flight measurement as due to a certain ion, and the species assignment needs to be done in a statistical manner.

Because we only want to compare the abundance ratios in the $0.8 \leq w < 1.2$ range and w cannot be derived from E/Q information without the species assignment, we ordered the counts

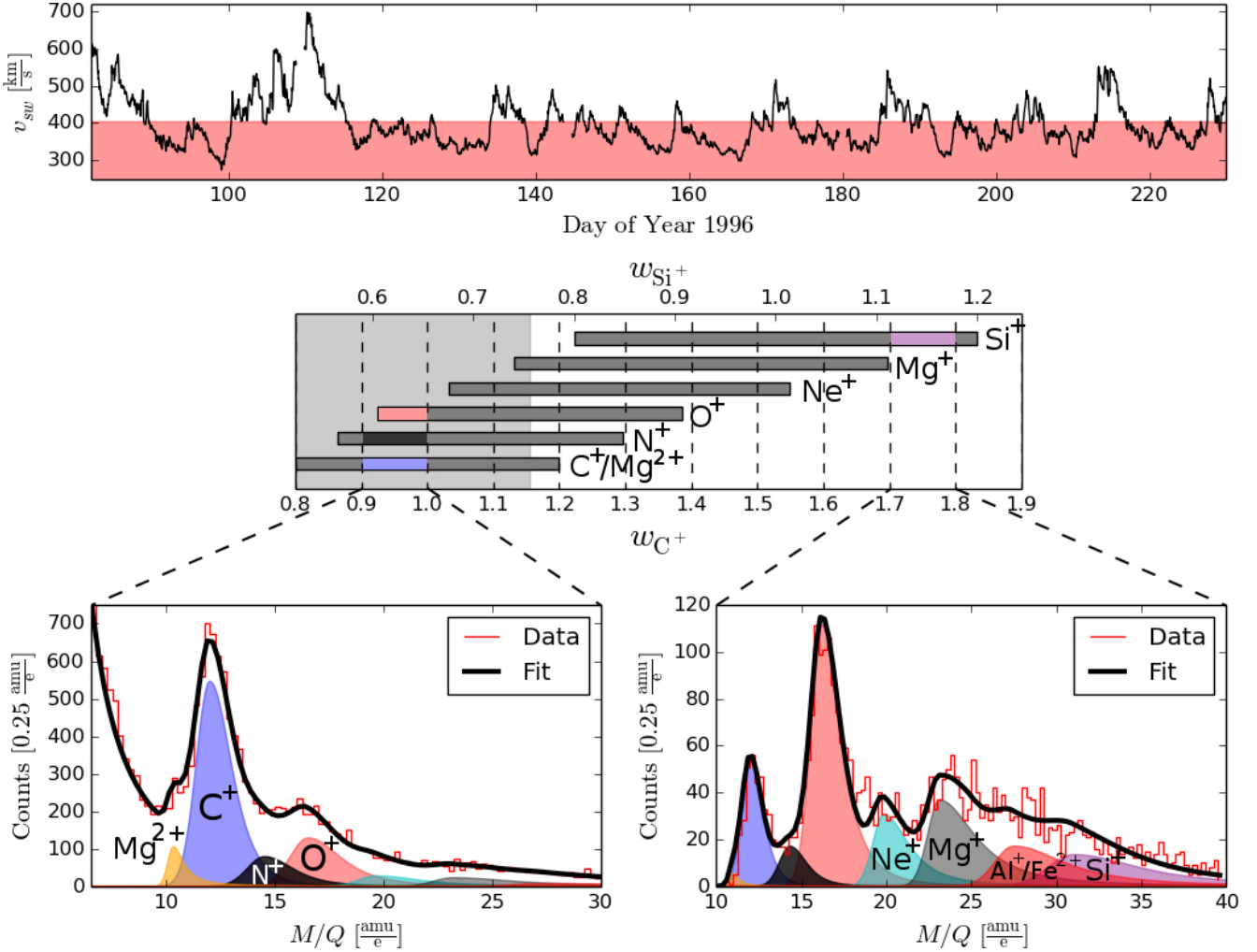


Fig. 1. Illustration of the analysis technique used to obtain the abundance ratios of the different pickup ion species. *Top panel:* time series of the solar-wind speed in the considered time period measured with the CELIAS/PM. The solar-wind speeds in the area shaded red correspond to about 65% of the considered time period. These data were used in our analysis. *Middle panel:* w_i -coverage for $0.8 \leq w_i < 1.2$ for each heavy PUI in terms of w_{C^+} . The dashed lines correspond to the w_{C^+} bins for which counts were determined. The shaded area on the left-hand side of the plot shows the range where $w_{He^+} \leq 2$, so we thus expect an enhanced background due to interstellar He^+ . Two example bins have been picked to show the fit of the corresponding M/Q histograms. *Lower left panel:* $0.9 \leq w_{C^+} < 1$ bin. One can see a significant amount of background counts that have been taken into account in the fit with a power-law distribution. This bin contributes to the total counts of C^+ , N^+ , Mg^{2+} , and partly to O^+ (highlighted in the middle panel). *Lower right panel:* corresponds to the $1.7 \leq w_{C^+} < 1.8$ bin. At energies this high, no background counts are observed and the distributions of Mg^+ , Al^+/Fe^{2+} , and Si^+ are more pronounced. Only the counts of Si^+ contribute to $0.8 \leq w_{Si^+} < 1.2$.

by the nominal w for C^+ denoted as w_{C^+} . This means that we calculated the w of a count as if it was C^+ regardless of its measured M/Q value. The nominal w_{C^+} can easily be converted into the w_i of other ions. For example, $w_{C^+} = 1$ corresponds to $w_{N^+} = 0.93$ and $w_{O^+} = 0.87$. In the upper left-hand panel of Fig. 1, the range $0.8 \leq w_i < 1.2$ is plotted in terms of w_{C^+} for every considered heavy PUI species. One can see that $0.8 \leq w_{C^+} < 1.9$ includes $0.8 \leq w_i < 1.2$ for all heavy PUIs up to Si^+ .

The counts have been ordered into bins with widths of $\Delta w_{C^+} = 0.1$. From all counts accumulated in this fashion, M/Q histograms are created and fitted using the fit function described in Sect. 2.5. The fit provides the optimised M/Q distribution for each considered heavy PUI that is integrated over M/Q to yield the count rate. This is shown for two example w_{C^+} bins in the lower panels of Fig. 1. The relative abundance is then accumulated from all w_{C^+} bins that cover $0.8 \leq w_i < 1.2$ for the corresponding ions taking detection efficiencies into account. This is indicated by the color code in the upper

left-hand panel of Fig. 1. For example, the $0.9 \leq w_{C^+} < 1$ bin contributes to the relative abundance of C^+ , N^+ , and partly to O^+ . The bins that only cover a part of the $0.8 \leq w_i < 1.2$ range are taken into account for the relative abundance with a weighting in correspondence to their bin coverage. The detection efficiencies are derived from measured efficiencies for He, C, N, and O (Hefti 1997) and extrapolated for the heavier ions.

2.3. Background model

Because of their low count rates, PUIs are affected by a time-of-flight background, which is due to the much more abundant interstellar He^+ and heavy solar-wind ions. Background counts in the M/Q range of heavy PUIs may have been produced by the following two effects. On the one hand, the tails of the time-of-flight distributions of interstellar He^+ and solar-wind iron ions reach into the time-of-flight range of heavy PUIs. The background caused by the solar-wind iron is partially suppressed

by using only events for which the residual energy is below threshold, i.e., registered as zero energy. The single tails can be described with a κ -distribution (lower part of Eq. (1)).

On the other hand, background counts may occur due to random time-of-flight coincidences. The large collection area of CTOF also means that many ions enter CTOF in a given E/Q step. Since there is a limited probability that an ion triggers a start or a stop signal for the τ measurement, it is possible that the start and stop signals of a single τ measurement are triggered by two different ions. This results in a random M/Q measurement. For the combination $w_i \approx 1$ and high M/Q values, the first effect is more important.

Background counts are negligible at $w_{C^+} \geq 1.3$. The boundary of $w_{C^+} = 1.3$ corresponds to $w_{He^+} = 2.25$ or $w_{Fe^{7+}} = 1.59$, for instance. He^+ has a very broad VDF that extends up to $w_{He^+} \approx 2$ due to its mainly interstellar origin, which is also shown in the upper left-hand panel of Fig. 1. Because CTOF measured on the upwind side of the Sun with respect to the interstellar wind, the w -distribution of interstellar He^+ is even smeared out to higher w values. The VDF of heavy solar-wind ions has its maximum approximately at the solar-wind bulk speed, and it has a comparatively small width. Thus at $w_{C^+} \geq 1.3$, no background counts are expected. Between $1.0 \leq w_{C^+} < 1.3$, only He^+ counts that reach into the M/Q range of the heavy PUIs have to be considered. Thus, it is sufficient to fit a κ -tail (see Eq. (1)) to the right-hand side of the He^+ peak to account for the background. At $w_{C^+} < 1.0$, a complex background is observed that consists of multiple ion species that cannot be resolved individually. In this case, a power-law distribution is a good approximation for the shape of the background counts.

2.4. Peak shape model

In the M/Q histograms, the heavy PUI peaks overlap each other owing to their large widths. As a result, only the C^+ and the O^+ peaks are clearly resolvable by eye (cf. lower panels of Fig. 1). To perform a precise statistical assignment of the counts, it is necessary to know the shapes of the single peaks.

The variable amount of energy lost by ions in the carbon foil results in a characteristic distribution, $f(M/Q)$, in the M/Q histograms. For a given ion species, the M/Q distribution can be described with a Gaussian- κ -function represented by the following equation:

$$f(M/Q) = A_0 \cdot \begin{cases} \exp\left(-\frac{(M/Q - M/Q_0)^2}{2\sigma_1^2}\right) & \text{if } \frac{M}{Q} \leq \frac{M}{Q}_0 \\ \left(1 + \frac{(M/Q - M/Q_0)^2}{\kappa_r \sigma_r^2}\right)^{-\kappa_r} & \text{if } \frac{M}{Q} > \frac{M}{Q}_0 \end{cases} \quad (1)$$

with the peak height A_0 , the peak position M/Q_0 , the peak widths σ_1 and σ_r on the left- and right-hand sides of the peak, respectively, and the parameter κ_r that describes the tail on the right-hand side of the distribution. All parameters depend on the ion species.

Because the variable energy loss is also the dominant process shaping the heavy PUI peaks, we simulate the passage of ions through the foil with the Tracking and Range of Ions in Matter (TRIM) software developed by Ziegler et al. (2010). A τ distribution of the ions can be deduced from these simulations that can be converted into an M/Q distribution using the conversion from the in-flight calibration. The actual ion peak shapes as measured by CTOF are estimated from this M/Q distribution.

The procedure for determining the ion peak shapes is illustrated in Fig. 2 for the example of O^+ for the energy range

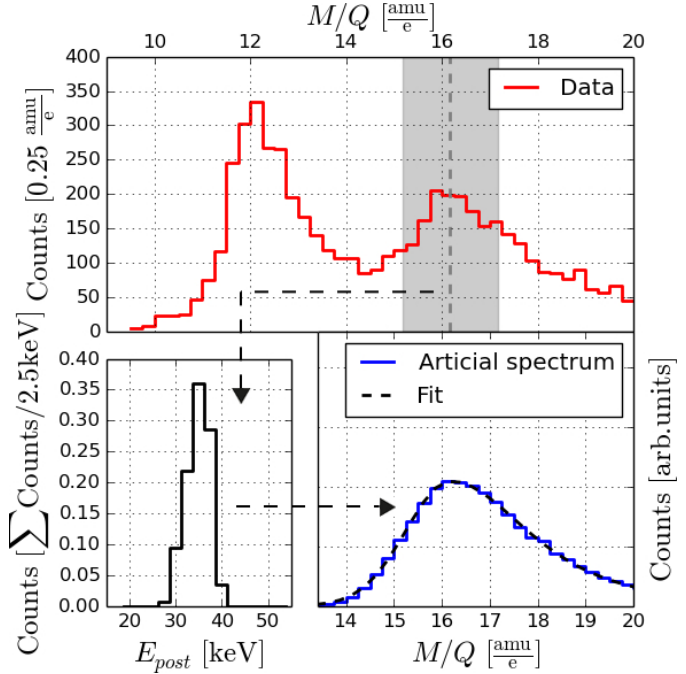


Fig. 2. Illustration of the estimation of the shape parameters for O^+ . The upper panel shows an M/Q histogram for $1.2 \leq w_{C^+} < 1.3$. From the peak's counts (a box with $M/Q_0 \pm 1 \text{ amu e}^{-1}$), a histogram of the energy of the ions when hitting the carbon foil is created (lower left panel). TRIM simulations corresponding to the energy bins are obtained. An artificial M/Q histogram is created from the transmitted energy and angular scattering information (lower right panel). A fit to this histogram yields estimated parameters for the real peak.

of $1.2 \leq w_{C^+} < 1.3$. In the upper panel the corresponding M/Q histogram is shown. The expected position $M/Q_0(O^+)$ of the O^+ peak can be calculated from the difference in the energy loss compared to C^+ and is shown by a dashed grey line. The shape of the M/Q distribution depends on the ion's energy after post-acceleration. This energy is smeared out because of multiple E/Q steps that contribute counts to the considered w range. We assume that in a box with $16.2 \pm 1 \text{ amu e}^{-1}$ predominantly O^+ occurs. From the measured E/Q and the post-acceleration voltage, the energy distribution with which the ions hit the foil is estimated, which is shown in the lower left-hand panel. For each occurring energy, TRIM simulations with sufficient statistics were performed to determine the M/Q distribution of O^+ . These distributions are weighted with the number of counts in the corresponding energy bin and summed up. The resulting artificial M/Q distribution is fitted with Eq. (1), which yields estimates for the shape parameters σ_1 , σ_r , and κ_r . This procedure is performed for the data from every w -bin described in Sect. 2.2.

It was found that the ratios of the peak width parameters, σ_1 and σ_r , between the different ion species stay constant to a large extent. Furthermore, the κ_r values were found to be fairly constant in the considered energy range. We did not take the absolute, but instead the relative values from the TRIM simulations, because we expect that the energy loss and angular scattering in the foil is the dominant reason for the asymmetry of the peak shapes, but other instrumental effects, such as electronic noise or non-ideal focusing of the trajectories, have been neglected. Thus only the σ_1 and σ_r ratios between two different peaks and the κ_r value were kept constant during the fit of the M/Q histograms. The corresponding values are given in Table 1.

Table 1. Peak shape parameter ratios with respect to the C⁺ peak derived with data from 270 km s⁻¹ ≤ v_{sw} ≤ 406 km s⁻¹ and Δw_{C⁺} = 0.1.

Ion	M/Q ₀ [amu e ⁻¹]	σ _l (Ion) σ _l (C ⁺)	σ _r (Ion) σ _r (C ⁺)	κ _r (Ion)
C ⁺	12	≡1	≡1	2.51 ± 0.20
N ⁺	14.34–14.53	1.24 ± 0.02	1.31 ± 0.02	2.13 ± 0.15
O ⁺	16.21–16.57	1.33 ± 0.06	1.47 ± 0.04	1.72 ± 0.09
Ne ⁺	19.66–19.92	1.27 ± 0.02	1.92 ± 0.12	1.39 ± 0.12
Mg ⁺	23.17–23.20	1.38 ± 0.12	2.68 ± 0.05	1.22 ± 0.07
Mg ²⁺	10.22–11.48	0.41 ± 0.01	0.44 ± 0.05	0.96 ± 0.02
Si ⁺	30.75–33.34	3.00 ± 0.20	4.99 ± 0.35	1.24 ± 0.33
Fe ^{2+,*}	~27.5	2.19	3.84	1.23
Al ^{+,*}				

Notes. (*) Since we are unable to distinguish between Al⁺ and Fe²⁺, the mean values of the Mg⁺ and Si⁺ parameters have been taken to model these ion populations.

2.5. Fit function

The fit function must include distributions for all ions that occur in the M/Q range of the considered heavy PUIs and the background model. Next to the seven heavy PUIs for which we want to compare the abundances, the isotopes of Ne and Mg and contributions of Al⁺ and Fe²⁺ are taken into account. Furthermore, the M/Q distribution of N⁺ probably contains counts of Si²⁺ that will be addressed in Sect. 3 in more detail. There are other ion species that lie inside the considered M/Q range, but the abundances of these ions are negligible compared to the considered ion species (Bochsler 2007).

The PUI isotopes $^{22}\text{Ne}^+$, $^{25}\text{Mg}^+$, and $^{26}\text{Mg}^+$ are included in the fit as distributions with the shape parameters σ_l , σ_r , and κ_r of $^{20}\text{Ne}^+$ or $^{24}\text{Mg}^+$, respectively, and the fixed abundances (Wiens et al. 2004):

$$\frac{^{22}\text{Ne}}{^{20}\text{Ne}} = 0.07; \frac{^{25}\text{Mg}}{^{24}\text{Mg}} = 0.14; \frac{^{26}\text{Mg}}{^{24}\text{Mg}} = 0.15.$$

The neutral particles that serve as the source population for inner-source PUIs are most probably created from solar-wind ions or interplanetary dust grains. Since both solar-wind ions and interplanetary dust grains have the same isotopic composition (Wimmer-Schweingruber et al. 1998), the isotopic composition of PUIs is also expected to be the same. In the M/Q histogram shown in the lower right-hand panel of Fig. 1, one can see a very flat decrease in the counts beyond the Mg⁺ peak, which is due to the Mg isotopes. In Sect. 3 the relative PUI abundances are compared to elemental solar-wind abundances. Therefore, the Ne⁺ and the Mg⁺ abundance ratios will include the abundances of all their isotopes.

Since the contributions of both Al⁺ and Fe²⁺ peak at $M/Q \approx 27.5$ amu e⁻¹, it is impossible to resolve these ion species separately. Nevertheless, we have to avoid counts of Al⁺ or Fe²⁺ being falsely attributed to Mg⁺ or Si⁺. Therefore one single distribution representing both ion species is taken into account in the fit function. Of course, no distinct relations for σ_l , σ_r , and κ_r following the procedure described in Sect. 2.4 and no detection efficiency can be deduced for this mixed species peak. Because of the latter, no abundance for these ion species could be determined. For the peak shape parameters σ_l , σ_r , and κ_r , the mean of the shape parameters of Mg⁺ and Si⁺ was chosen.

Overall, the fit function $F(M/Q)$ is the sum of 11 Gaussian- κ -functions (Eq. (1)) and the background model (Sect. 2.3):

$$F(M/Q) = \sum_i f_i(M/Q) + BG(M/Q) \quad (2)$$

with

$$i \text{ from } \left\{ \begin{array}{l} \text{C}^+, \text{N}^+, \text{O}^+, \underbrace{\text{Ne}^+, \text{Ne}^+, \text{Ne}^+}_{\text{Ne}^+}, \text{Mg}^{2+}, \\ \underbrace{\text{Mg}^+, \text{Mg}^+, \text{Mg}^+, \text{Mg}^+}_{\text{Mg}^+}, \text{Si}^+, \text{Al}^+/\text{Fe}^{2+} \end{array} \right\} \quad (3)$$

and

$$BG(M/Q) = \begin{cases} 0 & \text{for } w_{C^+} > 1.3 \\ A_{bg} \cdot \left(1 + \left(\frac{\frac{M}{Q} - \frac{M}{Q_{bg}}}{\kappa_{bg} \sigma_{bg}^2} \right)^2 \right)^{-\kappa_{bg}} & \text{for } 1. \leq w_{C^+} < 1.3 \\ A_{bg} \cdot \left(\frac{M}{Q} - \frac{M}{Q_{bg}} \right)^{b_{bg}} & \text{for } w_{C^+} < 1. \end{cases} \quad (4)$$

2.6. Fit results

Every ion distribution in the fit function has five parameters: A_0 , M/Q_0 , σ_l , σ_r , and κ_r . The fit function contains 11 different ion distributions in all and the background model that results in 55 to 59 parameters, depending on the background type.

The peak position M/Q_0 is determined by comparing the energy loss and angular scattering in CTOF's carbon foil of the considered ion and C⁺. The κ_r parameters are assumed to be constant. For σ_l and σ_r , relations for every ion species with respect to C⁺ were derived, which means that one parameter for σ_l and one for σ_r are sufficient to describe all peak widths. The ranges for M/Q_0 , the σ_l and σ_r relations, and the κ_r values are given in Table 1. Thus, the remaining free parameters for the fit of the M/Q histograms are eight peak heights A_0 , the peak widths of C⁺, $\sigma_l(\text{C}^+)$ and $\sigma_r(\text{C}^+)$, and the parameters of the background model. This gives a total of 10 to 14 free parameters.

The widths of the M/Q distributions primarily depend on the energy the ions have when hitting CTOF's carbon foil. It is known from TRIM simulations that at lower impact energies, the peak widths increase. A linear relation for $\sigma_l(\text{C}^+)$ and $\sigma_r(\text{C}^+)$ depending on the mean energy of the ions before hitting the foil was derived to consistently include this in the fit. Finally, only the eight peak heights A_0 and, if necessary, three or four parameters of the background model are fitted to the data. The optimisation is performed using the Nelder-Mead method and

Table 2. Results from the derivation of the inner-source PUI composition measured with SOHO/CELIAS/CTOF at 1 AU compared to the studies of Gloeckler et al. (2000) and Allegri et al. (2005).

Ion	M/Q [amu e ⁻¹]	This work	Gloeckler et al. (2000)	Allegri et al. (2005)
C ⁺	12	≡1	≡1	≡1
N ⁺	14	0.23 ± 0.02	0.27 ± 0.04	0.42 ± 0.09
O ⁺	16	0.56 ± 0.04	0.68 ± 0.07	0.99 ± 0.15
Ne ⁺	20	0.16 ± 0.01	0.22 ± 0.02	0.14 ± 0.03
Mg ⁺	24	0.28 ± 0.02 ^a	0.33 ± 0.05	–
Mg ²⁺	12	0.08 ± 0.02 ^b	–	–
Si ⁺	28	0.21 ± 0.02 ^a	0.22 ± 0.04	–
v_{sw} [km s ⁻¹]		270–406	318–864	~750
r [AU]		1	1.49	2
L [$^{\circ}$]		0	<60	70

Notes. The abundance ratios were normalised to the abundance of C⁺. In the bottom rows, the corresponding heliocentric distances, r , and heliographic latitudes, L , of the observations are shown. ^(a) Possibly affected by a large systematic error. ^(b) Sensitive to background subtraction.

a maximum-likelihood estimator based on Poisson statistics. Afterwards, the counts are corrected for instrumental detection efficiencies. The resulting inner-source PUI composition at 1 AU is displayed in Table 2. The abundances were normalised to the abundance of C⁺, because it offers the highest counting statistics and is expected to originate solely in the inner source.

2.6.1. Variable solar-wind speeds

Gloeckler et al. (2000) and Allegri et al. (2005) have found significantly different inner-source O⁺/C⁺ abundance ratios (see Table 2). The reason for this could be that the O⁺/C⁺ ratio shows a systematic increase with solar-wind speed. To address this issue, we focused our investigation on the O⁺/C⁺ abundance ratio.

To compare the abundances of all heavy PUIs up to Si⁺ in the previous section, we had to restrict our analysis to solar-wind speeds below 406 km s⁻¹ owing to the M/Q -dependent velocity coverage of CTOF. For O⁺ the maximum velocity that CTOF can measure is $v_{max}(O^{+}) = 645$ km s⁻¹. Thus, considering only C⁺ and O⁺, the solar-wind speed range in which the sensor covers $0.8 \leq w < 1.2$ equally for both ions extends up to 537 km s⁻¹. Furthermore, C⁺ and O⁺ are resolved well because they are the most abundant heavy PUIs. This means that these two ion species provide excellent comparability.

Using the CTOF data, we investigated the inner-source O⁺/C⁺ abundance ratio at different solar-wind speeds. For this, we sorted the PUI counts in v_{sw} bins from $270 \text{ km s}^{-1} \leq v_{sw} \leq 537 \text{ km s}^{-1}$. We repeated the analysis to the data accumulated in these solar-wind bins. The results are shown in Table 3. A clear dependency of the O⁺/C⁺ ratio on the solar-wind speed can be seen. The ratio increases systematically with solar-wind speed. This dependence of the heavy PUI composition on solar-wind speed is a newly observed feature of inner-source heavy PUIs, and it has to be checked for its compatibility with the proposed production scenarios. Furthermore, it explains the deviation of the ratios derived by Gloeckler et al. (2000) and Allegri et al. (2005). A scenario consistent with this newly found characteristic must predict differences in the production rates of O⁺ and C⁺ that depend on the solar-wind speed.

2.7. Error estimation

The errors given in Tables 2 and 3 are the pure counting errors that result from Poisson statistics. They were calculated

Table 3. Abundance ratios of O⁺/C⁺ for $0.8 \leq w < 1.2$ at varying solar-wind speeds.

Solar-wind speed [km s ⁻¹]	$\frac{O^{+}}{C^{+}}$
≤350	0.49 ± 0.06
350–400	0.58 ± 0.02
400–450	0.70 ± 0.04
450–500	0.82 ± 0.05
500–537	0.95 ± 0.19

by applying the procedure above 100 times using histograms with random Poisson noise added and random M/Q bin widths between 0.2 amu e⁻¹ and 0.5 amu e⁻¹.

Apart from these counting errors, there might be further systematic errors that affect the results. After all, only the C⁺ and O⁺ peaks are clearly visible in the M/Q histograms. By setting up a peak shape model based on TRIM simulations (see Sect. 2.4), the other peaks have been resolved, which means that the derived abundances depend on the accuracy of this model. This is especially relevant for ions that strongly overlap with other peaks such as N⁺, Ne⁺, Mg⁺, and Si⁺. Furthermore, the contributions of Al⁺ and Fe²⁺ can only be roughly estimated with the given approach.

The Mg²⁺ abundance is sensitive to the background subtraction. As a result, the background model may be a source of systematic errors that would mainly affect the abundances of C⁺ and Mg²⁺.

Only data where no residual energy signal was triggered was used for our analysis. But even low-charged PUIs have a low probability of triggering a residual energy measurement. This probability is negligible for singly charged PUIs at low speeds. But counts triggered by Mg²⁺ or PUIs at higher speeds may escape our analysis. This again means that the result for the abundance of Mg²⁺ is very uncertain. The O⁺/C⁺ ratio at higher solar-wind speeds is only affected to a small extent by this effect. Hovestadt et al. (1995) gives a threshold of ~25 keV for the residual energy measurement. Considering the energy loss of the post-accelerated ions in the carbon foil (10–20% for C⁺ and O⁺), and the energy loss in the dead layer of the solid state detector (~40% for C⁺ and O⁺) ions with an initial speed of ~560 km s⁻¹ can overcome this threshold. This affects the O⁺/C⁺ ratio at solar-wind speeds above 450 km s⁻¹ because speeds up to $w = 1.2$ have been considered. To quantify

Table 4. Comparison of the heavy PUI composition derived from CTOF data with the solar-wind composition (von Steiger et al. 2000; Shearer et al. 2014) and the modelled composition that one would expect from the production scenario proposed by Wimmer-Schweingruber & Bochsler (2003).

Ion	M/Q [amu e ⁻¹]	Solar wind	$\frac{\text{Ion}}{\text{C}^+}$	Simulation $r_{\min} = 30 R_\odot, D = -1$	$x/x^+/x^{++}$	Simulation $r_{\min} = 30 R_\odot, D = -1.3$	$x/x^+/x^{++}$	Simulation $r_{\min} = 4 R_\odot, D = -1.3$	$x/x^+/x^{++}$
C ⁺	12	≡1	≡1	≡1	55/43/2	≡1	51/47/2	≡1	20/58/23
N ⁺	14	0.13 ± 0.04	0.23 ± 0.02	0.07 ± 0.03	75/24/2	0.07 ± 0.03	72/26/2	0.09 ± 0.04	34/39/26
O ⁺	16	1.49 ± 0.19	0.56 ± 0.04	0.64 ± 0.08	80/18/2	0.65 ± 0.08	78/20/2	0.83 ± 0.11	37/32/31
Ne ⁺	20	0.25 ± 0.06	0.16 ± 0.01	0.09 ± 0.02	83/16/2	0.09 ± 0.02	82/17/1	0.16 ± 0.04	44/36/20
Mg ⁺	24	0.21 ± 0.09	0.28 ± 0.02 ^a	0.27 ± 0.11	36/55/10	0.26 ± 0.10	34/56/10	0.27 ± 0.11	14/74/12
Mg ²⁺	12		0.08 ± 0.02 ^b	0.05 ± 0.02		0.04 ± 0.02		0.04 ± 0.02	
Si ⁺	28	0.20 ± 0.07	0.21 ± 0.02 ^a	0.39 ± 0.08	3/86/11	0.37 ± 0.08	2/87/11	0.27 ± 0.06	1/81/19

Notes. For the model, three different parameter sets were chosen (see text). The column $x/x^+/x^{++}$ denotes the fractions of neutral, x , single-charged, x^+ , and doubly-charged, x^{++} , particles of a certain element at 1 AU in percent. ^(a) Possibly affected by a large systematic error. ^(b) Sensitive to background subtraction.

the impact of this effect, we compared the amount of C⁺ and O⁺ counts that have been registered with zero energy with the amount of all counts for these ion species in the highest solar-wind speed bin, $500 \text{ km s}^{-1} \leq v_{\text{sw}} < 537 \text{ km s}^{-1}$, using a simple box rate approach and a restriction to $1 \leq w < 1.2$ to avoid background counts. In this data set, 82% of the C⁺ counts and 88% of the O⁺ counts have been measured with zero residual energy, which in turn means that the restriction to events with zero residual energy introduces a small systematic error that is, however, smaller than the statistic error.

Finally, there are uncertainties in the efficiency model, which is only based on measurements for C, N, and O and extrapolated for heavier ions. Altogether, the uncertainties of Mg⁺ and Si⁺ given in Tables 2 and 4 are underestimated because their abundance might be affected by strong systematic errors, which are not included there.

3. Discussion

In the following, the results presented in Tables 2 and 3 are compared to the results derived by Allegrini et al. (2005) and Gloeckler et al. (2000). Afterwards a simple model is used to relate our observations to the solar-wind neutralisation scenario.

3.1. Comparison with former results

CELIAS/CTOF acquired inner-source PUI data at 1 AU during solar activity minimum in 1996 for rather low solar-wind speeds. The Gloeckler et al. (2000) data were obtained by Ulysses/SWICS at low and middle latitudes at an average heliocentric distance of 1.49 AU between 1994 and 1995, which also corresponds to the solar activity minimum. During this time Ulysses measured predominantly in high solar-wind speeds but also in low solar-wind speeds ranging from 318 km s^{-1} to 864 km s^{-1} . The data used by Allegrini et al. (2005) were also obtained by Ulysses/SWICS but in three different time periods, two in solar minimum and one in solar maximum, where SWICS measured exclusively in high solar-wind speeds at a heliocentric distance of ≈ 2 AU and latitudes of about 70° . For our analysis we used a total of $\sim 42\,000$ counts, while the other studies are based on ~ 800 counts (Gloeckler et al. 2000) and ~ 250 counts (Allegrini et al. 2005).

Our results for the inner-source heavy PUI composition are in satisfactory agreement with the values derived by Gloeckler et al. (2000) when keeping in mind that the O⁺/C⁺ ratio shows

a systematic trend with solar-wind speed. Although one can see significant deviations, especially for O⁺, former studies claimed that the inner-source PUI composition resembles the elemental solar-wind composition that is shown in Table 4 taken from von Steiger et al. (2000), except for the neon abundance that was taken from the more recent analysis of Shearer et al. (2014). Our results confirm these systematic deviations and raise the question of their origin, which is probably connected to the production mechanism of inner-source PUIs.

Our investigation focuses on the solar-wind neutralisation idea by Wimmer-Schweingruber & Bochsler (2003) that is the most promising production scenario. This scenario provides two effects that influence the inner-source PUI composition: on the one hand, the charge-state distribution of an ion after passing a thin dust grain depends on the ion energy and species. On the other hand, every ion species has a different ionisation probability. We suggest that the interplay of these two effects could already lead to the observed PUI composition.

3.2. Solar-wind neutralisation model

The basic idea is that the solar wind streaming outwards interacts with the dust population and continuously produces neutrals, singly-, and doubly-charged ions on the line of sight between the Sun and the spacecraft. If one assumes that the interaction cross-section for the dust population is equal for all solar-wind ions and every ion-dust interaction produces one single-charged PUI, we would observe solar-wind composition. But from experiments performed with thin carbon foils, we know that ions leaving the dust cannot be only neutral, but also (multiply) charged. The distribution of charge states after the interaction strongly depends on ion energy and species. Furthermore, this distribution can subsequently be altered by ionisation processes. Thus the measured composition of one-fold ionised PUIs does not necessarily resemble the solar-wind composition.

To investigate the deviation from the solar-wind composition, we set up a simple toy model for the solar-wind neutralisation scenario to study the impact of the effects mentioned above. Our model is similar to but even more simplified than the approach by Bochsler et al. (2007) who have already investigated the alteration of the PUI composition by these effects.

We assume that the solar wind streams radially outwards. Thus the flux, f_{sw} , decreases with r^{-2} with r the heliocentric distance, but the composition remains constant. At each distance solar-wind ions may interact with thin dust particles, resulting

in the production of neutrals and low-charged ions. The dust population is modelled with an interaction cross-section that depends on the heliocentric distance: $\sigma(r) \propto r^D$. Furthermore, we only assume very thin carbon foils for which the energy loss of the solar-wind ions is negligible. Thus, the interacting particles still have solar-wind velocity after the passage. This is also consistent with the observed w -spectra of inner-source PUIs. In this case these spectra would not exclusively stem from adiabatic cooling but would evolve directly from the production mechanism (Bochsler et al. 2006).

The fractions for neutrals, η , single-, η^+ , and doubly-ionised particles, η^{++} , after the foil passage are estimated from measurements of ions passing through thin carbon foils (Gonin et al. 1995, 1994; Bürgi et al. 1993; Wimmer-Schweingruber & Bochsler 2003; Allegrini et al. 2014). In addition to the primary production of the particles due to the dust grain passage, photo-ionisation is considered. Next to photo-ionisation, particles may also be ionised by electron impact or charge-exchange with solar-wind protons that are not included in our model because photo-ionisation is usually the dominant ionisation process. It cannot be ruled out that the other ionisation processes favour certain ion species. The photo-ionisation rates, v and v^+ , for the different ions at 1 AU were derived following the formula and parameters given in Verner et al. (1996) and scaled with r^{-2} .

For the solar radiation spectrum, a typical spectrum during solar minimum measured with TIMED/SEE was used (Woods et al. 2000). Thus neutrals are ionised to single-charged ions with the rate v , and single-charged ions can be ionised to doubly-charged ions with the rate v^+ . Since only a small fraction of the interacting particles end up as doubly-charged ions and the ionisation probability for doubly-charged ions is generally lower than for singly-charged ions, further ionisation is neglected. Moreover, the process starts at a certain distance from the Sun, r_{\min} , because dust grains sublime at a certain distance from the Sun, and the solar-wind must have been accelerated before interacting with the dust. This means that PUIs may be produced continuously on the path between r_{\min} and our point of observation, 1 AU. The simulation works on a linear 1D grid. Assuming a constant velocity for all particles, each grid point stands for one second in time, or $v_{sw} \cdot 1$ s km. The production rates P_i , P_i^+ , and P_i^{++} for neutrals, singly-, and doubly-charged particles that follow from the interaction of the solar-wind ions with the dust grains are calculated for every grid point i by

$$P_i = \sigma_i \cdot f_{sw,i} \cdot \eta \quad (5)$$

$$P_i^+ = \sigma_i \cdot f_{sw,i} \cdot \eta^+ \quad (6)$$

$$P_i^{++} = \sigma_i \cdot f_{sw,i} \cdot \eta^{++}. \quad (7)$$

The particle populations of neutrals, N_i , singly-charged ions, N_i^+ , and doubly-charged ions, N_i^{++} at each grid point i are calculated with the following formulae using the production rates above and the photo-ionisation rates v_i and v_i^+ :

$$N_i = N_{i-1} + P_i - N_{i-1} \cdot v_{i-1}$$

$$N_i^+ = N_{i-1}^+ + P_i^+ + N_{i-1} \cdot v_{i-1} - N_{i-1}^+ \cdot v_{i-1}^+$$

$$N_i^{++} = N_{i-1}^{++} + P_i^{++} + N_i^+ \cdot v_{i-1}^+.$$

3.3. Composition comparison

We chose the solar-wind composition given in Table 4 as the initial composition of the particles. The given errors are the propagated errors from the initial elemental solar-wind composition values. With the toy model, the expected inner-source

PUI composition was calculated for three different parameter sets of D , scaling the dust cross-section, and r_{\min} :

1. $r_{\min} = 30 R_\odot$; $D = -1$;
2. $r_{\min} = 30 R_\odot$; $D = -1.3$;
3. $r_{\min} = 4 R_\odot$; $D = -1.3$.

The first two parameter sets with $r_{\min} = 30 R_\odot$ are chosen following Schwadron et al. (2000), who propose that the peak of inner-source PUI production should be located within 10–50 R_\odot . The scaling of the dust cross-section is based on the density distribution of the dust and, on the one hand, taken from the theoretical value of $D = -1$ considering only Poynting-Robertson drag and, on the other, from the empirically found value of $D = -1.3$ (Leinert et al. 1978). In the simulation results, one can see that the variation in this parameter only results in very small differences in the simulation results. The third parameter set shows an extreme case. Kimura et al. (1997) found that carbon aggregates with small impurities sublime at $4 R_\odot$ from the Sun, and this is used for r_{\min} . The results for the inner-source PUI composition and the charge-state distributions at 1 AU are shown in Table 4 for all parameter sets.

In all results, the N^+ , O^+ , and Ne^+ abundance ratios with respect to C^+ are significantly lower than the corresponding elemental solar-wind values, whereas the Mg^+ and Si^+ ratios are increased with respect to the solar-wind ratios. In the measured inner-source heavy PUI composition, a similar behaviour can be found, except for N^+ . One possible reason for this is that the N^+ peak is likely to contain Si^{2+} counts that cannot be distinguished from N^+ counts owing to having the same M/Q and similar energy loss in the carbon foil. Furthermore, the model's results show an abundance of Si^{2+} of comparable order to Mg^{2+} , which supports this explanation.

From the quantitative point of view, the deviations of the model results and the measurements depend on the parameters of the model. The first two parameter sets reproduce the O^+/C^+ ratio well, but fail to reproduce the Ne^+/C^+ and Si^+/C^+ ratio that matches the third parameter set better. However, the measured Si^+ abundance is possibly affected by a large systematic error, and the Ne^+ abundance contains a contribution of ions with an interstellar origin. Owing to neon's very high first ionisation potential, interstellar neon atoms can approach close to the Sun before getting ionised (Drews et al. 2012). When these particles cool adiabatically before reaching 1 AU, we cannot distinguish between inner-source and interstellar Ne^+ ions. The Mg^+/C^+ and the Mg^{2+}/C^+ ratio are in reasonable agreement with all parameter sets when keeping in mind that the error of the Mg^{2+} abundance is greater than given in the table because of subtracting background counts. Considering the charge-state distributions at 1 AU that result from the toy model, it is worth mentioning that a significant neutral component is calculated for all parameter sets.

3.4. Solar-wind-speed dependence

In Table 5 the first two columns summarise results for the inner-source O^+/C^+ ratio at different solar-wind speeds. These consist of ratios obtained in this study ($v_{sw} \leq 537 \text{ km s}^{-1}$) and the result by Allegrini et al. (2005) that was measured at a solar-wind speed of about 750 km s^{-1} . The value of Gloeckler et al. (2000) was derived in solar-wind speeds from 318 km s^{-1} to 864 km s^{-1} and thus represents an average value for the solar-wind-speed-dependent O^+/C^+ ratio. It can be seen that both formerly obtained values fit the newly observed trend of the

Table 5. Abundance ratios of C^+/O^+ in $w = 0.8$ to $w = 1.2$ compared to the model results at varying solar-wind speeds.

Solar-wind speed [km s ⁻¹]	O^+ / C^+	$r_{\min} = 30 R_\odot, D = -1$	$r_{\min} = 30 R_\odot, D = -1.3$	$r_{\min} = 4 R_\odot, D = -1.3$
≤ 350	0.49 ± 0.06	0.63 ± 0.08	0.65 ± 0.08	0.82 ± 0.11
350–400	0.58 ± 0.02	0.64 ± 0.08	0.66 ± 0.08	0.84 ± 0.11
400–450	0.70 ± 0.04	0.66 ± 0.08	0.68 ± 0.08	0.85 ± 0.11
450–500	0.82 ± 0.05	0.69 ± 0.09	0.70 ± 0.09	0.86 ± 0.11
500–537	0.95 ± 0.19	0.72 ± 0.09	0.73 ± 0.09	0.87 ± 0.12
750	0.99 ± 0.15^a	0.91 ± 0.12	0.90 ± 0.12	0.93 ± 0.12

Notes. ^(a) From Allegri et al. (2005).

O^+/C^+ ratio with increasing solar-wind speed obtained by CTOF very well.

Columns 3–5 of Table 5 show the toy model predictions for the O^+/C^+ ratio as a function of the solar-wind velocity with the same parameter sets used in the previous section. In all cases, we observed a slight increase in the O^+/C^+ ratio with solar-wind speed. Although the increase is not as steep as in the data, the trend is reproduced. The increase in the model values is mainly related to the primary production of the ions. Allegri et al. (2014) measured the charge-state fractions of carbon and oxygen ions after the passage through very thin carbon foils at different ion energies. It was found that the fraction of O^+ ions after the foil shows a stronger increase with energy than the fraction of C^+ ions in the considered ion speed range, which would lead to the observed trend of the O^+/C^+ ratio.

4. Conclusion

We used data from the Charge-Time-Of-Flight sensor on-board SOHO to study the composition of inner-source PUIs. Previous studies have claimed that this composition is similar to the solar-wind composition, even though there were significant deviations. Our study that is based on ~42 000 counts compared to ~800 counts and ~250 counts of Gloeckler et al. (2000) and Allegri et al. (2005), respectively, confirmed these results. In particular, the large deviation of the O^+/C^+ from the solar-wind oxygen-to-carbon ratio remained. Furthermore, we could show that the deviation of the O^+/C^+ as measured by Gloeckler et al. (2000) and Allegri et al. (2005) is due to a systematic increase with solar-wind speed. This signature has not been reported before and constitutes another observational constraint for the production scenarios of inner-source PUIs.

To explain the compositional deviation and the newly found solar-wind speed dependence, a simple model has been set up based on the production mechanism proposed by Wimmer-Schweingruber & Bochsler (2003). This model includes the production of inner-source PUIs by the interaction of solar-wind ions with dust, resulting in neutral or low-charged particles and photo-ionisation. Owing to these processes, the formerly solar-wind ions can either contribute to a neutral, singly-, or doubly-charged population that is radially moving outwards with solar-wind speed. The distribution of charge states after passing the dust strongly depends on the element, as does the photo-ionisation rate. Our model predicts different charge-state distributions at 1 AU for every element. Thus, we do not expect the singly-charged population, which we observe, to reflect the elemental solar-wind composition. We point out that the model also predicts non-negligible populations of neutral

and doubly-charged particles co-moving outwards with the solar wind. Thus the inner source might also be a direct source for energetic neutral atoms. Future observations of inner-source neutrals may constitute a unique opportunity to further constrain the production mechanisms of inner-source PUIs.

The simple nature of our model leads us not to claim full quantitative accuracy. The main uncertainty of the model stems from the poorly known characteristics of the dust population within 1 AU. Especially the chemical composition, dust grain geometry, and the spatial distribution inside 1 AU are important factors for our model, where no reliable constraints exist to our knowledge. Nevertheless, the model results show that the deviation of the measured inner-source PUI composition and the elemental solar-wind composition can be explained with the interplay of solar-wind-dust interaction and photo-ionisation. Furthermore, the increase in the O^+/C^+ ratio at higher solar-wind speeds can be reproduced qualitatively. Overall, our findings suggest that the production scenario proposed by Wimmer-Schweingruber & Bochsler (2003) is the main driver in the production of inner-source PUIs.

Acknowledgements. We gratefully acknowledge use of Proton Monitor data that has been provided by the SOHO archive. This work was supported by the German Space Agency (DLR) under grant number 50 OC 1103 and by the University of Kiel.

References

- Allegri, F., Schwadron, N., McComas, D., Gloeckler, G., & Geiss, J. 2005, *J. Geophys. Res.: Space Phys.*, **110**
- Allegri, F., Ebert, R. W., Fuselier, S. A., et al. 2014, *Opt. Engineering*, **53**, 024101
- Berger, L., Drews, C., Taut, A., & Wimmer-Schweingruber, R. 2013, in *AIP Conf. Proc.*, **1539**, 386
- Berger, L., Drews, C., Taut, A., & Wimmer-Schweingruber, R. 2015, *A&A*, **576**, A54
- Bochsler, P. 2007, *A&ARv*, **14**, 1
- Bochsler, P., Möbius, E., & Wimmer-Schweingruber, R. 2006, *Geophys. Res. Lett.*, **33**
- Bochsler, P., Möbius, E., & Wimmer-Schweingruber, R. F. 2007, in *ESA SP*, **641**, 47
- Bürgi, A., Gonin, M., Oetliker, M., et al. 1993, *J. Appl. Phys.*, **73**, 4130
- Bzowski, M., & Królikowska, M. 2004 [[arXiv:astro-ph/0405148](https://arxiv.org/abs/astro-ph/0405148)]
- Drews, C., Berger, L., Wimmer-Schweingruber, R. F., et al. 2010, *J. Geophys. Res.: Space Phys.*, **115**
- Drews, C., Berger, L., Wimmer-Schweingruber, R. F., et al. 2012, *J. Geophys. Res.: Space Phys.*, **117**
- Geiss, J., Gloeckler, G., Fisk, L., & Steiger, R. V. 1995, *J. Geophys. Res. Space Phys.*, **100**, 23373
- Geiss, J., Gloeckler, G., & Von Steiger, R. 1996, in *The Heliosphere in the Local Interstellar Medium* (Springer), 43
- Gloeckler, G., Fisk, L., Geiss, J., Schwadron, N., & Zurbuchen, T. 2000, *J. Geophys. Res. Space Phys.*, **105**, 7459

- Gonin, M., Kallenbach, R., & Bochsler, P. 1994, *Nucl. Instr. Methods Phys. Res. Sect. B: Beam Interactions with Materials and Atoms*, **94**, 15
- Gonin, M., Kallenbach, R., Bochsler, P., & Bürgi, A. 1995, *Nucl. Instr. Meth. Phys. Res. Sect. B: Beam Interactions with Materials and Atoms*, **101**, 313
- Grünwaldt, H., Neugebauer, M., Hilchenbach, M., et al. 1997, *Geophys. Res. Lett.*, **24**, 1163
- Hefti, S. 1997, Ph.D. Thesis, Universität Bern
- Hovestadt, D., Hilchenbach, M., Bürgi, A., et al. 1995, *Sol. Phys.*, **162**, 441
- Kimura, H., Ishimoto, H., & Mukai, T. 1997, *A&A*, **326**, 263
- Leinert, C., Hanner, M., Link, H., & Pitz, E. 1978, *A&A*, **64**, 119
- Mann, I., & Czechowski, A. 2005, *ApJ*, **621**, L73
- Möbius, E., Hovestadt, D., Klecker, B., Scholer, M., & Gloeckler, G. 1985, *Nature*, **318**, 426
- Schwadron, N., Geiss, J., Fisk, L., et al. 2000, *J. Geophys. Res. Space Phys.*, **105**, 7465
- Shearer, P., von Steiger, R., Raines, J. M., et al. 2014, *ApJ*, **789**, 60
- Taut, A. 2014, Master's Thesis, Institute for Experimental and Applied Physics, Christian-Albrechts-University of Kiel
- Verner, D., Ferland, G., Korista, K., & Yakovlev, D. 1996 [[arXiv:astro-ph/9601009](https://arxiv.org/abs/astro-ph/9601009)]
- Von Steiger, R., Schwadron, N., Fisk, L., et al. 2000, *J. Geophys. Res.*, **105**, 27217
- Wiens, R. C., Bochsler, P., Burnett, D. S., & Wimmer-Schweingruber, R. F. 2004, *Earth Planet. Sci. Lett.*, **226**, 549
- Wimmer-Schweingruber, R. F., & Bochsler, P. 2003, *Geophys. Res. Lett.*, **30**
- Wimmer-Schweingruber, R. F., Bochsler, P., Kern, O., Gloeckler, G., & Hamilton, D. C. 1998, *J. Geophys. Res. Space Phys.*, **103**, 20621
- Woods, T. N., Bailey, S., Eparvier, F., et al. 2000, *Phys. Chem. Earth, Part C: Solar, Terrestrial & Planetary Science*, **25**, 393
- Ziegler, J. F., Ziegler, M., & Biersack, J. 2010, *Nucl. Instr. Methods Phys. Res. Sect. B: Beam Interactions with Materials and Atoms*, **268**, 1818

3.3 FOLLOW-UP INVESTIGATIONS

3.3.1 Identification of Mg^{2+}

The majority of PUIs is singly charged, because once they are ionized they are transported outwards by the solar wind and its embedded IMF, where decreased ionization rates are expected due to the larger heliocentric distance. Nevertheless, there is a non-zero probability for PUIs to experience a second ionization process. The result is a doubly charged PUI, of course. This may be especially relevant for elements with a low first ionization potential like magnesium or silicon. Magnesium and silicon are also components of the heavy solar wind ions, but as all heavy solar wind ions they are highly charged and commonly appear as Mg^{7+} - Mg^{10+} and Si^{7+} - Si^{11+} (e.g. Berger et al. (2011)). Therefore, it is safe to assume that Mg^{2+} or Si^{2+} are doubly charged PUIs that must have been created in interplanetary space. In the simulation results of the solar wind neutralization scenario in Tab. 4 in Taut et al. (2015), a non-negligible amount of Mg^{2+} and Si^{2+} is predicted and Mg^{2+} has already been considered in the fit of the M/Q histograms. Here, we provide a more thorough identification of Mg^{2+} , which indicates that indeed doubly charged PUIs have been observed.

In terms of M/Q one cannot distinguish between C^+ and Mg^{2+} as both have a value of 12 amu e⁻¹. The M/Q is calculated from the sensor's E/Q step and the measured ToF. However, at a given E/Q step Mg^{2+} shows a slightly smaller ToF than C^+ due to its decreased relative energy loss in the sensor's carbon foil. Thus, the calculated M/Q of Mg^{2+} ions, assuming the energy loss of C^+ as it was done in Taut et al. (2015), is expected to be lower than 12 amu e⁻¹ (see Table 1 of publication).

In the M/Q histograms considering heavy PUI data, one can surmise a small bump next to the pronounced C^+ peak, where we would expect the Mg^{2+} counts (see Fig. 14 left). Especially in the histogram of counts which triggered an SSD

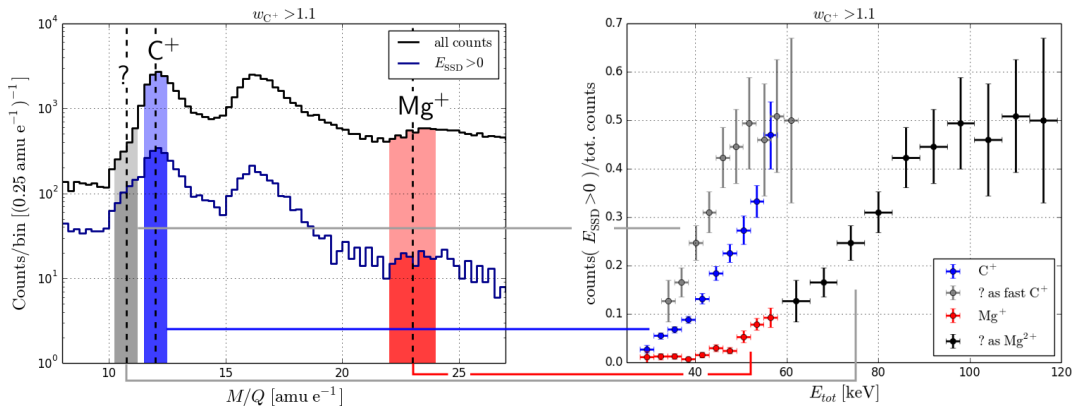


Figure 14: Identification of Mg^{2+} by evaluating the triple coincidence efficiency. *Left panel:* M/Q histograms of all data with $w_{C^+} > 1.1$ and sorted for counts that triggered an SSD signal with the same condition. The M/Q boxes utilized for the ion identification are illustrated. *Right panel:* Derived SSD efficiencies for C^+ , Mg^+ and the counts that we anticipate to be Mg^{2+} as singly- and doubly-charged ion.

signal this bump seems to be more pronounced. To distinguish, whether this peak is due to Mg^{2+} ions or just fast C^+ ions that did not loose a high amount of energy in the carbon foil, we consider the [SSD](#) efficiency of the two ion species.

For this, we filter the data for $w_{\text{C}^+} > 1.1$ to suppress the solar wind background counts that superpose the considered peaks at lower speeds. Then, we perform a simplified ion identification of C^+ , Mg^+ and what we anticipate to be Mg^{2+} by just assigning all counts within the M/Q range of $\pm 0.5 \text{ amu e}^{-1}$ for C^+ and the unknown ion, and $\pm 1 \text{ amu e}^{-1}$ for Mg^+ from the expected value to the corresponding species. Finally, we test how many counts of the individual species triggered an [SSD](#) signal at a certain energy. The ratio of all measured counts to the ones that triggered an [SSD](#) signal serves as a proxy for the [SSD](#) efficiency.

The probability to trigger an [SSD](#) signal depends on the energy and species of the incoming ion. Therefore, we consider this proxy for the [SSD](#) efficiency as a function of total energy of the ion before reaching the carbon foil of [CTOF](#)'s [ToF](#) chamber. To calculate this energy from the E/Q step of the electrostatic analyzer and the post-acceleration voltage U_{pa} , one requires knowledge about the ion's charge state as $E_{\text{tot}} = (E/Q + U_p) \cdot Q$. As this is what we aim to find out for the ion species in question, we plot the efficiency of this species over total energy on the one hand as if it was a singly charged ion, and on the other hand as if it was a doubly charged ion. Then, we can compare how this efficiency relates to the efficiency of C^+ and Mg^+ , respectively.

In Fig. 14 this scheme and the results are displayed. One can see that the [SSD](#) efficiency of the unknown species would be about a factor of two larger than the efficiency of C^+ , if it was a singly charged ion. On the other hand, if we assume that the unknown ion species corresponds to Mg^{2+} the [SSD](#) efficiency matches very well with the efficiency of Mg^+ . All this indicates, that the small peak on the left-hand side of the C^+ peak is caused by Mg^{2+} counts, that were not taken into account in former studies.

Unfortunately, this analysis cannot be repeated for the identification of Si^{2+} as the expected position of this species is superposed by the M/Q distributions of C^+ and N^+ . As Si^+ is also expected to have a lower [SSD](#) efficiency than Mg^+ it is possible that the Si^{2+} efficiency cannot be distinguished from the C^+ or N^+ efficiency. Nevertheless, the presence of Mg^{2+} indicates that also Si^{2+} may have been measured, which means that the N^+ abundance derived in [Taut et al. \(2015\)](#) is underestimated as the corresponding M/Q distributions may be contaminated by Si^{2+} counts.

Finally, the observation of doubly charged [PUIs](#) is another argument for the solar wind neutralization scenario proposed by [Wimmer-Schweingruber and Bochsler \(2003\)](#). This scenario favors the production of doubly charged ions, because solar wind ions must not necessarily loose all of their charge while passing through a dust grain. For example, in [Allegrini et al. \(2014\)](#) it is observed that a significant fraction of charged ions is not neutral when passing a thin carbon foil which is similar to the penetration through a dust grain in interplanetary space. Thus, by this process singly-charged and even doubly-charged ions can be created directly, which both leads to an enhanced abundance of doubly charged [PUIs](#).

3.3.2 Modeling of the Inner Source

A tool to study the theoretical VDF of PUIs is provided by the Earth-Moon-Mars Radiation Environment Module ([EMMREM](#)) framework and in particular its Energetic Particle Radiation Environment Module ([EPREM](#)). This code numerically solves the focused transport equation and convection-diffusion equation along an ideal Parker field line (see [Schwadron et al. \(2010\)](#) and references therein). It incorporates the processes that are believed to be most relevant for the evolution of the PUI VDF: pitch-angle scattering, adiabatic focusing, and cooling. With the help of this tool, the PUI VDF can be simulated under various conditions: For example, studies have been performed investigating the variability of the PUI VDF under certain solar wind conditions ([Chen et al., 2015](#)) or considering PUI transport effects and its impacts on the determination of λ_{flow} from the flux increase in the focusing cone ([Quinn et al., 2016](#)).

A more recent approach performed by P. Quinn from the University of New Hampshire focuses on the simulation of the C^+ and O^+ VDF. As C^+ almost exclusively stems from the inner-source, a model for the inner-source PUI production is incorporated into the simulation code. As source function for the inner-source PUIs, a dust grain population interacting with the solar wind is modeled. For the interaction of the solar wind ions with the dust grains the [TRIM](#) software ([Ziegler and Biersack, 2008](#)) is involved. As processes creating neutrals from dust the solar wind neutralization, solar wind recycling, and sputtering of grain material are considered. The solar wind neutralization scenario is divided into the originally proposed picture, where solar wind ions pass through dust grains, and backscattering of ions, which means that the ions penetrate the dust particles, are deflected more than 90° in direction and then exit the particle again as neutral or lowly-charged ion. The software keeps track of the creation mechanism of individual ions and, thus, the different VDFs resulting from these production mechanisms can be compared. The resulting 1D projected VDFs are compared to VDFs measured by [CTOF](#). For the determination of the measured VDFs of C^+ and O^+ , the ion identification developed in [Taut et al. \(2015\)](#) has been exploited. Again, the data has been split for individ-

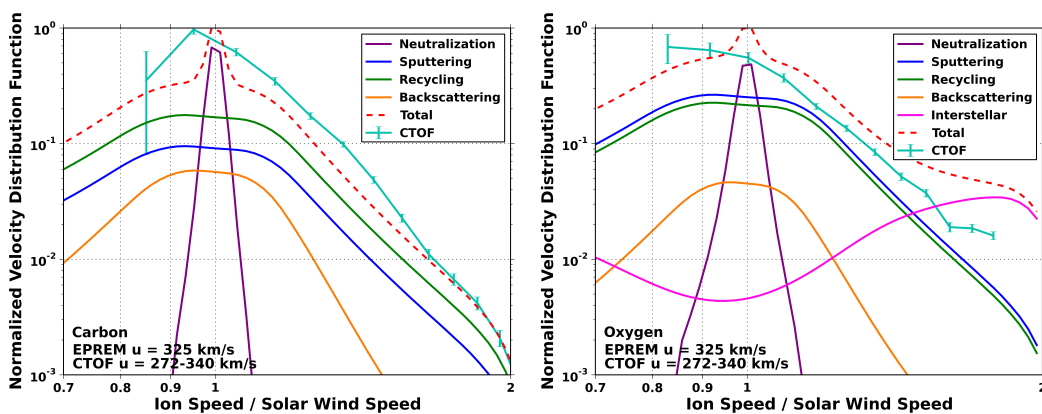


Figure 15: [EPREM](#) simulation results for the C^+ (left panel) and O^+ (right panel) VDF at 1 AU from various production mechanisms compared to the measured VDF of the corresponding ion species derived from [CTOF](#) data.

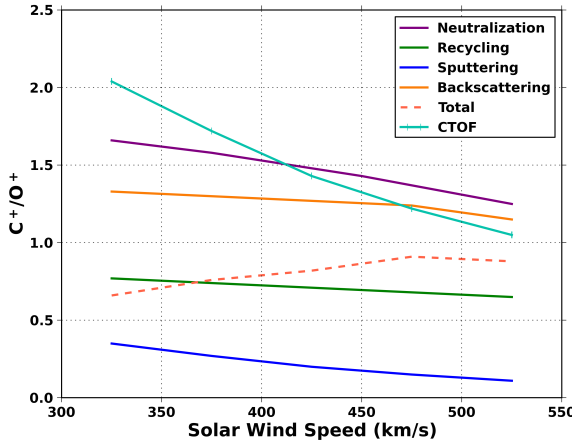


Figure 16: Simulated C^+/O^+ abundance ratio in the speed range $0.8 < w < 1.2$ as a function of solar wind speed for various inner-source PUI production mechanisms. For comparison also the observed ratios presented in Taut et al. (2015) are displayed.

ual speed ranges in terms of w_{C^+} and in each range, a fit of the M/Q histogram has been applied to derive the count rate of C^+ and O^+ in the corresponding velocity range. This count rate is then corrected for the sensor's detection efficiency corresponding to the considered ion species and speed range. Furthermore, a correction converting the count rates into an equivalent to the phase-space density needs to be applied. At higher speeds, one measurement cycle of CTOF can detect PUIs that originate from a bigger spatial volume, which results in a necessary correction with v_{ion} . Additionally, the sensor's velocity coverage correponds to a part of a spherical shell with a width proportional to v_{ion} , which means that the total velocity space volume covered at a given speed v_{ion} is proportional to v_{ion}^3 . Thus, the count rates are corrected with a weighting corresponding to v_{ion}^4 . The result is not an absolute phase-space density, but it is proportional to it. Thus, only the shape of the simulated and the observed VDFs can be compared. Furthermore, the simulation obtains the abundance ratio of O^+ to C^+ in the range of $0.8 < w < 1.2$. By varying the solar wind speed one can compare these ratios with the results displayed in Tab. 3 of Taut et al. (2015).

In Fig. 15 the preliminary simulation results for the C^+ and O^+ VDF are displayed. For both ion species, it is found that the VDF expected from the originally proposed solar wind neutralization scenario (Wimmer-Schweingruber and Bochsler, 2003) is substantially narrower than the observed inner-source VDF. In contrast to that, the width of the VDF expected for the solar wind recycling scenario (Schwadron et al., 2000), sputtering, and backscattering matches the observed VDF shape comparatively well. However, it is worth noting that a broadening of the VDF expected from the solar wind neutralization scenario can easily be achieved by considering a different dust geometry, which would result in larger energy losses of penetrating solar wind ions.

The observed shoulder in the O^+ VDF fits well to the modeled VDF of interstellar O^+ . As expected, the modeled contamination of the inner-source O^+ abundance in the $0.8 < w < 1.2$ range due to interstellar O^+ is negligible as in this speed range the phase-space density of interstellar O^+ is about two orders of magnitude below the density of the modeled inner-source O^+ .

In Fig. 16 the simulated C^+/O^+ abundance ratio in the speed range $0.8 < w < 1.2$ as a function of solar wind speed is shown. The solar wind recycling scenario and the sputtering process predict C^+/O^+ abundance ratios below one

and the decrease of this ratio with solar wind speed is not as steep as the observed trend. The solar wind neutralization scenario including backscattering predicts a C⁺/O⁺ abundance ratio greater than one. The trend with solar wind speed is also not as steep as the observed trend, but still these production scenarios match this observation substantially better.

The major problem in this simulation is again the modeled dust population. The only dust quantity that can be measured in space is the mass of the dust grains. All other information about the composition or geometry of interplanetary dust stems from the evaluation of collected samples in the near-Earth environment or micrometeorites preserved in the Antarctic or Greenland ice (Grün et al., 2012). Therefore, a lot of assumptions need to be made modeling the interplanetary dust especially near the Sun, where very limited information about the dust grains is available. A more elaborate discussion of the results and the involved uncertainties will be published in Quinn et al. (2018).

3.3.3 Summary

In Tab. 3 a compilation of all proposed inner-source PUI production scenarios to date and their relation to the measured properties of inner-source PUIs is shown. It appears that the main driver of the inner-source PUI production is likely to be the solar wind neutralization mechanism proposed by Wimmer-Schweingruber and Bochsler (2003). None of the observed properties directly excludes this scenario, even though this scenario can only explain certain properties assuming a special dust geometry.

For example, it is not completely ruled out, if the observed stability of inner-source PUI flux over the solar cycle cannot be explained by this scenario. If one argues that not nanometer-sized dust, but larger dust grains with fractal geometry are responsible for the solar wind neutralization, a significantly less pronounced dependence of the inner-source PUI flux with the solar cycle is expected. A population of larger dust grains is expected to be less influenced by CMEs as their M/Q ratio is believed to be too low for an efficient interaction. This would then also explain the observed VDF that did not match to the expected VDF from a production by the penetration through thin dust grains. For larger dust grains with fractal geometry, the ions have multiple possibilities of passing through the grain. Some of those will result in a substantially larger energy loss, which would then result in a broadening of the VDF.

Another possibility is, that there might be at least two dominant sources for inner-source PUIs and the combination of these sources leads to the observed properties. Still, all proposed processes are likely to happen within the heliosphere. However, it is also likely that most of these processes are negligible and that only one or two processes significantly contribute to the observed inner-source PUI flux.

Table 3: Compilation of proposed inner-source PUI scenarios vs. observational constraints these scenarios need to explain adapted from Allegrini et al. (2005). The table has been expanded for scenario 5 proposed by Schwadron and McComas (2010) and the three new observational constraints reported in Berger et al. (2015), Taut et al. (2015), and Drews et al. (2016).

	Scenario 1 SW recycling	Scenario 2 SW neutralization	Scenario 3 Sungrazing comets	Scenario 4 Dust-dust collisions	Scenario 5 Energetic neutrals
Observed composition	Possibly ^a	Yes	No ^b	No ^b	No ^c
Observed VDF	Yes	Possibly ^d	Possibly	Possibly	No
Large PUI flux	Unlikely ^e	Possibly	Possibly	Possibly	Yes
Randomly distributed source	Yes	Yes	No	Yes ^f	Possibly
Stability over solar cycle	Yes	Possibly ^g	Yes	Possibly	Possibly
O ⁺ -O ⁶⁺ flux correlation	Unlikely ^h	Yes	No	No	No
Increasing O ⁺ /C ⁺ with v_{sw}	Possibly ⁱ	Yes	No	No	No
Production at 1 AU	Possibly	Possibly	No	Possibly	Yes

^a Success of this scenario requires a very low sputtering yield.

^b Depleted in Ne, rich in C, Si, Mg, Fe.

^c Scenario predicts a negligible amount of Si due to high ionization rates (Bochsler and Möbius, 2010).

^d Success of this scenario requires a large energy loss of the passing ion in the dust grain or a substantial deflection in direction (backscattering).

^e Grains efficiently scatter light and would yield a cross section two decades higher than observed from zodiacal light.

^f However, peaks at low latitude.

^g Success of this scenario requires that CMEs do not trap nanometer-sized grains or that highly fractal grains also serve as thin foils.

^h Requires a correlation of the sputtering yield of O from dust grains with the O⁶⁺ flux and a rapid ionization and pickup process.

ⁱ However, simulations predict a C⁺/O⁺ ratio below one.

4

THE PICKUP ION TORUS VDF OBSERVED WITH CELIAS/CTOF

Due to the pickup process, PUIs are injected into the solar wind plasma with a highly anisotropic VDF that has the shape of a torus in velocity space. The orientation of the torus is always perpendicular to the ambient IMF orientation. In [Vasyliunas and Siscoe \(1976\)](#) the authors argue that this initial anisotropic VDF is rapidly transformed into an isotropic VDF as such a VDF is unstable with respect to the generation of waves inside the solar wind plasma. Furthermore, fluctuations of the IMF cause pitch-angle scattering, which also leads to a more isotropic PUI VDF. However, [Möbius et al. \(1998\)](#) reported that measurements of the 1D projection of the He⁺ PUI VDF show a systematic variability with IMF orientation, which indicates that the PUI VDF is anisotropic. This has been attributed to a model by [Isenberg \(1997\)](#), who claims that the pitch-angle of PUIs only very inefficiently scatters through 90°. Thus, only one hemisphere of velocity space becomes isotropic rapidly. In [Oka et al. \(2002\)](#) the observation of a torus-like VDF of He⁺ PUIs has been reported for the first time, which has challenged the assumption of rapid pitch-angle scattering. These observations have been supported by [Drews et al. \(2013\)](#), who directly linked the variability of the 1D projected He⁺ VDF to the observed IMF orientation at 1 AU. Also measurements closer to the Sun at 0.3 AU performed by the MErcury Surface, Space ENvironment, GEochemistry and Ranging ([MESSENGER](#)) spacecraft provided confirmation that the PUI VDF does not instantaneously become isotropic ([Gershman et al., 2014](#)). With a complex analysis utilizing the position sensitive detection system of PLASTIC, [Drews et al. \(2015\)](#) showed that a clear signature of the initial torus VDF is visible in the observed 2D He⁺ VDF at 1 AU. Furthermore, it has been found that at lower speeds PUIs tend to stream along the IMF lines, which also contradicts isotropy. After all, the anisotropy of the PUI VDF is also connected to the cooling behaviour of PUIs (see Sec. 1.6.3) and thus it significantly contributes to the evolution of the PUI VDF.

Recently, the anisotropy of PUI VDFs gained further relevance. [IBEX](#) observed an enigmatic ribbon of enhanced energetic neutral intensity that spans the whole sky. There are multiple theories that claim that PUIs that charge-exchange and are converted into energetic neutrals are responsible for this signature (see [McComas et al. \(2011\)](#)). One of the most promising theories considers PUI charge-exchange in the LISM ([Heerikhuisen et al., 2009](#)), but it requires that the initial torus VDF is stable over a prolonged time, which is currently under debate ([Florinski et al., 2010](#)). Anyhow, although there are substantial differences in the background medium comparing the solar wind in the inner heliosphere and the LISM, the fact that the initial PUI VDF is more stable than assumed in the solar wind could provide clues for the stability of this VDF in the LISM.

In this chapter, we aim to contribute to Question 2: *What is the 3D VDF of PUIs at 1 AU and what are the implication for the stability of a torus VDF within the dynamic solar wind?* Again, we utilize CTOF data, but this time we only consider He⁺ and

no heavy PUIs. Complementary to former studies, we investigate how the He⁺ PUI VDF changes with IMF orientation. As SOHO does not carry a magnetometer, data of Wind/MFI had to be utilized that has been extrapolated to the location of SOHO.

4.1 BRIEF SUMMARY OF THE PUBLICATION

After the context of this study is introduced, the details of the data analysis are described. For the PUI VDF measurements CTOF data is utilized and the identification of He⁺ ions in the CTOF data set is outlined. The IMF orientation is taken from MFI on Wind, which was also located in an orbit around in the considered time period. We assume the IMF to be frozen into the solar wind and then calculate the time it takes the solar wind to carry the IMF from one spacecraft to the other. Additionally, we introduce criteria to decide whether to trust this extrapolation or not. In times, where strong fluctuations of the IMF are observed at the location of Wind, the extrapolated IMF at the location of SOHO is likely not to be valid.

In total, four projected 1D VDFs are derived and compared in this publication, that correspond to four different ranges of IMF orientation. Firstly, we define the angles Φ and Θ that can be calculated from the measured IMF vector, with that one can distinguish between IMF configurations, in which the initial torus VDF falls into CTOF's FoV and those, where this torus is outside the FoV. Then, the ranges of Φ and Θ are given, that correspond to the IMF orientations that are investigated.

It is found that the observed variation of projected 1D He⁺ VDF is consistent with the picture of an initial torus distribution moving through CTOF's FoV as a function of IMF orientation. This complements on the previous studies. Furthermore, an anisotropy of the PUIs that must have undergone an acceleration process is observed. This suggests, that accelerated PUIs preferentially stream along the IMF lines, which may have implications for the acceleration mechanisms.

4.2 PUBLICATION

The following article is reproduced from Taut et al. (2016) with the permission of AIP Publishing. The article is a peer reviewed proceedings to the Solar Wind 14 conference, that took place in Weihai, China, in June 2015.

Observations of the He⁺ pickup ion torus velocity distribution function with SOHO/CELIAS/CTOF

A. Taut, L. Berger, P. Bochsler, C. Drews, B. Klecker and R. F. Wimmer-Schweingruber,
AIP Conference Proceedings, 1720, 050001 (2016), DOI: 10.1063/1.4943835

Own contribution: 90%

Observations of the He⁺ Pickup Ion Torus Velocity Distribution Function with SOHO/CELIAS/CTOF

Andreas Taut^{1,a)}, Lars Berger¹, Peter Bochsler², Christian Drews¹, Berndt Klecker³
and Robert F. Wimmer-Schweingruber¹

¹*Institut für Experimentelle und Angewandte Physik, Christian-Albrechts-Universität zu Kiel, Leibnizstrasse 11,
24118 Kiel, Germany*

²*Physikalisches Institut, Universität Bern, Sidlerstrasse 5, 3012 Bern, Switzerland*

³*Max-Planck-Institut für extraterrestrische Physik, Giessenbachstrasse 1, 85748 Garching, Germany*

^{a)}Corresponding author: taut@physik.uni-kiel.de

Abstract. Interstellar PickUp Ions (PUIs) are created from neutrals coming from the interstellar medium that get ionized inside the heliosphere. Once ionized, the freshly created ions are injected into the magnetized solar wind plasma with a highly anisotropic torus-shaped Velocity Distribution Function (VDF). It has been commonly assumed that wave-particle interactions rapidly destroy this torus by isotropizing the distribution in one hemisphere of velocity space. However, recent observations of a He⁺ torus distribution using PLASTIC on STEREO showed that the assumption of a rapid isotropization is oversimplified. The aim of this work is to complement these studies. Using He⁺ data from the Charge Time-Of-Flight (CTOF) sensor of the Charge, EElement, and Isotope Analysis System (CELIAS) on-board the SOlar and Heliospheric Observatory (SOHO) and magnetic field data from the Magnetic Field Investigation (MFI) magnetometer of the WIND spacecraft, we derive the projected 1-D VDF of He⁺ for different magnetic field configurations. Depending on the magnetic field direction, the initial torus VDF lies inside CTOF's aperture or not. By comparing the VDFs derived under different magnetic field directions with each other we reveal an anisotropic signature of the He⁺ VDF.

INTRODUCTION

PickUp Ions (PUIs) in the heliosphere are former neutrals that have been ionized by solar EUV radiation, charge-exchange with solar wind protons, or electron impact. The most common seed population of PUIs are neutrals from the interstellar medium that penetrate the heliosphere unimpeded by electro-magnetic forces. Interstellar PUIs were first observed by Möbius *et al.* [1] using data from the AMPTE spacecraft and their nature has been a subject to research ever since (cf. [2]). The neutrals have commonly a very low speed compared to the solar wind, which leads to an anisotropic initial Velocity Distribution Function (VDF) once the neutrals are ionized. They are forced on gyro orbits perpendicular to the ambient magnetic field that is swept outward with the solar wind. Thus the initial VDF resembles the form of a torus in velocity space (cf. Drews *et al.* [3]). Considering a perpendicular magnetic field configuration the speed of PUIs in the spacecraft frame of reference would range between $w \doteq \frac{v_{\text{ion}}}{v_{\text{sw}}} \approx 0$ and $w \approx 2$, which is why PUI VDFs show a strict cutoff at $w \approx 2$.

This torus VDF is then altered by wave-particle interactions and cooling processes. Wave-particle interactions can change the pitch-angle of PUIs which leads to an isotropization of the VDF. It has been commonly assumed that the isotropization happens on a short timescale compared to the time it takes the PUIs to reach the observer. Therefore, observations of an anisotropy in He⁺ VDFs were previously attributed to inefficient pitch-angle scattering across 90° [4]. But studies of Oka *et al.* [5] and Drews *et al.* [6] showed that the anisotropy stems from locally ionized PUIs that are not yet isotropized and still exhibit a torus-like VDF.

DATA ANALYSIS

The aim of this study is to show that an anisotropic torus feature of the He⁺ PUI VDF is also observed with the CTOF sensor on-board SOHO. To this aim we combine data measured by the CTOF sensor with data provided by the MFI instrument of the nearby WIND spacecraft.

He⁺ Pickup Ion Data

CTOF is a linear time-of-flight mass spectrometer which measures energy-per-charge, time-of-flight and residual energy of incoming ions which can then be converted into their mass-per-charge, mass, and energy. A more detailed description of the CTOF sensor can be found in Hovestadt *et al.* [7]. Due to the rather short operation time of CTOF, only data from day of year 150 to 220, 1996, is used. During this time SOHO was located at the upwind side of the sun with respect to the interstellar neutral flow, the region of PUI crescent [8]. CTOF's aperture covers a field of view of ±25° in-ecliptic and ±15° out-of-ecliptic while pointing directly towards the sun. We apply the same algorithm for the conversion of energy-per-charge and time-of-flight into mass-per-charge, $\frac{M}{Q}$, values that was already used in Taut *et al.* [9], with the difference that it has been adapted to the energy loss of helium ions. Similar to the work based on data from the PLASTIC instrument on STEREO/A by Drews *et al.* [6] we identify He⁺ ions by a simple mass-per-charge box fulfilling the criterion $3.5 \leq \frac{M}{Q} \leq 4.5$. We only consider the VDF in a range between $w_{\text{He}^+} = 1.3$ and $w_{\text{He}^+} = 2.3$. At this speed range no background of prominent heavy solar wind ions is expected.

B-Field Extrapolation

The MFI instrument on-board WIND measures the magnetic field vector (for example in GSE coordinates: B_x , B_y , and B_z) at a maximum frequency of 10.9 Hz [10]. As both spacecraft, SOHO and WIND, are approximately located at L1, the magnetic field vector at the location of WIND should not be that far off the ambient magnetic field vector at the location of SOHO. However, assuming a magnetic field that is frozen into the solar wind plasma, one can calculate the time difference, Δt , with which the same magnetic field is seen by the two spacecraft by convecting the magnetic field from one spacecraft to the other (as used in e.g. Saul *et al.* [11]). We then assume the magnetic field vector measured by WIND/MFI corrected for this time difference ($\Delta t \sim 30$ min) to be valid at the location of SOHO.

To synchronize this data with the CTOF He⁺ data we calculate the mean magnetic field vector for every 5-min measurement cycle of the sensor. Additionally, we determine the magnetic field angle with respect to the axis of CTOF's aperture, which is simply $\alpha = \arccos\left(\frac{B_z}{B}\right)$. We use this quantity to further restrict the data. The magnetic field convection approach as described above yields only reasonable result if the magnetic field does not change rapidly on short timescales [12]. Thus, we removed all 5-min cycles in which the standard deviation of α exceeds 5°. Furthermore, the standard deviation of every 5-min cycle including three cycles before and after this cycle has been determined and all cycles with a value greater than 10° were dismissed. This ensures that all possible uncertainties related to the extrapolation of the magnetic field are kept at a reasonable level.

METHOD & RESULTS

The magnetic field orientation tells us if the initial torus VDF of the He⁺ PUIs can be detected with the aperture of CTOF. Using simple geometric arguments one can derive the velocity, \vec{V} , for which He⁺ PUIs that are injected into a magnetic field \vec{B} have their maximum speed in the spacecraft frame. This velocity is given by

$$\vec{V} = 2(\vec{v}_{\text{sw}} - \frac{v_{\text{sw}} B_x}{B^2} \vec{B}) \quad (1)$$

assuming a solar wind streaming radially away from the sun. We are only interested in the in- and out-of-ecliptic angles, ϕ and θ , of this velocity that, neglecting the small velocity of the neutral seed population, do not depend on the ambient solar wind speed. These angles can be calculated by

$$\phi = \arctan 2(V_y, V_x) \quad (2)$$

$$\theta = \arcsin\left(\frac{V_z}{V}\right). \quad (3)$$

Finally, we can use these angles to distinguish whether a signature of the initial torus VDF should be observed for a certain magnetic field configuration.

The initial torus VDF of He^+ ions is a 3D feature. As CTOF does not offer any information about the incident angle of measured ions we are limited to spectra that are integrated over the whole angular acceptance of the sensor. However, parts of the torus VDF are only inside CTOF's aperture during specific magnetic field orientations. This is illustrated in the three panels on the right-hand side in Fig. 1, that show the v_x - v_y plane. The expected position of the torus VDF is shown for three magnetic field configurations, and CTOF's field of view is indicated by the shaded triangle. Naturally, the count rates near the cutoff speed, $w \approx 2$, should be increased if the torus is inside the covered velocity space in contrast to configurations where it lies outside this area. In the latter case only He^+ ions that have already gone through a scattering process are measured by CTOF. We chose the magnetic field configuration according to the following conditions: the torus signature lies in the center, at the edge, or just outside the aperture. Additionally we consider magnetic field orientations where absolutely no torus distributed He^+ ions should be measured at all, which means that only ions that have already been isotropized are measured. The detailed criteria for these configurations are summarized in Tab. 1. The neutral seed population of the He^+ ions has a non-negligible speed, which effects

TABLE 1. Magnetic field configurations and corresponding positions of the He^+ torus in CTOF's aperture. These restrictions are used to create the histograms displayed in Fig. 1

Torus position	$ \phi /^\circ$	$ \theta /^\circ$
Center of aperture	0 – 7.5	≤ 10
Edge of aperture	15 – 22.5	≤ 10
Just outside	30 – 37.5	≤ 10
Outside	≥ 50	-

the cut-off of the PUI VDF. This means that for different solar wind speeds, the cut-off is located at a slightly different w value. Thus, we chose to consider only a comparatively narrow solar wind speed range. This speed range is $360 \text{ km s}^{-1} \leq v_{\text{sw}} \leq 390 \text{ km s}^{-1}$, as it offers very good counting statistics.

After the restriction of the data according to the criteria described above, w -histograms of the single data sets were created. On the one hand, these histograms were corrected for the instrumental response of CTOF, on the other hand, the number of cycles that contribute to the data set was taken into account. This ensures that the histograms can be compared to each other. These histograms are shown in the top panel of Fig. 1. To reveal the initial torus VDF, the ratio of the "Center", "Edge", and "Just outside" histogram with the "Outside" histogram is displayed in the lower panel. In the error bars shown in Fig. 1, only the pure counting error was considered, which has been propagated into the ratio of the histograms. It is obviously impossible to quantify an error for the magnetic field orientation due to the lack of a direct measurement at the location of SOHO. This, of course, introduces a systematic error, which is minimized using the restrictions given in the previous section.

One can see that during magnetic field orientations where we would expect the torus to be in the center of CTOF's aperture around 2.5 times more ions are measured around $w \approx 2$ than during orientations with the torus outside the aperture. When we expect the torus to be at the edge of the aperture this ratio is reduced, and its maximum appears to be shifted towards lower w values. The lower intensity can be explained by the width of the torus which makes it possible that a part of it is not detected by CTOF. Furthermore, in Hovestadt *et al.* [7] it can be seen that the detection efficiency of CTOF decreases with increasing deviation of the incident angle from the sun-instrument line. The shift in w can easily be explained considering the 2D velocity plots displayed on the right-hand side of Fig. 1. If the torus is not located in the center of the aperture the maximum speed of the He^+ ions in the spacecraft frame of reference decreases. When going towards lower ion speeds, the torus signature fades which may be explained by the cooling of the VDF. He^+ ions measured at lower w values have already had time to cool, which means that more time for isotropizing wave-particle interactions was available.

Considering orientations with the torus just outside the aperture, no excess at higher w values is observed, which contradicts the theory of rapid isotropization in one hemisphere of velocity space, but it can easily be explained by a He^+ torus. Furthermore, the ratio drops for high w in all curves. In this speed range the PUIs must have undergone an acceleration process, which seems to act predominantly parallel to the magnetic field (at least in our considered time period). The acceleration by turbulent field-aligned electric fields [13] could be an explanation for that.

In summary, we observe a clear anisotropy in the VDF of He^+ PUIs, which is in agreement with a torus VDF superposed over an isotropic VDF. The location of the torus in velocity space depends on the ambient magnetic field as discussed in Drews *et al.* [3]. Even though the extrapolated magnetic field for the location of SOHO introduces some uncertainty, we were able to confirm previous studies with our new data set. Our results challenge the assumption of rapid pitch-angle isotropization which is commonly made in PUI transport models (e.g. [14]), as this is not in agreement with our observations.

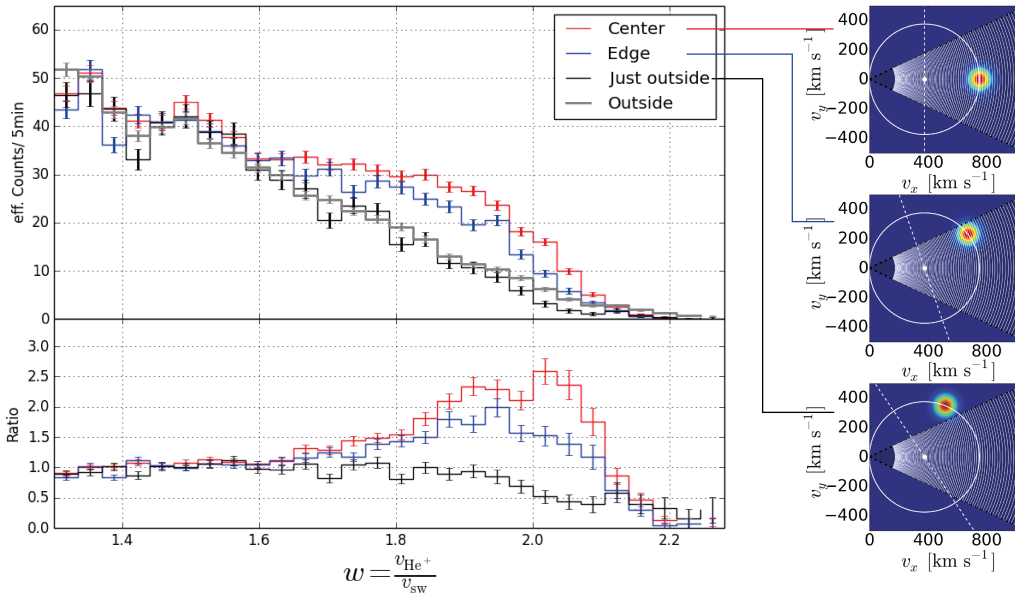


FIGURE 1. In the top panel the w -histograms corrected for detection efficiencies and observation time are displayed that were created for the four magnetic field configurations given in Tab. 1. The lower panel displays the ratio of the histograms "Center", "Edge", and "Just outside" with the "Outside" histogram to make the torus distributed He^+ ions visible. The three plots on the right-hand side show a 2D cut through velocity space, the v_x - v_y plane, which correspond to the "Center", "Edge", and "Just outside" case. The dashed white line shows the magnetic field orientation and the expected torus distribution (with arbitrary width) indicated with a color code. The shaded triangle corresponds to CTOF's aperture.

ACKNOWLEDGMENTS

We gratefully acknowledge use of Proton Monitor data that has been provided by the SOHO archive. This work was supported by the German Space Agency (DLR) under grants number 50 OC 1103 and 50 OC 1501 and by the University of Kiel. Rfws thanks ISSI and the ISSI team "Exploration of the inner Heliosphere - what we have learned from Helios and what we want to study with Solar Orbiter" for helpful discussions.

REFERENCES

- [1] E. Möbius, D. Hovestadt, B. Klecker, M. Scholer, and G. Gloeckler, *Nature* **318**, 426–429 (1985).
- [2] R. Kallenbach, J. Geiss, G. Gloeckler, and R. Von Steiger, *Astrophysics and Space Science* **274**, 97–114 (2000).
- [3] C. Drews, L. Berger, A. Taut, T. Pelekis, and R. Wimmer-Schweingruber, *Astronomy & Astrophysics* **575**, p. A97 (2015).
- [4] E. Möbius, D. Rucinski, M. Lee, and P. Isenberg, *Journal of Geophysical Research: Space Physics* (1978–2012) **103**, 257–265 (1998).
- [5] M. Oka, T. Terasawa, H. Noda, Y. Saito, and T. Mukai, *Geophysical research letters* **29**, 54–1 (2002).
- [6] C. Drews, L. Berger, R. F. Wimmer-Schweingruber, and A. B. Galvin, *Geophysical Research Letters* **40**, 1468–1473 (2013).
- [7] D. Hovestadt, M. Hilchenbach, A. Bürgi, B. Klecker, P. Laeverenz, M. Scholer, H. Grünwaldt, W. Axford, S. Livi, E. Marsch, *et al.*, in *The SOHO Mission* (Springer, 1995), pp. 441–481.
- [8] C. Drews, L. Berger, R. F. Wimmer-Schweingruber, P. Bochsler, A. B. Galvin, B. Klecker, and E. Möbius, *Journal of Geophysical Research: Space Physics* (1978–2012) **117** (2012).
- [9] A. Taut, L. Berger, C. Drews, and R. Wimmer-Schweingruber, *Astronomy & Astrophysics* **576**, p. A55 (2015).
- [10] R. Lepping, M. Acuña, L. Burlaga, W. Farrell, J. Slavin, K. Schatten, F. Mariani, N. Ness, F. Neubauer, Y. Whang, *et al.*, *Space Science Reviews* **71**, 207–229 (1995).
- [11] L. Saul, E. Möbius, P. Isenberg, and P. Bochsler, *The Astrophysical Journal* **655**, p. 672 (2007).
- [12] D. Weimer, D. Ober, N. Maynard, W. Burke, M. Collier, D. McComas, N. Ness, and C. Smith, *Journal of Geophysical Research: Space Physics* (1978–2012) **107**, SMP-29 (2002).
- [13] J. A. le Roux, G. P. Zank, and W. H. Matthaeus, *Journal of Geophysical Research: Space Physics* (1978–2012) **107**, SSH-9 (2002).
- [14] N. Schwadron, *Journal of Geophysical Research: Space Physics* (1978–2012) **103**, 20643–20649 (1998).

THE INTERSTELLAR FLOW LONGITUDE DERIVED FROM THE PICKUP ION CUTOFF

The parameters of the partially ionized [LISM](#) play a crucial role in the understanding of the heliosphere and, in particular, its boundaries. The relative velocity vector and the magnetic field embedded in the [LISM](#) determine the external dynamic and magnetic pressure onto the heliosphere. In principle, this interplay creates the shape of the heliosphere ([Parker, 1961](#)). Furthermore, the existence of a bow shock inside the [LISM](#) is still under debate (e.g. [Ratkiewicz and Kotlarz \(2016\)](#)). The crucial question for this is, if the interstellar plasma flow is supersonic with respect to the relative motion of heliosphere and [LISM](#). This depends of course on the relative speed, $v_{\text{ISN},\infty}$, and the magnetosonic speed within the [LISM](#), which depends on density, temperature, and magnetic field strength.

As indicated above, the velocity vector of the relative motion between [LISM](#) and heliosphere is a key parameter for the understanding of the boundaries of the heliosphere. This velocity vector also corresponds to the flow vector of interstellar neutrals into the heliosphere, $\vec{v}_{\text{ISN},\infty}$. The direction of this vector can be measured by backscattered solar UV light on hydrogen ([Bertaux and Blamont, 1971](#)) or helium atoms ([Weller and Meier, 1974](#)); the speed and longitude can be determined from interstellar [PUI](#) measurements ([Möbius et al., 1995](#); [Gloeckler et al., 2004](#)), and the whole vector can be determined utilizing direct neutral particle measurements ([Witte \(2004\)](#); [Wood et al. \(2015\)](#); [McComas et al. \(2015\)](#); [Schwadron et al. \(2015\)](#), etc.). An overview of the measurement of the [LISM](#) parameters with various techniques until 2004 may be found in [Möbius et al. \(2004\)](#).

The most recent results from [IBEX](#) are based on count rate measurements of interstellar neutrals as a function of direction. This involves the problem that the various [LISM](#) parameters one can determine from the hyperbolic trajectory equation (flow longitude λ_{flow} , latitude β_{flow} , speed $v_{\text{isn},\infty}$, and temperature T_{LISM}) are coupled and their corresponding uncertainties leave a comparatively large 4D parameter tube ([Schwadron et al., 2015](#)). One can easily explain this coupling on the example of the flow direction and speed: Due to the gravitational bending of the neutral particle trajectories, one has to assume a certain particle speed to derive the direction from which the particles originally came from. Vice versa, one has to know the precise flow direction to derive the particle speed from the bending of the trajectory. This example of the coupling of uncertainties (with the flow longitude) is displayed in the top panel of Fig. 17. In the bottom panel the coupling of interstellar flow longitude and [LISM](#) temperature is displayed.

It is also possible to determine λ_{flow} with the help of [PUIs](#). The main advantage of the measurement of charged particles instead of neutral particles is that a precise measurement of the charged particle's speed is possible. Therefore, λ_{flow} can be determined by an independent approach. An independent and precise measurement of the interstellar flow longitude would then also restrict this 4D parameter

tube, which means that more precise parameters of the flow latitude, speed, and temperature would be obtained. The first approach to derive the interstellar flow longitude from PUI measurements has been related to the PUI flux increase caused by the focusing cone (Gloeckler et al., 2004). As the neutral particle focusing cone is supposed to be aligned with the interstellar neutral flow and the PUI production rate is directly coupled to the neutral seed density, the interstellar PUI flux increase inside the focusing cone provides information about the flow direction. In Drews et al. (2012), also the PUI crescent has been added to this kind of study. However, as was shown by simulations presented in Chalov and Fahr (1999) and Quinn et al. (2016), this method suffers from a systematic error. Due to the anisotropy of the PUI VDF, the ions are exerted to a transport process along the mean IMF following the Parker spiral. This systematic effect shifts the PUI focusing cone to larger ecliptic longitudes compared to the neutral particle focusing cone.

In Möbius et al. (2015), another method to derive the interstellar flow longitude λ_{flow} from PUI measurements has been proposed, that is expected to minimize such transport effects. This method is based on the fact that the radial injection speed of

PUIs manifests itself in the VDF. The location of the so-called cutoff of the PUI VDF, which is a comparatively sharp decrease of count rates, varies as a function of injection speed, which was already observed by Möbius et al. (1999). By quantifying the cutoff, one obtains a proxy for the injection speed, which is related to the neutral particle speed. As PUIs measured around the cutoff did not have much time to cool, one can assume that these freshly injected ions are substantially less affected by transport processes. As the neutral speed follows a symmetric pattern at a given distance from the Sun, this symmetry is preserved in the PUI VDF, which can be utilized to derive the symmetry axis. The symmetry axis corresponds to the neutral flow longitude.

In this publication, we revisit the method proposed by Möbius et al. (2015) to determine the interstellar flow longitude from measurements of the PUI VDF. Thus, we contribute to Question 3: *How can we utilize the PUI VDF to find the interstellar neutral flow longitude?* This is inevitably connected to Question 2: *What is the 3D VDF of PUIs at 1 AU and what are the implication for the stability of a torus VDF within the dynamic solar wind?* As we are aiming to utilize the PUI VDF to determine λ_{flow} , a good understanding of the VDF itself is necessary for a precision measurement of this parameter.

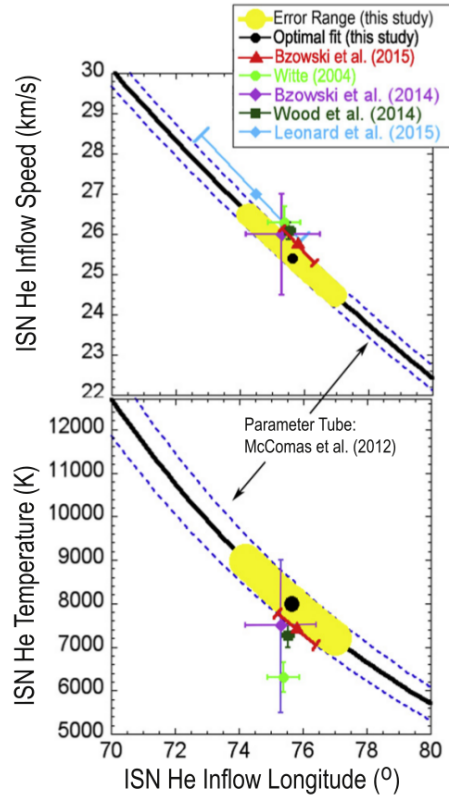


Figure 17: IBEX results for the flow speed, $v_{\text{ISN},\infty}$, and temperature, T_{ISM} , as a function of flow longitude, λ_{flow} , from various studies. The plot is taken from Schwadron et al. (2015). The uncertainties of the parameters (including flow latitude β_{flow}) are coupled and leave a 4D parameter tube.

5.1 BRIEF SUMMARY OF THE PUBLICATION

After a short overview about the context of this investigation and former measurements of λ_{flow} , the motivation of the paper is outlined. The method developed by Möbius et al. (2015) is proposed to be improved and as a consequence of the improvements further systematic errors connected to this method can be identified. The utilized STA/PLASTIC data set is introduced, followed by an extensive description of the physical principles that the method developed by Möbius et al. (2015) is based on.

The first improvement of the λ_{flow} determination is a filter for acceleration sites, that systematically shift the determined cutoff speeds to higher values. For this, we developed a criterion based on the He²⁺ VDF simultaneously measured by PLASTIC. The general idea is, to exclude time periods where an acceleration signature is measured in the He²⁺ VDF as we expect the He⁺ ions to have undergone acceleration in these time periods as well. Then, the frame of reference in which the PUI VDF is considered is discussed. It is outlined that there is an underlying systematic error connected to the determination of the cutoff speed in terms of w'_{sw} , but this error can be minimized by utilizing the newly introduced quantity V_r instead. Additional techniques to determine the cutoff speed are introduced and afterwards the determination of λ_{flow} from the cutoff speeds is revised. It is proposed to use a model as fit function, which incorporates the non-circular orbit of STA, which introduces an asymmetry in the cutoff speeds. Another improvement is the concept of estimating the resulting error from this approach, that is calculated utilizing Bootstrap Monte-Carlo techniques.

In the presentation of the results, the result of the different cutoff speed and λ_{flow} determination methods are compared to each other. Furthermore, two different data sets are compared. The methods have been applied on the one hand to a data set, where acceleration sites have been excluded with the introduced condition, and on the other hand to a data set unfiltered for these time periods. The lower uncertainties within the results of the data set filtered for local acceleration justify our approach. Furthermore, we show that larger mirror-correlation coefficients compared to the ones presented in the original paper by Möbius et al. (2015) are obtained after the improvement of the method. This implies an enhanced level of symmetry of the determined cutoff speeds which should result in a more precise determination of λ_{flow} . However, we obtain larger errors for λ_{flow} than given in the original paper by Möbius et al. (2015). This strongly indicates that the error of the method given in Möbius et al. (2015) is highly underestimated.

With the help of the improved method, the impact of the selection in IMF orientation is studied. An unexpected, clear dependence of the λ_{flow} result as a function of IMF orientation is found. This means that the mix of IMF orientations contained in the utilized data set introduces a systematic error in the λ_{flow} result. It is surmised that longitudinal transport is again involved in the creation of this effect. Finally, the publication concludes arguing that none of the presented λ_{flow} results should be taken as the real inflow direction as the newly found systematic error has to be investigated in more detail.

5.2 PUBLICATION

The following article is reproduced from Taut et al. (2018) with permission from Astronomy & Astrophysics, ©ESO.

Challenges in the determination of the interstellar flow longitude from the pickup ion cutoff

A. Taut, L. Berger, C. Drews, E. Möbius, V. Heidrich-Meisner, D. Keilbach, M. A. Lee and R. F. Wimmer-Schweingruber, *Astronomy & Astrophysics*, accepted: 20 November 2017, DOI: 10.1051/0004-6361/201731796

Own contribution: 70%

Challenges in the determination of the interstellar flow longitude from the pickup ion cutoff

A. Taut¹, L. Berger¹, E. Möbius², C. Drews¹, V. Heidrich-Meisner¹, D. Keilbach¹, M. A. Lee², and R. F. Wimmer-Schweingruber¹

¹ Institut für Experimentelle und Angewandte Physik, Christian-Albrechts-Universität zu Kiel, Germany
e-mail: taut@physik.uni-kiel.de

² Space Science Center & Department of Physics, University of New Hampshire, Durham, NH, USA

December 7, 2017

ABSTRACT

Context. The interstellar flow longitude corresponds to the Sun's direction of movement relative to the local interstellar medium. Thus, it constitutes a fundamental parameter for our understanding of the heliosphere and, in particular, its interaction with its surroundings, which is currently investigated by the Interstellar Boundary EXplorer (IBEX). One possibility to derive this parameter is based on pickup ions that are former neutral ions that have been ionized in the inner heliosphere. The neutrals enter the heliosphere as an interstellar wind from the direction of the Sun's movement against the partially ionized interstellar medium. Pickup ions carry information about the spatial variation of their neutral parent population (density and flow vector field) in their velocity distribution function. From the symmetry of the longitudinal flow velocity distribution, the interstellar flow longitude can be derived.

Aims. The aim of this paper is to identify and eliminate systematic errors that are connected to this approach of measuring the interstellar flow longitude; we want to minimize any systematic influences on the result of this analysis and give a reasonable estimate for the uncertainty.

Methods. We use He⁺ data measured by the PLAsma and SupraThermal Ion Composition (PLASTIC) sensor on the Solar TErrestrial RElations Observatory Ahead (STEREO A) spacecraft. We analyze a recent approach, identify sources of systematic errors, and propose solutions to eliminate them. Furthermore, a method is introduced to estimate the error associated with this approach. Additionally, we investigate how the selection of interplanetary magnetic field angles, which is closely connected to the pickup ion velocity distribution function, affects the result for the interstellar flow longitude.

Results. We find that the revised analysis used to address part of the expected systematic effects obtains significantly different results than presented in the previous study. In particular, the derived uncertainties are considerably larger. Furthermore, an unexpected systematic trend of the resulting interstellar flow longitude with the selection of interplanetary magnetic field orientation is uncovered.

Key words. Sun: heliosphere – Sun: fundamental parameters – ISM: general – solar wind

1. Context

The heliosphere is a plasma bubble that is carved out of the partially ionized local interstellar medium (LISM) by the solar wind. Recently, our understanding of the boundaries of the heliosphere and its interaction with the LISM has been expanded by the unexpected results of the Interstellar Boundary EXplorer (IBEX) and the in situ observations by the Voyager spacecraft (Stone et al. 2005). Among the findings is the IBEX ribbon (McComas et al. 2009), which provides insight into the interstellar magnetic field. Another key component of the interaction is the interstellar flow vector, \mathbf{v}_{LISM} , which denotes the relative motion between the Sun and the LISM. Therefore, the interstellar flow vector has been the objective of investigations for years (Axford 1972). First, remote measurements of neutral hydrogen (Bertaux & Blamont 1971) and helium (Weller & Meier 1974) were performed using backscattered solar UV observations. Later on, in situ measurements using PickUp Ions (PUIs) (Möbius et al. 1995) and direct neutral particle observations (Witte 2004) complemented the previous studies. A more extensive summary of the history of the investigation of the interstellar flow can be found in Möbius et al. (2004).

Due to the relative motion between the Sun and the LISM of

$\sim 26 \text{ km s}^{-1}$ (Wood et al. 2015), neutral particles enter the heliosphere as an interstellar wind from a defined direction. Since 2008, these neutrals are measured by IBEX amongst others, from which one can derive \mathbf{v}_{LISM} and the temperature of the interstellar neutral flow, T_{ISN} , through the hyperbolic trajectory equation (see Bzowski et al. (2012), Möbius et al. (2012)). The inflow vector can also be expressed by the inflow longitude, λ_{flow} ; latitude, β_{flow} ; and speed, V_{ISN} . However, these parameters are coupled. They can be expressed as a function of the interstellar neutral flow longitude and the range of allowable parameters along the 4D parameter tube is relatively large (see Schwadron et al. (2015)). Therefore, an independent measurement of the interstellar flow longitude would help to constrain this parameter tube.

The interstellar neutral flow forms a characteristic structure close to the Sun that is symmetric about the flow direction. Not only its density profile, but also its velocity pattern follows this symmetry, which is obvious along a circular orbit around the Sun. From these features the longitudinal direction of the flow vector can be derived using interstellar PUI measurements. Interstellar PUIs are created from interstellar wind neutrals by ionization processes, such as photoionization by EUV radiation, charge-exchange with solar wind protons, and electron impact. PickUp

Ions were already predicted in the 1970s by Fahr (1971) and subsequently confirmed by observations of the AMPTE spacecraft (Möbius et al. 1985). One can easily identify PUIs by their almost exclusive single-charge state and their highly suprathermal velocity distribution function (VDF), which is a consequence of the pickup process. Once ionized, PUIs are exposed to the electromagnetic forces exerted by the solar wind and the frozen-in magnetic field, and transported outward.

As the interstellar wind is gravitationally focused downwind of the Sun, a region of enhanced neutral density evolves, called the focusing cone. Of course, the condition for this structure to form is that enough neutrals reach the downwind side without being ionized. Hence, the focusing cone is only observed for elements with a high first ionization potential, such as helium or neon (Drews et al. 2010). On the upwind side of the Sun, called the crescent, forms for elements with a low first ionization potential like oxygen (Drews et al. 2012). At ecliptic longitudes, λ , which corresponds to the interstellar upwind direction, the neutrals have a smaller pathlength to reach a distance of 1 AU from the Sun. Thus, these neutrals are less affected by ionization processes, which increases the number of particles that reach this distance.

These two regions are aligned with the interstellar flow longitude, λ_{flow} . The PUI production rate is directly coupled to the neutral particle density and thus largely reproduces the focusing cone and the crescent. Furthermore, the crescent signature is more pronounced in the observed PUI flux due to the radial velocity variation that follows the density profile (Sokół et al. 2016). In this way, the crescent also becomes visible for species with low ionization rates, such as helium. Hence, PUI measurements can also be utilized to determine λ_{flow} , as was performed in Drews et al. (2012). Although a careful error estimation was performed, it is likely that these results are affected by systematic errors. In contrast to neutrals, PUIs are affected by transport effects that act preferably along the mean interplanetary magnetic field (IMF), which follows the Parker spiral (Chalov 2014; Quinn et al. 2016).

Another method for using PUIs as a diagnostic tool to derive the interstellar flow longitude, λ_{flow} , was recently proposed by Möbius et al. (2015). As shown in Möbius et al. (1999) the injection speed of PUIs into the solar wind depends on ecliptic longitude because of the longitude-dependant relative motion of the neutral interstellar wind particles and the radially outward streaming solar wind. This injection speed can be determined from the PUI VDF by utilizing what is known as the cutoff feature. As this method is based on the evaluation of freshly injected ions, it is expected to be less sensitive to transport effects and therefore substantially less affected by the possibility of a strong systematic error.

2. Motivation and goals

In this paper we revisit the method presented as a proof-of-concept study by Möbius et al. (2015) using He^+ PUI data from the PLASma and SupraThermal Ion Composition instrument (PLASTIC, Galvin et al. (2008)) on board the Solar TErestrial RElations Observatory Ahead spacecraft (STEREO A). We extend this method by analyzing its weaknesses and proposing ways to circumvent these disadvantages. Furthermore, a new method to obtain a reasonable error estimation is applied. Using the improved method to derive the interstellar flow longitude, we investigate further systematic effects that may influence the interstellar flow longitude results from the He^+ PUI cutoff.

First, we give a short introduction into the STEREO A/PLASTIC

He^+ data. Second, we provide an overview of the PUI physics that enables the determination of the interstellar flow longitude from PUI VDFs, which was performed in Möbius et al. (2015). We summarize the individual steps of the revisited analysis and describe the improvements implemented in each step.

As in Möbius et al. (2015) we perform the PUI analysis in the solar wind frame. This has the advantage that the injection speed of PUIs is solely a function of the solar wind speed, $|\mathbf{v}_{\text{sw}}| = v_{\text{sw}}$, and the local interstellar neutral flow velocity, \mathbf{V}_n . In Fig. 1 this is illustrated for the simplified case of PUIs that are created from neutrals that are at rest. Due to their gyration about the IMF, the PUI velocities lie on a shell that has the radius of the solar wind speed and is centered around the solar wind velocity. Accordingly, all PUIs of the torus VDF move at solar wind speed in the solar wind frame in this case.

Möbius et al. (2015) perform their analysis of the PUI distribution in terms of the normalized PUI speed $w'_{\text{He}^+} = \frac{v'_{\text{He}^+}}{v_{\text{sw}}}$, where $v'_{\text{He}^+} = |\mathbf{v}_{\text{He}^+} - \mathbf{v}_{\text{sw}}|$ is the PUI speed in the solar wind frame. In contrast, we transform the measured PUI speeds into another data product, V_r , which eliminates the influence of the ambient solar wind speed on the cutoff speed determination. A more detailed discussion of V_r is provided in Sect. 4.4.1. Furthermore, we propose improved methods to derive the cutoff speed and we present an approach to exclude acceleration sites from the data that may have an influence on the cutoff speed measurements. The final improvement of the original method that we introduce here is an error estimation that is based on a bootstrap Monte Carlo approach, similar to that utilized in Drews et al. (2012). After these improvements, further systematic influences of external parameters on the result for the interstellar flow longitude from the PUI cutoff are investigated. As the PUI VDF and therefore the longitudinal transport of these ions, which should be minimized by concentrating on the PUI cutoff, is linked to the ambient IMF configuration, we test how the selection of IMF directions still affects the results of the analysis.

3. Data acquisition

PLASTIC is a time-of-flight mass spectrometer that measures energy-per-charge, time-of-flight, and residual energy from which the mass, charge, and energy of an incident ion can be calculated. Using this information one can extract the He^+ data of PLASTIC's solar wind section, as in Drews et al. (2010, 2012). Once an ion is identified, one can calculate the ion's speed in the spacecraft frame of reference from the energy-per-charge information, which makes it possible to derive the VDF of an ion species.

One great advantage of PLASTIC compared to other time-of-flight mass spectrometers (e.g., CTOF on SOHO or SWICS on ACE) is its position-sensitive detection system. The latitudinal angle of incidence is measured in the range of -20° to $+20^\circ$ in 32 steps with a deflection system, while the measurement of the azimuthal angle in the range of -22.5° to $+22.5^\circ$ in 32 steps is realized by evaluating the output of a resistive anode. This means that the velocity vector of the measured ion in the spacecraft frame, in this case \mathbf{v}_{He^+} , can be fully reconstructed. This is true not only for PUIs, but also for the solar wind proton measurement, which yields the solar wind bulk velocity, \mathbf{v}_{sw} , as a 3D vector. Thus, a transformation of the PUI velocity in the spacecraft frame, \mathbf{v}_{He^+} , into the solar wind frame, $\mathbf{v}'_{\text{He}^+}$, is possible.

Furthermore, we use the 1 min resolution IMF data provided by the IMPACT instrument suite (Acuña et al. 2008), a time

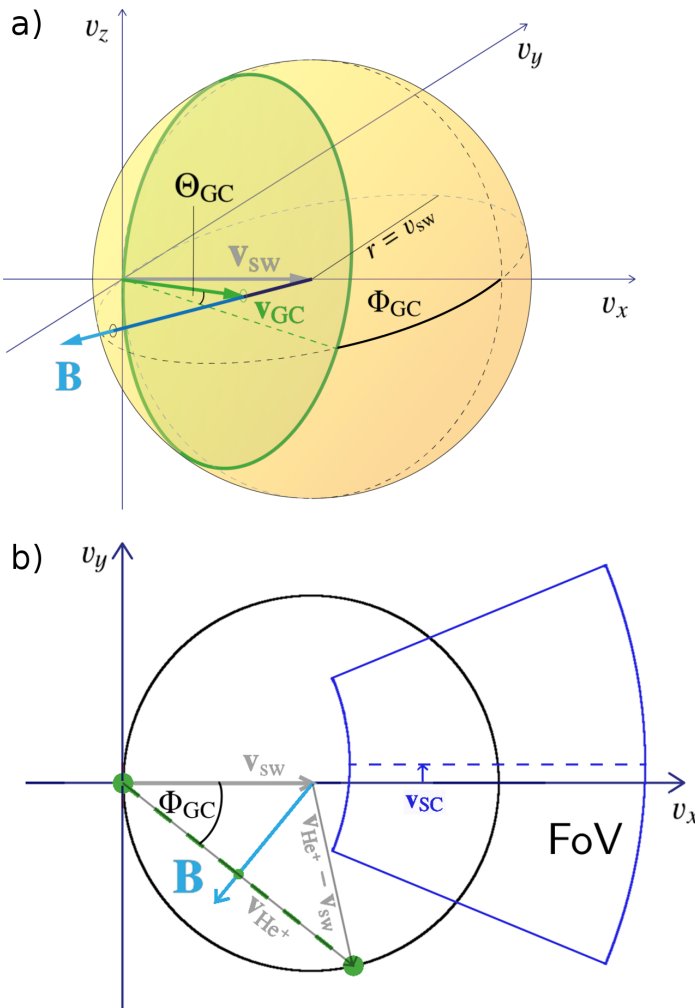


Fig. 1. Illustration of the ideal torus VDF of freshly injected PUIs.

a) 3D illustration, where v_x corresponds to the radial direction with respect to the Sun. PUIs at rest are injected into the solar wind plasma with a torus VDF that lies on a shell around the solar wind velocity. The radius of the shell equals the solar wind speed. The green line shows the velocity space trajectory of the PUIs around \mathbf{B} . The guiding center velocity of the torus, \mathbf{v}_{GC} , is shown with the green vector. Furthermore, the latitudinal angle, Θ_{GC} , of the guiding center velocity is illustrated. b) 2D cut through the v_x - v_y plane of the configuration shown in a). For the intersection of the torus with the v_x - v_y plane, the velocity vectors in the spacecraft and solar wind frame of reference are shown. The area marked by the blue solid lines depicts PLASTIC's coverage in velocity space. It is not symmetrical about v_x , because of STEREO A's tangential eigen-velocity of 30 km s^{-1} . Freshly injected PUIs would obviously not be observed by PLASTIC under this IMF orientation. The angle Φ_{GC} corresponds to the azimuthal angle of the guiding center velocity.

resolution more than adequate for the PLASTIC data sets with a sensor cycle time of 5 minutes.

4. Analysis method

4.1. Physical motivation

In Fig. 2 an overview of the physical motivation of the approach to obtain the interstellar flow longitude, as introduced in Möbius et al. (2015), is given. Due to the Sun's gravitation, the interstellar neutral flow forms a characteristic structure around the Sun, which is symmetric about the interstellar flow direction

(Fig. 2 a). This symmetry is also found in the radial speed of the neutrals considering a fixed distance from the Sun (Fig. 2 b). If these neutrals become ionized, their injection speed into the solar wind plasma depends on the relative motion of the parent neutral with respect to the solar wind, which is shown in Fig. 2 c for the crescent ($\lambda \approx 255^\circ$), the focusing cone ($\lambda \approx 75^\circ$), and two intermediate locations ($\lambda \approx 165^\circ$ and $\lambda \approx 345^\circ$), illustrated with three different choices of the IMF orientation that keep the initial torus within the PLASTIC field of view(FoV). Consequently, the PUI VDF carries an imprint of the neutral's radial speed upon PUI injection, which manifests itself in the so-called PUI cutoff, which is discussed in the following section. We utilize this feature to determine the interstellar flow longitude.

4.2. Pickup ion cutoff

Due to their gyration about the IMF, PUIs are injected into the solar wind plasma with an anisotropic VDF that has the shape of a torus in velocity space. While traveling outward with the solar wind, the initial anisotropic VDF is gradually transformed into an isotropic VDF by pitch-angle scattering, which until recently was expected to be a rapid process. However, independent observations made by different spacecraft showed that in particular the He^+ VDF remains anisotropic for much longer than previously assumed (Oka et al. 2002; Drews et al. 2015; Taut et al. 2016).

For PUIs that are generated from neutrals at rest, this initial torus lies on a shell that is centered around the solar wind velocity and has a radius equal to the solar wind speed (Fig. 1). Consequently, these PUIs always move with solar wind speed in the solar wind frame of reference independent of the IMF orientation. For non-resting neutrals the injection speed, and therefore the radius of the shell, depends predominantly on the neutral's radial speed, as is pointed out in the previous section. Thus, this speed is directly related to the ecliptic longitude, where the ion is injected. In Fig. 2 c three examples are shown corresponding to different ecliptic longitudes and IMF orientations.

Following the initial theory of PUI VDFs by Vasylunas & Siscoe (1976), which implied a rapid isotropization by pitch-angle scattering and assumed no energy transfer between the solar wind and PUIs, no PUIs above the injection speed are expected to be observed. Hence, the so-called PUI cutoff would be a sharp edge of the VDF and it would be trivial to derive the injection speed. Instead, all PUI observations show a smooth decrease in count rate rather than a sharp edge. In the following, we call this decrease the PUI cutoff of the VDF.

There are two possible ways to explain the observation of PUIs above the injection speed. First, the most obvious explanation is that acceleration processes must act on the PUI VDF. Acceleration can occur locally due to compression regions or shocks, which is discussed in more detail in Sec. 4.3. Furthermore, even in the quiet solar wind a ubiquitous population of accelerated particles can be observed (see Fisk & Gloeckler (2012)), which indicates that acceleration may continuously act on the PUI VDF.

Second, as can be seen from Fig. 1, the guiding center velocity of PUIs in the spacecraft frame is not necessarily equal to the solar wind velocity, especially at IMF orientations not at 90° to the solar wind. Hence, PUIs may be transported from the solar wind parcel where they were created at a given solar wind speed into another solar wind parcel with, for example, a slightly lower speed. In the solar wind frame of reference, these ions then appear to have a speed above the local injection speed because the PUI speed is always considered with respect to the

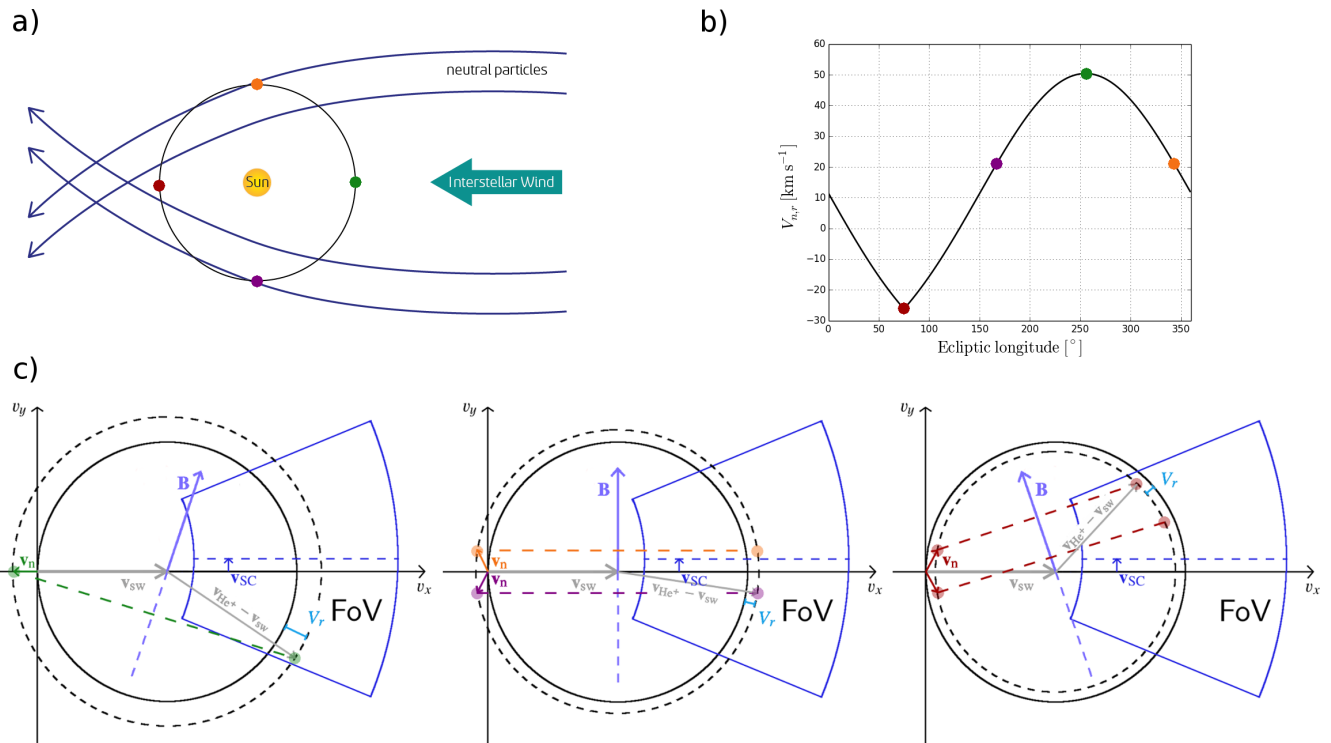


Fig. 2. a) Interstellar neutral flow in the ecliptic plane. Four sample trajectories are shown and four locations are marked by colored dots: green corresponds to the crescent ($\lambda \approx 255^\circ$), dark red corresponds to the focusing cone ($\lambda \approx 75^\circ$), and the orange and purple points correspond to ecliptic longitudes in between ($\lambda \approx 165^\circ$ and $\lambda \approx 345^\circ$). b) Radial speed of the interstellar neutrals as a function of ecliptic longitude calculated from Eq. 5 with $\lambda_{flow} = 75^\circ$ and $v_{ISN\infty} = 0.88$. The colored dots correspond to the ecliptic longitudes introduced in a). c) 2D velocity space illustrations in the v_x - v_y plane for the PUI injection (Fig. 1). The velocity of the neutrals at each ecliptic longitude is shown as a colored vector. The bold circle illustrates the shell with radius v_{sw} , while the dashed circle depicts the shell on which the PUI torus lies that results from the non-zero radial speed of the parent neutral. For illustration purposes, the IMF orientation is chosen to lie within the ecliptic plane. The colored dashed lines illustrate the orientation of the torus VDF, the colored dots mark the points where the torus intersects with the v_x - v_y plane. *left:* PUI injection in the crescent at an IMF orientation corresponding to $\Phi_{GC} \approx -15^\circ$. *middle:* PUI injection between the crescent and focusing cone at an IMF orientation corresponding to $\Phi_{GC} \approx 0^\circ$. *right:* PUI injection in the focusing cone at an IMF orientation corresponding to $\Phi_{GC} \approx +15^\circ$.

solar wind speed (see Sec. 4.4.1).

Therefore, the measured PUI cutoff VDF is modulated by multiple processes, which makes it impossible to derive the precise injection speed from a measured PUI VDF. Fortunately, a relative cutoff speed shift as a function of ecliptic longitude is sufficient to find the interstellar flow longitude as the symmetry is still preserved for the relative speeds. For example, we can choose a characteristic point on the cutoff VDF which we define as the cutoff speed. This point must not necessarily correspond to the injection speed, but the offset of the injection speed to this characteristic point can be assumed to be constant, if the shape of the PUI cutoff VDF is constant at all ecliptic longitudes.

In any case, all processes modulating the PUI cutoff are stochastically distributed and, in particular, are not expected to show any dependence on ecliptic longitude. This means that when considering long-term data, these stochastic fluctuations of the PUI cutoff are expected to average out, resulting in a comparable shape of the cutoff for all ecliptic longitudes. If we assume that the PUI cutoff shape is approximately equal at all ecliptic longitudes, we can derive methods to find the relative cutoff speed, which are described in Sec. 4.4.2.

However, to justify this assumption we need to ensure that PLASTIC actually measures freshly injected ions. If the initial torus of freshly injected PUIs is not within the FoV of PLASTIC, only PUIs that already have undergone a scattering process are measured, which may completely alter the shape of the cutoff. In addition, it is very important for the determination of

the interstellar flow longitude from the PUI cutoff that freshly injected PUIs are significantly less affected by possible PUI transport processes along the mean IMF.

To test whether the initial torus VDF of freshly injected PUIs is inside PLASTIC's aperture or not, the guiding center velocity, \mathbf{v}_{GC} , of an ideal torus in the spacecraft frame is considered. We define the ideal torus as the theoretical velocity-space trajectory that an injected PUI with initial speed $V_n = 0$ would follow under a perfectly stable IMF configuration. Former PUI studies (e.g., Drews et al. (2015, 2016)) and also Möbius et al. (2015) restrict the IMF data to orientations that lie $\pm 20^\circ$ within the ecliptic plane. Then it solely depends on the azimuthal angle of the IMF whether an ideal torus falls into PLASTIC's FoV or not. However, a huge amount of data is dismissed by this restriction, while there are IMF orientations possible, where the torus falls into the FoV without lying within the ecliptic plane. The guiding center velocity of the ideal torus in the spacecraft frame, \mathbf{v}_{GC} , can be derived by simple geometric arguments:

$$\mathbf{v}_{GC} = \mathbf{v}_{sw} - \frac{B_x v_{sw}}{|\mathbf{B}|^2} \mathbf{B} \quad (1)$$

$$\Phi_{GC} = \arctan 2(v_{GC,y}, v_{GC,x}) \star \quad (2)$$

$$\Theta_{GC} = \arcsin \left(\frac{v_{GC,z}}{|\mathbf{v}_{GC}|} \right) \quad (3)$$

The azimuthal angle, Φ_{GC} , and the latitudinal angle, Θ_{GC} , correspond to the spherical coordinates of the vector. If \mathbf{v}_{GC} is within PLASTIC's angular coverage, then also a slice of the gyrotrropic torus VDF falls into its FoV. Thus, an ideal torus falls into PLASTIC's aperture if $-22.5^\circ \leq \Phi_{GC} \leq 22.5^\circ$ and $-20^\circ \leq \Theta_{GC} \leq 20^\circ$ neglecting STEREO A's eigen-velocity of $v_{SC} \approx 30 \text{ km s}^{-1}$ in the longitudinal direction. Only if \mathbf{v}_{GC} fulfills both criteria are torus PUIs observed by PLASTIC. Due to v_{SC} the symmetry line of PLASTIC's velocity-space coverage is shifted with respect to the radial direction. This has the effect that the angular range of Φ_{GC} , where an ideal torus would be observed, is shifted by approximately $+3^\circ$ for very low solar wind speeds ($v_{sw} \approx 250 \text{ km s}^{-1}$). In Fig. 1 an example is shown for an arbitrary IMF orientation. In this example, the angular coordinates of \mathbf{v}_{GC} are $\Theta_{GC} \approx +5^\circ$ and $\Phi_{GC} \approx -40^\circ$, which means that no torus PUIs are observed by PLASTIC under this IMF orientation.

4.3. Acceleration sites

As already indicated in Sec. 2, the observation of He^+ ions above the injection speed is evidence that acceleration processes may act on the He^+ VDF. Especially, shocks or compression regions like Stream Interaction Regions (SIRs) with a high level of turbulence (cf. Gloeckler et al. (1994), Schwadron et al. (1996)) can efficiently accelerate PUIs above their injection speed. In turn, this means that the He^+ cutoff shape and location may be significantly altered by the increased abundance of accelerated PUIs, which would contradict the assumption that the PUI cutoff VDF is comparable at all ecliptic longitudes. More precisely, this may lead to a systematically higher cutoff speed at ecliptic longitudes where local acceleration sites are included in the data. These changes in the PUI cutoff will very likely bias the determination of the interstellar flow longitude, λ_{flow} .

In order to minimize the effect of time periods with a strong local acceleration on the cutoff measurements, we attempt to eliminate these occurrences. As a criterion for this task, we consider He^{2+} distributions also measured by PLASTIC. He^{2+} is of solar origin and thus does not vary systematically with ecliptic longitude. Also, its counting statistics are sufficient to yield a statistically significant representation of the VDF on a 5 min basis. It is reasonable to assume that acceleration processes in compressions act similarly on both ion species, He^+ and He^{2+} (e.g., Gloeckler (1999), Chotoo et al. (2000)), or that at least signatures of acceleration processes that act on He^+ are visible in the He^{2+} VDF. Then, we can identify and eliminate time periods when the He^{2+} VDF is affected by acceleration processes.

Similar to the He^+ distributions, those of He^{2+} are derived from the raw PLASTIC pulse-height-analysis by the expected time-of-flight and residual energy signal at a given energy-per-charge step. For every He^{2+} count its speed relative to the solar wind speed, $w_{\text{He}^{2+}} = \frac{v_{\text{He}^{2+}}}{v_{sw}}$, in the spacecraft frame is calculated. The solar wind section of PLASTIC has another feature that we utilize here. The energy-per-charge values are stepped through from high to low values. If the particle flux exceeds a certain limit when the energy steps approach the He^{2+} bulk flow energy, the sensor switches to the so-called small channel, which reduces its geometric factor. Because the channel switch occurs at a fixed count rate we can treat this threshold as a reference flux. In the following, we use the normalized speed of He^{2+} ions $w_{\text{He}^{2+},10\%}$ where the He^{2+} rate exceeds 10% of the channel switch thresh-

old value as a condition for effective acceleration of He^{2+} ions and thus by inference also of He^+ PUIs.

We motivate the choice of our condition for interplanetary acceleration with the display of the He^+ and He^{2+} VDFs over the course of an SIR in Fig. 3. The spectra are taken during four time intervals, which are marked in blue, gray, cyan, and red. In the solar wind speed and density data one can clearly identify the SIR at approximately DoY 127 - 129 by the strong increase in density, which is subsequently followed by a sudden drop and then an increase in solar wind speed (see Jian et al. (2006)). The blue and red periods correspond to comparatively undisturbed solar wind before and after the SIR, respectively. The time period marked in gray corresponds to turbulent wind right after the spacecraft passed the stream interface, which can be identified by the sudden drop in proton density. The time period marked in cyan already has a slight negative gradient in solar wind speed. Nevertheless, the proton density (and the He^{2+} spectra) suggest that compressed fast solar wind is observed.

In the lower left panel the He^+ spectra measured in the four time periods are displayed. In the quiet solar wind, a sharp cutoff is observed that matches the expected injection speed of $V_r \approx 50 \text{ km s}^{-1}$ as the time period can be assigned to a position of STEREO A close to the interstellar upwind direction in ecliptic longitude ($\lambda \approx 230^\circ$). The other two spectra appear to be shifted to higher speeds and show a distinct tail extending to higher speeds, which indicates the acceleration of He^+ ions. In the lower right panel of Fig. 3 the He^{2+} spectra taken in the main channel are displayed for one 5 min interval within each considered time period. Obviously, the channel switch and thus the 10% value of the threshold rate occurs at a higher $w_{\text{He}^{2+}}$ in the time periods with compressed solar wind where PUI acceleration is observed when compared with quiet solar wind. Furthermore, the count rate decrease as a function of $w_{\text{He}^{2+}}$ is steeper in the quiet solar wind than right after the stream interface. Both effects lead to low $w_{\text{He}^{2+},10\%}$ values in the quiet wind and enhanced $w_{\text{He}^{2+},10\%}$ values in compressed wind and thus supposedly in acceleration sites. The increased threshold speed $w_{\text{He}^{2+},10\%}$ can be traced to three different causes or a combination of them: 1) the acceleration efficiency is high, which expresses itself as a hard spectrum in $w_{\text{He}^{2+}}$ (gray spectrum); 2) a large fraction of the He^{2+} distribution is injected into acceleration; or 3) the density of solar wind He^{2+} is very high, e.g., due to a solar wind compression. Both 2) and 3) would push the He^{2+} spectrum to higher $w_{\text{He}^{2+},10\%}$ values (as in the green spectrum). All three effects are expected to occur in conjunction with solar wind compression regions and thus also to lead to effective He^+ acceleration.

Figure 4 shows a composite 2D histogram of the normalized He^+ PUI counts as a function of V_r versus $w_{\text{He}^{2+},10\%}$ accumulated for time intervals in the PUI crescent region ($230^\circ \leq \lambda \leq 280^\circ$). At these ecliptic longitudes the PUI injection speed is almost constant with variations $\lesssim 5 \text{ km s}^{-1}$. When a He^{2+} spectrum is measured that results in $w_{\text{He}^{2+},10\%} > 1.35$, the He^+ distributions appear to extend to substantially higher speeds. This observation seems to indicate that under this condition the assumption of a cutoff VDF with comparable shape independent of ecliptic longitude is violated. To ensure that the cutoff VDF has a comparable shape and to minimize this effect on the λ_{flow} determination, we filter the entire data set by requiring $w_{\text{He}^{2+},10\%} \leq 1.35$.

Of course, the method we use to exclude acceleration sites is an empirical approach that is not based on an evaluation of the details of the physical processes that lead to tails or a shift of the PUI VDF to higher speeds. However, as can be seen from the example in Fig. 3, all three effects that can lead to a local appearance of accelerated He^{2+} and thus per inference of He^+ PUIs

* $\arctan 2$ is the four-quadrant inverse tangent, which is sensitive to the signs of the arguments.

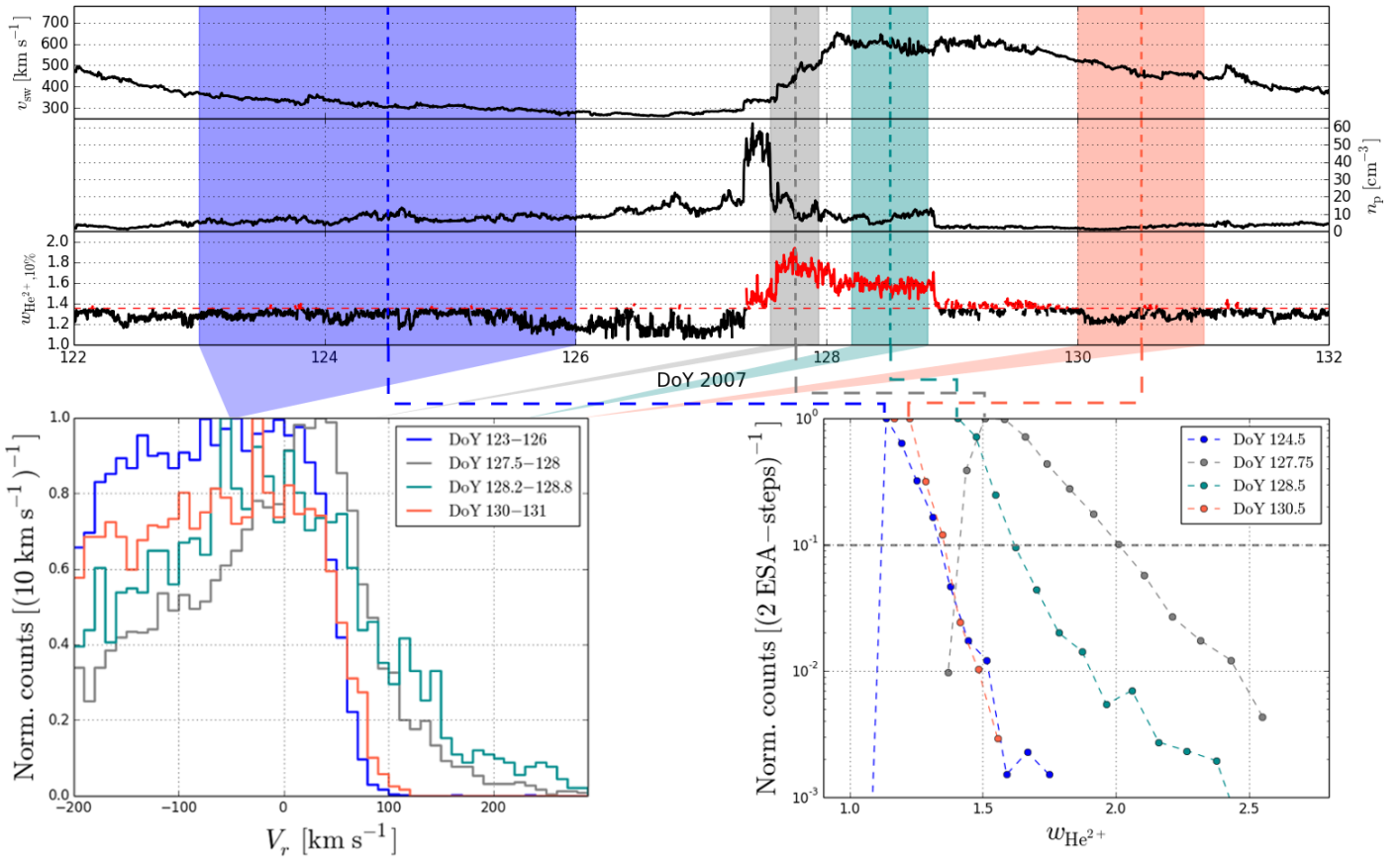


Fig. 3. Upper panel: Solar wind speed, proton density, and the parameter $w_{\text{He}^{2+},10\%}$ derived from the He $^{2+}$ VDF. Four time periods are marked that correspond to quiet solar wind (blue and red), compressed wind after the stream interface (gray), and compressed fast wind (cyan). Time periods that are displayed with the red solid line in the $w_{\text{He}^{2+},10\%}$ panel are excluded from our analysis. Lower left panel: He $^+$ count histograms measured in the marked time periods. Lower right panel: He $^{2+}$ VDF measured by the sensor's main channel in one 5 min interval within the considered time periods.

seem to be captured by this method. A more detailed investigation of these observations and their implications goes beyond the scope of this work and may be the subject of an independent follow-up investigation. Figure 4 shows that our empirical approach to use the value $w_{\text{He}^{2+}}$ where the He $^{2+}$ distribution exceeds a threshold flux serves as a good indicator for acceleration of He $^+$ PUIs.

4.4. Determining the pickup ion cutoff speed

The concept we use to determine λ_{flow} from the variation of the cutoff speed is identical to that of the method described in Möbius et al. (2015). First, the data is filtered for suitable IMF configurations (Sect. 2), and sites of strong local acceleration are excluded (Sect. 4.3) to ensure that the shape of the PUI cutoff is approximately the same. Then, the data is split into bins of ecliptic longitude, for which a histogram of the He $^+$ counts as a function of V_r is created. The speed V_r of each He $^+$ count is calculated from the He $^+$ speed in the solar wind frame and the solar wind speed. It is introduced more explicitly in the following section. For each histogram, the cutoff speed is determined, and λ_{flow} is derived from the variation of these speeds with longitude. However, we introduce improvements in each of these steps that are described in the following sections. An overview of the analysis including an example for each step of the analysis is illustrated in Fig. 5.

4.4.1. Frame of reference

Due to the pickup process, the speed of PUIs is always related to the ambient solar wind speed. This is why the PUI VDF has commonly been considered in terms of the PUI speed normalized to the solar wind speed, $w_{\text{He}^+} = \frac{v_{\text{He}^+}}{v_{\text{sw}}}$, which is typically considered in the spacecraft frame of reference (see Kallenbach et al. (2000)). However, in this frame the speed of a freshly injected ion is not constant due to the gyration about the IMF. For example, the speed of a PUI created from a neutral at rest alternates between 0 and the maximum speed of $2v_{\text{sw}}$ for an IMF configuration perpendicular to the solar wind. Furthermore, the maximum speed of a freshly injected PUI depends on the IMF orientation. Only the velocity component perpendicular to the IMF of the relative motion of the former neutral and the solar wind is crucial for the gyration speed. For example, in Fig. 1 a non-perpendicular IMF orientation is illustrated, where obviously the freshly injected torus PUIs reach a substantially lower maximum speed in the spacecraft frame than $2v_{\text{sw}}$. Considering the cutoff VDF in this frame, it is clear that it is severely influenced by the IMF orientation.

As already mentioned in Sec. 2, transforming the PUI speed into the solar wind frame of reference has the advantage that for a given solar wind speed, the injection speed of freshly injected PUIs is conserved for a given ecliptic longitude under any IMF orientation. Therefore, in Drews et al. (2015), the data product $w'_{\text{He}^+} = \frac{v'_{\text{He}^+}}{v_{\text{sw}}}$ has been introduced. This data product has also been

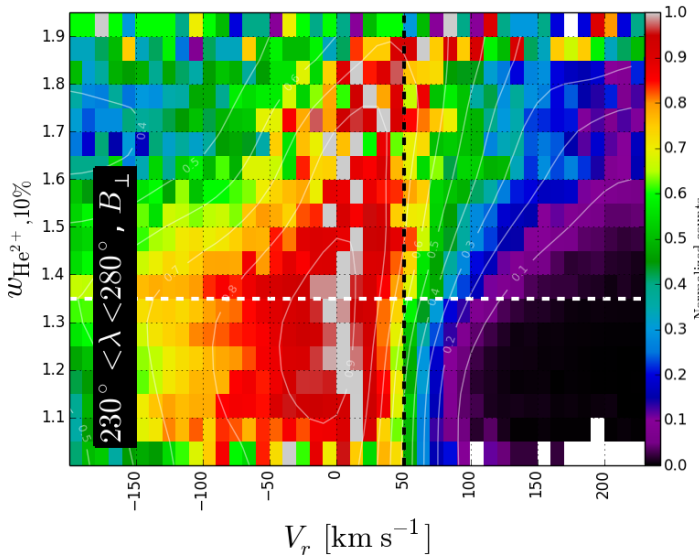


Fig. 4. Two-dimensional histogram of He^+ PUI counts in the crescent range of ecliptic longitude ($230^\circ \leq \lambda \leq 280^\circ$) depending on V_r and $w_{\text{He}^{2+},10\%}$. Only IMF configurations where the torus VDF of freshly injected PUIs is measured by PLASTIC's aperture are considered by selecting $-15^\circ \leq \Theta_{\text{GC}} \leq 15^\circ$ and $-15^\circ \leq \Phi_{\text{GC}} \leq 15^\circ$. The counts per bin are normalized to the maximum of each $w_{\text{He}^{2+},10\%}$ bin. The nominal cutoff in this range of ecliptic longitude is indicated by the vertical black dashed line. Above $w_{\text{He}^{2+},10\%} = 1.35$ (white dashed line) the cutoff smears out to higher speeds, which indicates that acceleration processes must have acted on the He^+ VDF.

utilized in Möbius et al. (2015) to determine the cutoff speed. However, using this quantity introduces an implicit dependence of the variation of the cutoff speed with longitude on the solar wind speed through the normalization in w'_{He^+} . This effect can be demonstrated by considering a simplified situation: for ecliptic longitudes close to the interstellar upwind direction, the interstellar neutrals stream anti-parallel to the solar wind with a speed $V_n \approx 50 \text{ km s}^{-1}$ with respect to the Sun. Therefore, their injection speed in the solar wind frame equals the relative speed between the neutrals and the solar wind. Assuming a solar wind speed, $v_{\text{sw},1} = 300 \text{ km s}^{-1}$, the injection speed would be $v_{\text{inj},1} = 350 \text{ km s}^{-1}$; at a higher solar wind speed of $v_{\text{sw},1} = 600 \text{ km s}^{-1}$, the injection speed would be $v_{\text{inj},1} = 650 \text{ km s}^{-1}$. In terms of w_{He^+} , these injection speeds correspond to $w_{\text{He}^{+,1}} = 1.17$ and $w_{\text{He}^{+,2}} = 1.08$ for the same ecliptic longitude. Thus, the cutoff speed in terms of w_{He^+} shows a clear dependence on solar wind speed. Because the neutral particle speed is constant at a given ecliptic longitude and does not depend on the solar wind speed, it is not advisable to use the normalized PUI velocity for the evaluation of the interstellar neutral gas flow.

Therefore, we chose to consider the cutoff in terms of V_r :

$$V_r = v'_{\text{He}^+} - v_{\text{sw}} \quad (4)$$

The first term, $v'_{\text{He}^+} = |\mathbf{v}_{\text{He}^+} - \mathbf{v}_{\text{sw}}|$, corresponds to the PUI speed in the solar wind frame of reference (see Fig. 1). PLASTIC is able to measure this speed because information about the ion incident angle is provided by the azimuthal deflection steps and the latitudinal position bins (see Sec. 3). Thus, V_r is the difference between the PUI speed and the ideal torus shell, which is also illustrated in Fig. 2 c. Throughout this paper, we use He^+ histograms in terms of V_r with a bin-width of 10 km s^{-1} .

4.4.2. Techniques for determining cutoff speed

In Möbius et al. (2015) a tanh-function is utilized to fit the cutoff in the He^+ spectra in every ecliptic longitude bin. The point of inflection of the tanh-function is then used as the cutoff speed. This method is illustrated in the upper panel of Fig. 5 b. It yields reasonable results for the cutoff speeds if the He^+ counting statistics are sufficiently high in the considered bin of ecliptic longitude. If the He^+ counting statistics in the ecliptic longitude bin is very low (maximum of ~ 10 counts/bin in the V_r histogram) the counts per bin are strongly fluctuating due to statistical noise. In this case, the tanh-fit of the cutoff is likely to yield highly variable results for the cutoff speeds that deviate significantly from the expected values.

Therefore, we developed another method to determine the cutoff speed that is independent of a functional fit to the histogram. Instead, we smooth the histogram with a $3-V_r$ -bin weighted running average, where the weights are calculated from a normal distribution centered on the considered bin with a width of 3 bins. Additionally, a cubic interpolation is calculated for the smoothed data. Using this interpolation we define the cutoff speed as the speed where this interpolation matches 50% of the maximum of the smoothed data. An example of this method for a given bin of λ is displayed in the middle panel of Fig. 5 b. The results of this procedure are expected to be similar to those returned by the fit method as the tanh-function also has its point of inflection at 50% of its maximum.

We also developed a third option to determine the cutoff speed that is independent from the other two methods to check how the cutoff determination method affects the result for the interstellar flow longitude. This method relies on the maximization of the correlation between the measured distributions and a reference curve. The reference curve is derived from data accumulated over a range of ecliptic longitude of $250^\circ < \lambda < 260^\circ$ as no significant changes of the nominal cutoff speed are expected in this range. Furthermore, the reference curve is smoothed with a three-bin running-average. In each bin of ecliptic longitude, the measured spectra are now shifted in V_r such that the correlation between the spectrum and the reference curve reaches a maximum. This means that in order to find the offset ΔV_r , we need to add to the measured spectra to obtain a maximum correlation coefficient calculated with the reference curve. As we are only interested in the part of the distribution where the cutoff is located, we focus on the range $0 \text{ km s}^{-1} < V_r < 120 \text{ km s}^{-1}$ of the reference curve. In the lower panel of Fig. 5 b, a demonstration of this method is given. The shift, ΔV_r , that is applied to the data to reach the maximum correlation in one bin of ecliptic longitude is taken as the relative cutoff value. As we are comparing each cutoff VDF with the reference curve taken from the crescent, we expect the highest shift ΔV_r in the focusing cone and $\Delta V_r \approx 0 \text{ km s}^{-1}$ in the crescent. This means that the sign of the ΔV_r needs to be flipped to obtain the same curve shape of cutoff speed versus ecliptic longitude as the other two methods obtain, and which is shown in Fig. 5 c. However, the sign of ΔV_r is irrelevant with respect to the λ_{flow} determination methods introduced in the next section.

In Sec. 6.1 we apply all three methods to the same data set and compare the results obtained for the interstellar flow longitude.

4.5. Determining the interstellar flow longitude

In Möbius et al. (2015) the authors propose that a precise method for determining the interstellar flow longitude, λ_{flow} , from the PUI cutoff is to calculate a mirror-correlation coefficient, C_m , for

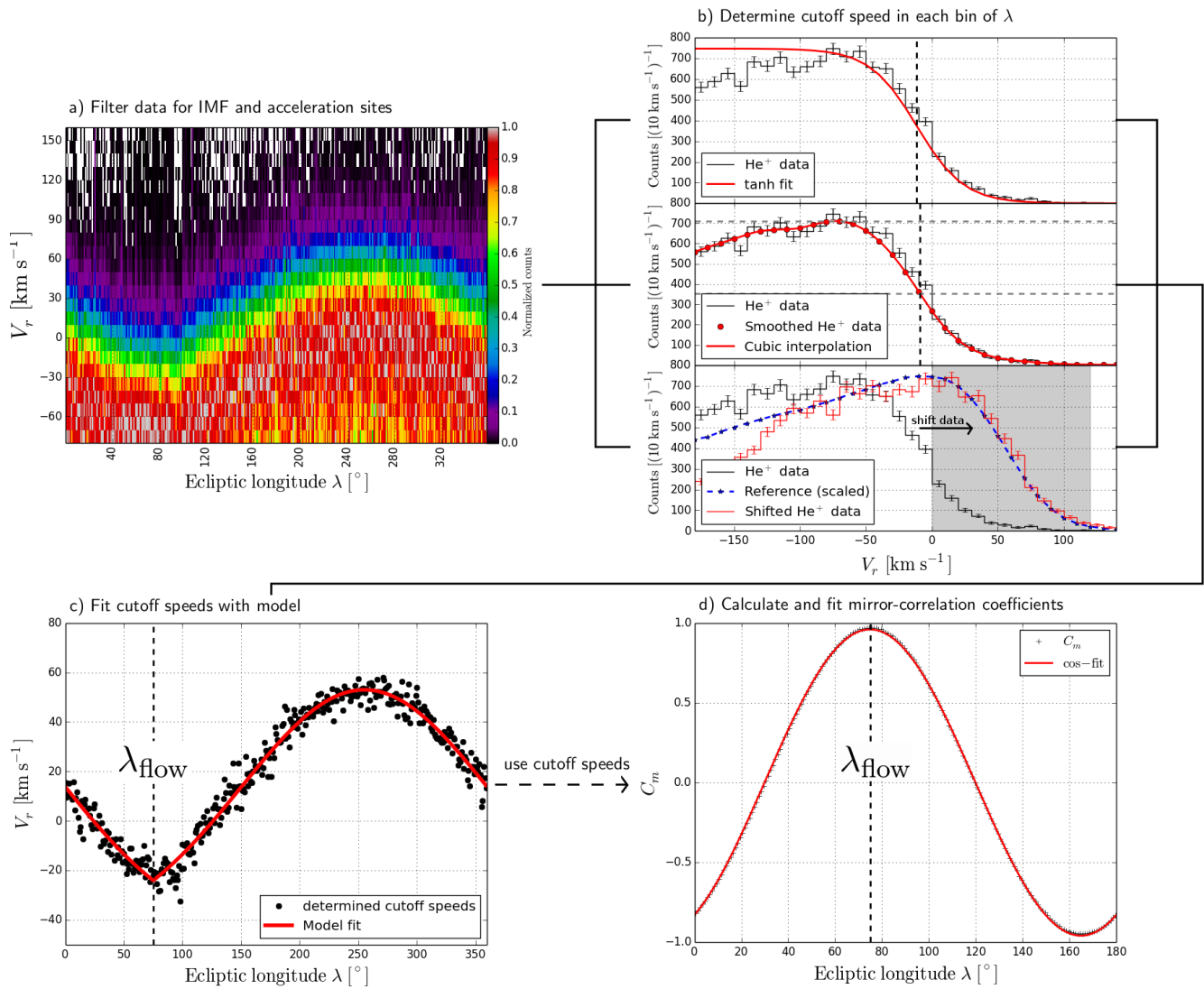


Fig. 5. a) Two-dimensional histogram of He⁺ counts as a function of ecliptic longitude, λ , and V_r . The data have been filtered for IMF orientation according to $-15^\circ \leq \Theta_{\text{GC}} \leq 15^\circ$ and $-15^\circ \leq \Phi_{\text{GC}} \leq 15^\circ$ (see Sects. 3 and 6), and acceleration sites by requiring $w_{\text{He}^{2+},10\%} \leq 1.35$ (see Sect. 4.3). The counts per bin are normalized to the maximum of each λ bin. b) Demonstration of the three cutoff determination techniques performed on the example of bin $\lambda = 100^\circ$. The upper panel shows the tanh-fit as used in Möbius et al. (2015), the middle panel shows the 50% threshold method, and the lower panel illustrates the maximization of the correlation coefficient with a reference curve. c) Resulting cutoff speeds from the threshold method as a function of λ . The interstellar flow longitude is determined by fitting Eq. 5 to the results. d) Mirror-correlation coefficients for every bin of λ calculated from the cutoff speeds. The interstellar flow longitude is determined by fitting a cos-function to the resulting correlation coefficients.

every bin of ecliptic longitude and then fit this data with a cos-function with variable amplitude and phase. The resulting value for the phase-parameter corresponds to the position of the focusing cone or crescent, respectively. An example of this method is shown in Fig. 5 d). The main advantage of this method is that it is completely independent from any model of the radial neutral particle speed as the only assumption is that it is symmetric about the flow direction. The disadvantage is that it neglects that the STEREO A orbit is not a perfect circle, which of course affects the symmetry of the measured cutoff speeds and introduces a systematic error on the order of $\Delta\lambda_{\text{flow}} \approx 0.1^\circ$, which is discussed in Möbius et al. (2015).

In Möbius et al. (2015) an analytical model for the radial neutral

particle speed at 1 AU is also given,

$$v_{n,r}^2 = 2 + v_{\text{ISN}\infty}^2 - (1 - \cos \lambda) - \left[v_{\text{ISN}\infty}^2 \sin^2 \lambda + v_{\text{ISN}\infty} \sin |\lambda| \sqrt{v_{\text{ISN}\infty}^2 \sin^2 \lambda + 4(1 - \cos \lambda)} \right] / 2, \quad (5)$$

where $v_{n,r} = \frac{V_{n,r}}{V_E}$ and $v_{\text{ISN}\infty} = \frac{V_{\text{ISN}\infty}}{V_E}$ is the neutral particle speed at the observer and infinity, respectively, normalized to $V_E = \sqrt{\frac{GM_S}{R_E}}$ with the gravitational constant, G ; solar mass, M_S ; and Sun–Earth distance, $R_E = 1$ AU. The interstellar flow longitude, λ_{flow} , is connected to λ via $\lambda = \lambda_{\text{Obs}} - \lambda_{\text{flow}} - 180^\circ$. We note that this equation has been derived under the assumption that the orbital plane of the neutrals is equivalent to the ecliptic plane, which means that the latitudinal tilt of the interstellar neutral flow has been neglected.

Using this equation, one can also perform a three-parameter least-squares fit of the cutoff speed data with λ_{flow} , $V_{\text{ISN}\infty}$, and an offset as free parameters. By using the known relation of ecliptic longitude and solar distance of STEREO A, it is easy to consider the STEREO A orbit in this fit by renormalizing the parameters. The model matches the data reasonably, which can be seen in the example in Fig. 5 c.

We use both of these methods for the determination of the interstellar flow longitude from the He^+ cutoff values and compare the results in Sec. 6.1.

5. Error estimation

Concerning the estimated error that our analysis yields for λ_{flow} , we distinguish between two different errors related to their different sources. On the one hand, our analysis has a statistical error due to the limited He^+ counts. On the other hand, varying solar wind conditions that slightly influence the determined cutoff speeds may lead to a systematic but stochastically distributed error. Both errors can be estimated using Monte Carlo techniques. Generally, count rates such as those in the V_r histograms for every bin of ecliptic longitude follow Poisson statistics. Thus, we estimate the statistical error by adding Poissonian noise according to the counting statistics for each bin to the V_r histograms and repeating the analysis $N = 1000$ times using data sets modified in this way. The standard deviation of the results for λ_{flow} serves as our estimate for the purely statistical error.

The estimate of the stochastic error is a little more involved. Here, we exploit that our data consist of seven STEREO A orbits. Thus, there are seven independent and decoupled measurements of the cutoff under different solar wind conditions. By discarding two orbits of data each time, we get 21 different combinations of five out of seven orbits with sufficient statistics that we can utilize to estimate the error of our analysis that is introduced by the slight variation of the cutoff due to varying solar wind conditions. This method is closely related to the error estimation for λ_{flow} utilized by Drews et al. (2012). In the approach applied in this work, variations of the interplanetary conditions introduce stochastically distributed fluctuations in the PUI flux, which is utilized to determine the location of the focusing cone and crescent. Consequently, we derive the cutoff in every bin of ecliptic longitude for all 21 combinations of 5 orbits. Afterwards, we determine λ_{flow} $N = 1000$ times by randomly choosing one of these 21 results in every bin of ecliptic longitude. The standard deviation of the results for λ_{flow} serves as our total error estimate that includes both error sources.

6. Results

In the previous sections, we presented approaches to eliminate systematic effects that may influence the result for the interstellar flow longitude, λ_{flow} , derived from the PUI cutoff and a new approach for estimating the error of the obtained λ_{flow} value. Now we apply this modified analysis to STEREO A/PLASTIC He^+ PUI observations from 2007 through 2014.

6.1. Updated results for the interstellar flow longitude

First, we compare how the different methods for determining cutoff and the two different options used to derive the interstellar flow longitude from the cutoff speeds affect the results. For this, we take data filtered for IMF configurations where the PUI torus

is supposedly covered by PLASTIC's velocity space coverage. To ensure that the torus is inside PLASTIC's aperture in the latitudinal and longitudinal direction we restrict the data to IMFs where $-15^\circ \leq \Theta_{\text{GC}} \leq 15^\circ$ and $-15^\circ \leq \Phi_{\text{GC}} \leq 15^\circ$, respectively. The bin width of ecliptic longitude is chosen to be $\Delta\lambda = 1^\circ$. To demonstrate the effect of acceleration sites on the analysis, we compare how the filter for $w_{\text{He}^{2+},10\%} \leq 1.35$ influences the obtained values for λ_{flow} and its errors. The results are summarized in Table 1.

First of all, the result that the observed curve of the cutoff speeds (Fig. 5 c) fits the predicted behavior of the injection speed (Fig. 2 b) shows that the assumption that we can relate the PUI cutoff speed to the injection speed is justified. Furthermore, the stochastic errors of all methods are significantly smaller than one bin width and the very high correlation coefficients of the mirror-correlation imply a high level of symmetry.

Considering the results from the data set, which has not been filtered for acceleration sites, one can see that the results derived from the different cutoff determination techniques deviate significantly from each other. In particular, the λ_{flow} values derived from the tanh-fit and the 50% threshold technique do not agree within their mutual stochastic errors. Apparently, different cutoff determination techniques have a different sensitivity to the impact of acceleration sites. The systematic errors that are introduced, which are stochastically distributed over ecliptic longitude, lead to the differences in the results for λ_{flow} .

This is not the case for the data set in which acceleration sites have been excluded. The 50% threshold method shows a small deviation ($\Delta\lambda_{\text{flow}} \approx 0.25^\circ$) from the other two methods that obtain very similar results ($\Delta\lambda_{\text{flow}} \approx 0.04^\circ$). However, all values agree within their mutual uncertainties, both statistical and stochastic. Furthermore, a decrease of the stochastic errors is observed when filtering the data for acceleration sites. This is also supported by the increase in the maximum mirror-correlation coefficient, which implies that an enhanced symmetry of the cutoff speeds is obtained. These results support the conclusion that it is necessary to exclude acceleration sites from the data. Consequently, we only discuss the results obtained from the filtered data in the following.

All results for λ_{flow} from the filtered data show a significant deviation of $\Delta\lambda_{\text{flow}} \approx -1^\circ$ from the value presented in Möbius et al. (2016a): $\lambda_{\text{flow}} = 76.19^\circ \pm 0.04^\circ$. The statistical error is in all cases slightly larger than the value of $\sigma_{\text{stat.}} = 0.15^\circ$ estimated in Möbius et al. (2016b). Furthermore, the tanh-fit method seems to be most affected by statistical fluctuations, while the maximum correlation method is the most stable with respect to statistics. Interestingly, this trend is inverted for the stochastic error, which is introduced by the variability of solar wind conditions. It is about a factor of two larger than the statistical error. The uncertainty for λ_{flow} given in Möbius et al. (2016a) was highly underestimated as the stochastic error derived with our approach is about one order of magnitude larger. However, Möbius et al. (2015, 2016a) explicitly noted that their error estimate was solely based on statistical considerations and that systematic errors would likely be larger and still needed to be studied. In any case, the difference between the obtained errors of the different cutoff determination techniques is on the order of 10%. While inside the stochastic uncertainties, there seems to be a consistent difference between the interstellar flow longitude determined from the mirror-correlation and the direct fit with Eq. 5. The cos-fit of the mirror-correlation coefficients obtained λ_{flow} values that are $\Delta\lambda_{\text{flow}} \approx 0.2^\circ$ lower than those derived from the fit of Eq. 5 to the cutoff speeds. To some extent, this may be connected to the non-circular orbit of STEREO A, which is consid-

Table 1. Results for the interstellar flow longitude, λ_{flow} , from the He^+ PUI cutoff derived from three different methods to determine cutoff and two different ways to determine λ_{flow} from the cutoff speeds. Furthermore the maximum of the mirror-correlation coefficients, $\max(C_m)$, and the errors, $\sigma_{\text{stat.}}$ and $\sigma_{\text{stoch.}}$ discussed in Sec. 5 are displayed. The IMF filter was set to $-15^\circ \leq \Phi_{\text{GC}} \leq 15^\circ$ and $-15^\circ \leq \Theta_{\text{GC}} \leq 15^\circ$. For the results displayed in the lower rows, we required $w_{\text{He}^{2+},10\%} \leq 1.35$ in the data selection to exclude acceleration sites.

Method	Mirror-correlation				Model-fit		
	λ_{flow} [°]	$\max(C_m)$	$\sigma_{\text{stat.}}$ [°]	$\sigma_{\text{stoch.}}$ [°]	λ_{flow} [°]	$\sigma_{\text{stat.}}$ [°]	$\sigma_{\text{stoch.}}$ [°]
<i>without $w_{\text{He}^{2+},10\%}$ filter:</i>							
tanh-fit	75.33	0.965	0.27	0.45	75.62	0.24	0.45
50% threshold	76.11	0.954	0.18	0.54	76.39	0.16	0.50
max. correlation	75.78	0.968	0.17	0.45	75.98	0.15	0.43
<i>with $w_{\text{He}^{2+},10\%}$ filter:</i>							
tanh-fit	75.18	0.975	0.23	0.35	75.41	0.22	0.34
50% threshold	74.88	0.971	0.20	0.36	75.17	0.18	0.35
max. correlation	75.15	0.974	0.18	0.41	75.34	0.16	0.39

ered in Eq. 5 and not in the mirror-correlation approach, but it is likely not the entire reason because the estimated difference for the ellipticity is smaller. Furthermore, comparing the statistical and stochastic errors estimated for the two different λ_{flow} determination methods, it can be seen that both produce comparable uncertainties.

6.2. Influence of Φ_{GC} on λ_{flow} results

The enhanced data quality that is established by the improvements of the method makes it possible to study further systematic influences on the results for λ_{flow} . A key parameter that affects the PUI VDF, and therefore the PUI transport, is the IMF orientation. As we are only interested in the interstellar flow longitude, the parameter Φ_{GC} is crucial as a latitudinal transport effect or the latitudinal orientation of the torus is not supposed to affect the derived interstellar flow longitude.

Thus, we perform the analysis with data sets filtered for different IMF configurations and focus on the parameter Φ_{GC} . We require again that $-15^\circ < \Theta_{\text{GC}} < 15^\circ$ to ensure that the ideal torus falls into PLASTIC's FoV in the range of $-22.5^\circ \lesssim \Phi_{\text{GC}} \lesssim 22.5^\circ$. Furthermore, we still exclude sites with enhanced local acceleration signatures by filtering the data for $w_{\text{He}^{2+},10\%} \leq 1.35$. As we want to explore the entire range of possible Φ_{GC} angles, this means that the ideal torus is not necessarily in PLASTIC's FoV, in particular in the range $|\Phi_{\text{GC}}| \gtrsim 22.5^\circ$. For the cutoff determination method we chose the 50% threshold approach as this method copes best with low statistics, which can occur due to the narrow selection of IMF data. For the determination of λ_{flow} the direct model fit was chosen, because of the smaller uncertainties and the elliptical orbit of STEREO A which is considered in the model.

In Fig. 6 one can see the results for λ_{flow} over the Φ_{GC} range. It is apparent that for IMF configurations where an ideal torus would be measured by PLASTIC's aperture (red shaded area) the result for λ_{flow} depends approximately linearly on the selected Φ_{GC} range. This trend seems to continue for configurations where an ideal torus would be just outside PLASTIC's aperture, which is probably related to the non-zero width of a real torus VDF. At magnetic field configurations where the torus is clearly outside of PLASTIC's aperture ($|\Phi_{\text{GC}}| \gtrsim 40^\circ$) no correlation between the IMF configuration and the result for λ_{flow} is observed, although these data points have comparatively large error bars. We also performed this analysis using the other cutoff determination methods, which produced similar results and in particular the same clear trend that can be seen in Fig. 6.

Comparing these results to the values determined from a broad

range of IMF data that are displayed in Table 1, one can see that these values are slightly lower than the intersection of the curve in Fig. 6 with $\Phi_{\text{GC}} = 0^\circ$, but within the stochastic uncertainties. This difference may be caused by the fact that IMF angles with $\Phi_{\text{GC}} > 0^\circ$ occur more frequently than IMF angles with $\Phi_{\text{GC}} < 0^\circ$, because angles with $\Phi_{\text{GC}} > 0^\circ$ are closer to the Parker angle which corresponds to the mean IMF.

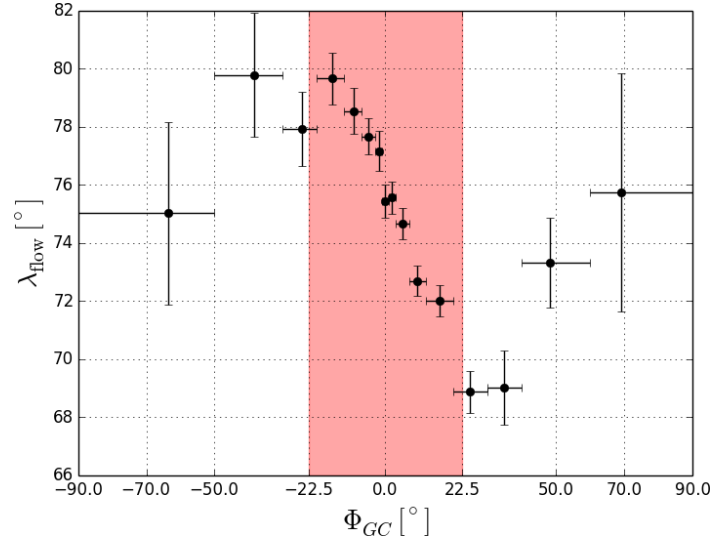


Fig. 6. Results of λ_{flow} for different selections of IMF orientations in terms of Φ_{GC} . Due to the small sample size, especially in the $|\Phi_{\text{GC}}| \gtrsim 40^\circ$ region, a comparatively coarse resolution in ecliptic longitude of $\Delta\lambda = 4^\circ$ was chosen for the analysis. The error of λ_{flow} corresponds to the stochastic error, while the errorbars in Φ_{GC} illustrate the selected Φ_{GC} range. The data points are displayed at the mean Φ_{GC} value for each range. The red area corresponds to the values where an ideal torus would be detected by PLASTIC neglecting STEREO A's eigen-velocity.

7. Discussion

As already mentioned in the previous section, the results listed in Table 1 deviate considerably from the result presented in Möbius et al. (2016a), $\lambda_{\text{flow}} = 76.19^\circ \pm 0.04^\circ$. This supports the hypothesis that systematic influences like the dependence of the cutoff speed on the solar wind speed, which we eliminated by deriving the cutoff in terms of V_r instead of w_{sw} , or the presence of acceleration sites may have a strong impact on the result for λ_{flow} , which cannot be neglected. Our error estimate, which now includes contributions from stochastically distributed variations

in the interplanetary conditions, is about one order of magnitude higher for our results than presented in Möbius et al. (2015, 2016a), which is solely the pure fit error of the cos-fit to the mirror-correlation coefficients. The errors presented in Table 1 are derived from a totally different approach. On the one hand, it takes into account the limited counting statistics; on the other hand, the varying solar wind conditions that can slightly influence the cutoff are considered. Nevertheless, one can see that the data quality is improved compared to the previous results. The maximum of the mirror-correlation coefficients shown in Möbius et al. (2016a) is clearly below 0.900, while with our introduced improvements mirror-correlation coefficients of up to 0.974 are reached. This implies that the curve of the cutoff speed versus ecliptic longitude shows an enhanced symmetry which enables a more precise determination of λ_{flow} . Apparently, the filter for suited IMF directions has a considerable impact on the result for the interstellar flow longitude derived from the PUI cutoff. This in turn means that when accumulating the data over a wide range of IMF configurations, as we did to derive the values displayed in Table 1 and as was performed in Möbius et al. (2016a), the result for λ_{flow} strongly depends on the mix of IMF angles. Additionally, this dependence plays a role in the stochastic error. As every orbit consists of a unique mix of IMF configurations, the cutoff speed in every orbit varies stochastically. The reason for this dependence must be connected to the torus VDF of freshly injected PUIs and its anisotropy. Furthermore, whatever causes this effect must systematically depend on the combination of ecliptic longitude and IMF as otherwise no asymmetry in the cutoff speeds would be introduced. For example, an effect that would increase the cutoff speed independently of the longitudinal position of STEREO A would just affect the offset parameter in the fit of the model based on Eq. 5 and not λ_{flow} . This argument is, of course, also valid for the fit of the mirror-correlation coefficients. Only if the cutoff is altered together with a longitudinal dependence is the result for λ_{flow} affected.

One possible process that could produce the observed signature is longitudinal transport. As PUIs remain gyrotropic at all times due to the Lorentz-force, their guiding-center velocity depends on the local IMF orientation. If we assume that PUIs are transported towards higher ecliptic longitudes between their time of injection and the time when they are measured, a systematically lower cutoff is determined at $\lambda \approx 150^\circ$ and a systematically higher cutoff is determined at $\lambda \approx 350^\circ$ (Fig. 5 c). This would shift the entire cutoff speed curve towards higher ecliptic longitudes and thus an increased value for λ_{flow} would be determined. One might surmise that under a perfectly perpendicular IMF orientation ($\Phi_{\text{GC}} = 0^\circ$) the nominal λ_{flow} would be determined. However, STEREO A's eigen-velocity (which affects the velocity-space coverage of PLASTIC), possible asymmetries of the PUI torus VDF (Drews et al. 2015), and the unknown history of the locally measured IMF transform this into a more involved problem whose individual effects need to be studied separately before being included either in the data selection or through appropriate corrections. Furthermore, PLASTIC's instrument function and, in particular, the efficiency of the position bins that are used to transform the measured speed into the solar wind frame, are complex and not well determined. Hence, we cannot yet exclude that the signature presented in Fig. 6 is caused by the interplay of the complexities of the PUI VDF and PLASTIC's instrument function. For this reason, additional observational constraints and a better understanding of the PUI transport effects will have to be developed. These investigations go

beyond the scope of this work and will be included in a separate study in the near future.

8. Conclusion

We have revisited the determination of the interstellar flow longitude based on the PUI cutoff proposed by Möbius et al. (2015). In the first part of this work, we focused on the improvement of the analysis. By using V_r instead of w_{sw} we eliminated a possible systematic influence caused by solar wind speed variations. Another problem that we addressed was the impact of local acceleration sites, which constitute a possible source for systematic uncertainties in the cutoff determination that are stochastically distributed over ecliptic longitude. Thus, they can affect the derivation of λ_{flow} and, of course, increase the uncertainty of the result. By considering the VDF of He^{2+} we were able to exclude them to a large extent.

For the determination of the cutoff speed, we have proposed two new methods, which we show are consistent with the previously used method. A new approach to estimate the error of the analysis was introduced. On the one hand, the statistical error caused by the limited number of He^+ counts was considered; on the other hand, a stochastic error caused by varying solar wind conditions was taken into account. Both errors were estimated using Monte Carlo approaches. The results of the modified analysis deviate by $\Delta\lambda_{\text{flow}} \approx -1^\circ$ from the result presented in Möbius et al. (2016a). This illustrates how the systematic errors that we claim to have minimized, have an impact on the result for λ_{flow} . The resulting stochastic errors of $\sim 0.4^\circ$ are about one order of magnitude larger than the error presented in Möbius et al. (2015, 2016a) of 0.04°.

Additionally, we found that a direct fit of a model to the data yields an error for the interstellar flow longitude comparable with calculating and fitting mirror-correlation coefficients. The advantage of the direct fit of the cutoff speeds is that the model incorporates the non-circular orbit of STEREO A, which introduces a systematic error in the mirror-correlation approach. Nevertheless, the mirror-correlation coefficients calculated for the cutoff speeds derived from the newly filtered data with the modified methods imply an improved data quality.

Using these improvements, we were able to uncover an unexpected systematic dependence of the derived interstellar flow longitude from the considered IMF configurations. This dependence is not only crucial for determining the actual interstellar flow longitude from the PUI cutoff, but is also very interesting for fundamental PUI transport physics.

This means that the λ_{flow} results of this study displayed in Table 1 and the value presented in Möbius et al. (2016a) are still influenced by the mix of IMF orientations that appear in the selection of the data used to derive these values. At this point, we would like to emphasize that with our current understanding the value of $\lambda_{\text{flow}} = 75.41^\circ \pm 0.34^\circ$ with the lowest stochastical uncertainty should not be taken as the real interstellar flow longitude. Our understanding of the involved processes is still not thorough enough to correct for the systematic trend that is introduced by the IMF orientation. Thus, we plan to investigate possible explanations for this effect in more detail and with a further refinement in the data selection in a follow-up study.

Acknowledgements. This work was supported by the German Space Agency (DLR) under grant number 50 OC 1501, and by the University of Kiel. The work at the University of New Hampshire is supported by SR&T Grant NNX16AF79G. Furthermore, we thank Sonja Taut for her help with Fig. 1 a.

References

- Acuña, M., Curtis, D., Scheifele, J., et al. 2008, Space Science Reviews, 136, 203
- Axford, W. 1972, NASA Special Publication, 308, 609
- Bertaux, J. & Blamont, J. 1971, Astronomy and Astrophysics, 11, 200
- Bzowski, M., Kubiak, M., Möbius, E., et al. 2012, The Astrophysical Journal Supplement Series, 198, 12
- Chalov, S. 2014, Monthly Notices of the Royal Astronomical Society: Letters, 443, L25
- Chotoo, K., Schwadron, N., Mason, G., et al. 2000, Journal of Geophysical Research: Space Physics, 105, 23107
- Drews, C., Berger, L., Taut, A., Pelekis, T., & Wimmer-Schweingruber, R. 2015, Astronomy & Astrophysics, 575, A97
- Drews, C., Berger, L., Taut, A., & Wimmer-Schweingruber, R. F. 2016, Astronomy & Astrophysics, 588, A12
- Drews, C., Berger, L., Wimmer-Schweingruber, R. F., et al. 2012, Journal of Geophysical Research: Space Physics, 117, n/a, a09106
- Drews, C., Berger, L., Wimmer-Schweingruber, R. F., et al. 2010, Journal of Geophysical Research: Space Physics, 115
- Fahr, H. 1971, Planetary and Space Science, 19, 1121
- Fisk, L. & Gloeckler, G. 2012, Space science reviews, 173, 433
- Galvin, A., Kistler, L., Popecki, M., et al. 2008, Space Science Reviews, 136, 437
- Gloeckler, G. 1999, in Corotating Interaction Regions (Springer), 91–104
- Gloeckler, G., Geiss, J., Roelof, E., et al. 1994, Journal of Geophysical Research: Space Physics, 99, 17637
- Jian, L., Russell, C., Luhmann, J., & Skoug, R. 2006, Solar Physics, 239, 337
- Kallenbach, R., Geiss, J., Gloeckler, G., & Von Steiger, R. 2000, Astrophysics and Space Science, 274, 97
- McComas, D., Allegrini, F., Bochsler, P., et al. 2009, science, 326, 959
- Möbius, E., Bochsler, P., Bzowski, M., et al. 2012, The Astrophysical Journal Supplement Series, 198, 11
- Möbius, E., Bzowski, M., Chalov, S., et al. 2004, Astronomy & Astrophysics, 426, 897
- Möbius, E., Hovestadt, D., Klecker, B., Scholer, M., & Gloeckler, G. 1985, Nature, 318, 426
- Möbius, E., Lee, M., & Drews, C. 2015, The Astrophysical Journal, 815, 20
- Möbius, E., Lee, M., & Drews, C. 2016a, The Astrophysical Journal, 826, 99
- Möbius, E., Lee, M., Gloeckler, G., Drews, C., & Keilbach, D. 2016b, in Journal of Physics: Conference Series, Vol. 767, IOP Publishing, 012017
- Möbius, E., Litvinenko, Y., Grüwaldt, H., et al. 1999, Geophysical research letters, 26, 3181
- Möbius, E., Rucinski, D., Hovestadt, D., & Klecker, B. 1995, Astronomy and Astrophysics, 304, 505
- Oka, M., Terasawa, T., Noda, H., Saito, Y., & Mukai, T. 2002, Geophysical research letters, 29, 54
- Quinn, P., Schwadron, N., & Möbius, E. 2016, The Astrophysical Journal, 824, 142
- Schwadron, N., Fisk, L., & Gloeckler, G. 1996, Geophysical research letters, 23, 2871
- Schwadron, N. A., Möbius, E., Leonard, T., et al. 2015, The Astrophysical Journal Supplement Series, 220, 25
- Sokół, J. M., Bzowski, M., Kubiak, M. A., & Möbius, E. 2016, Monthly Notices of the Royal Astronomical Society, 458, 3691
- Stone, E., Cummings, A., McDonald, F., et al. 2005, Science, 309, 2017
- Taut, A., Berger, L., Bochsler, P., et al. 2016, in AIP Conference Proceedings, Vol. 1720, AIP Publishing, 050001
- Vasyliunas, V. & Siscoe, G. 1976, Journal of Geophysical Research, 81, 1247
- Weller, C. & Meier, R. 1974, The Astrophysical Journal, 193, 471
- Witte, M. 2004, Astronomy & Astrophysics, 426, 835
- Wood, B. E., Müller, H.-R., & Witte, M. 2015, The Astrophysical Journal, 801, 62

5.3 FOLLOW-UP INVESTIGATIONS

5.3.1 Additional Observational Constraints

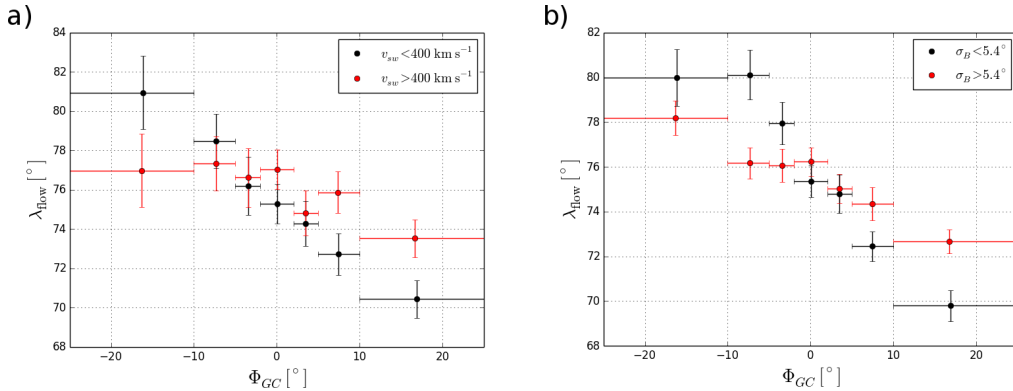


Figure 18: Further observational constraints related to the variation of the λ_{flow} result with IMF orientation, Φ_{GC} . a) Utilizing data sorted for solar wind speed: comparatively slow solar wind ($v_{\text{sw}} < 400 \text{ km s}^{-1}$) is displayed in black, faster solar wind ($v_{\text{sw}} > 400 \text{ km s}^{-1}$) in red. b) Utilizing data sorted for IMF variability: comparatively calm IMF ($\sigma_B < 5.4^\circ$) is displayed in black, variable IMF ($\sigma_B > 5.4^\circ$) in red.

To find additional observational constraints for the systematic effect of the IMF orientation on the λ_{flow} result presented in Fig. 6 of Taut et al. (2018), the analysis has been repeated filtering the data for different solar wind conditions. On the one hand, the data has been split into two ranges of solar wind speed, comparatively slow solar wind ($v_{\text{sw}} < 400 \text{ km s}^{-1}$) and fast solar wind ($v_{\text{sw}} > 400 \text{ km s}^{-1}$). The results are displayed in Fig. 18 a. As there is very poor statistics for IMF angles with $|\Phi_{\text{GC}}| > 40^\circ$, the focus is set on IMF configurations, where an ideal torus would fall into PLASTIC’s FoV. Apparently, the observed effect is more pronounced at low solar wind speeds than at high solar wind speeds. Additionally, it has been tested, if the observed variability of the IMF has an impact on the systematic trend of λ_{flow} with Φ_{GC} . We quantified this variability by considering 1-min mean IMF vectors. For every PLASTIC measurement cycle, the mean angular change of the IMF vector, σ_B , has been calculated in the time range ± 15 min of the considered measurement cycle. According to σ_B , the data set has been split in half, which corresponds to a limit of $\sigma_B = 5.4^\circ$. The results of the analysis of λ_{flow} vs. Φ_{GC} is displayed in Fig. 18 b. Again, a clear difference between the data sets is observed. In times with a calm IMF the effect is significantly more pronounced than in times with a high variability of the IMF orientation.

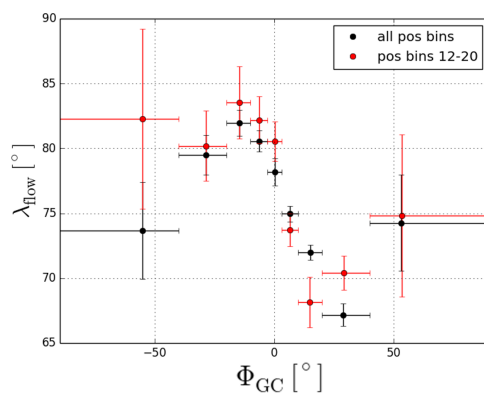


Figure 19: Analysis of the λ_{flow} result as a function of selected IMF orientation with two different FoVs: In black with the full FoV (all available position bins), in red a restricted FoV (position bins 12 to 20, see Fig. 20).

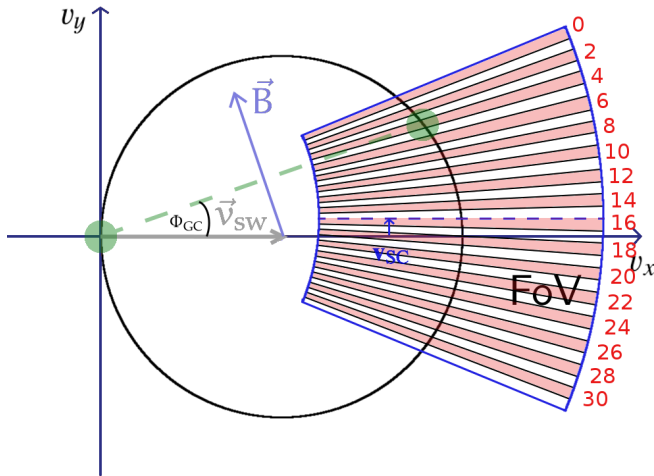


Figure 20: Velocity space sketch of the FoV of PLASTIC’s SWS and its position bin resolution in azimuthal direction. Inside this FoV PLASTIC can distinguish between 32 position bins. An example of an ideal torus VDF is illustrated (torus created from neutral at rest) and the angle Φ_{GC} is depicted, which follows from the IMF orientation. Thus for IMF orientations with $0^\circ < \Phi_{GC} < 22.5^\circ$ the ideal torus VDF would fall into position bins < 16 .

Another test we can perform is related to the FoV of PLASTIC. Due to its position sensitive detection system, one can artificially shrink the FoV in azimuthal direction by just selecting the central position bins. An illustration of the position bin coverage in velocity space is given in Fig. 20. The result of this restriction in the data set is displayed in Fig. 19. Compared to the data set, in which all position bins have been taken into account, the curve of λ_{flow} as a function of Φ_{GC} shows a steeper decrease.

5.3.2 Explanation for the Observed Effect

In Taut et al. (2018) it is surmised that again longitudinal transport of the PUIs leads to the observed trend of the λ_{flow} result as a function of IMF orientation displayed in Fig. 6 of the publication. The mechanism how this leads to the observed shift is displayed in Fig. 21. Due to the Lorentz force, PUIs are bound to the IMF line at any time. This means that the guiding center velocity, which depicts their average motion along the field line, is not necessarily equal to the radial solar wind velocity. Consequently, PUIs are transported in longitude, if they preserve their guiding center velocity for a prolonged time. In the middle panels of Fig. 21 a positive guiding center velocity in v_y corresponds to transport to increasing ecliptic longitude, a negative velocity to decreasing ecliptic longitudes. This means that PUIs from the initial torus VDF are transported to increased ecliptic longitudes at $\Phi_{\text{GC}} > 0^\circ$. In contrast to that, we observe for these IMF orientations a shift of λ_{flow} to decreased values implying a transport into the opposite direction. However, as indicated by the shaded hemispheres, more velocity space is covered for PUIs that have the contrary sign in the guiding center velocity. We assume that the torus distributed ions are locally injected and, thus, did not have sufficient time to be transported. However, the underlying distribution consists of ions that have already undergone a scattering process and are therefore likely to be older. These ions have had sufficient time to be transported and this transport is directed into the observed direc-

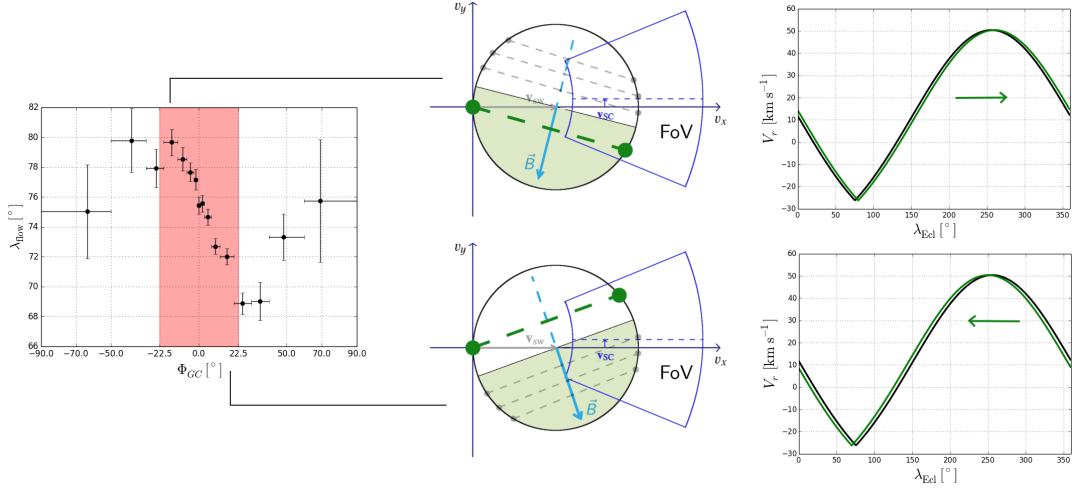


Figure 21: Illustration of longitudinal transport that is supposed to lead to the observed shift of the λ_{flow} result with **IMF** orientation. The middle panels show velocity space sketches for two given **IMF** orientations. As the **PUI** motion is bound to the **IMF**, the guiding center velocities in v_y direction are positive in the white hemisphere and negative in the grey hemisphere, which leads to longitudinal transport. The coverage of the **FoV** of these two areas depends on the **IMF** orientation, which may lead to the observation of a transport effect.

tion of the λ_{flow} shift. This mechanism fits well to the observations of the effect with respect to solar wind speed and **IMF** variability displayed in Fig. 18. The fast solar wind is commonly more turbulent than the slow solar wind (Tu and Marsch, 1995). Thus, more pitch-angle scattering is assumed to happen in the fast solar wind. For a transport effect, the **PUIs** need to preserve their pitch-angle for a prolonged time and thus pitch-angle scattering would hamper longitudinal transport. This is also in close relation to the variability of the **IMF** direction. Only under a stable **IMF** orientation the **PUIs** would be transported efficiently into one direction. In a highly variable **IMF** less transport would be observed and also more pitch-angle scattering would occur. However, the observation of a steeper curve in a narrower azimuthal **FoV** displayed in Fig. 19 does not fit this model. With such a restriction in the **FoV** only **PUIs** with a small longitudinal guiding-center velocity are sampled. A smaller guiding-center velocity would lead to less longitudinal transport and therefore a less steep signature would be expected from a narrower **FoV**.

Hence, we suggest an alternative mechanism that could create the observed trend of λ_{flow} with Φ_{GC} . We argue that the orientation of the initial torus **VDF** in velocity space and how this **VDF** is covered by **PLASTIC's** **FoV** may be responsible for creating this effect. An illustration of the mechanism is provided in Fig. 22. The torus **VDF** is not an ideal structure, but it is smeared out in velocity space and has a non-zero width. Thus, depending on the **IMF** orientation more or less freshly injected torus **PUIs** are measured. This torus is superposed over a background of isotropic **PUIs** that have already scattered. Both, the torus **PUIs** and the isotropic **PUIs** have a characteristic shape. Now the interplay of these two shapes, or more precisely the fraction of **PUIs** from the initial torus **VDF** and the isotropic **PUIs**, affects the cutoff speed determined by any of our cutoff speed determination techniques. If more ions from the torus **VDF** are measured and therefore a

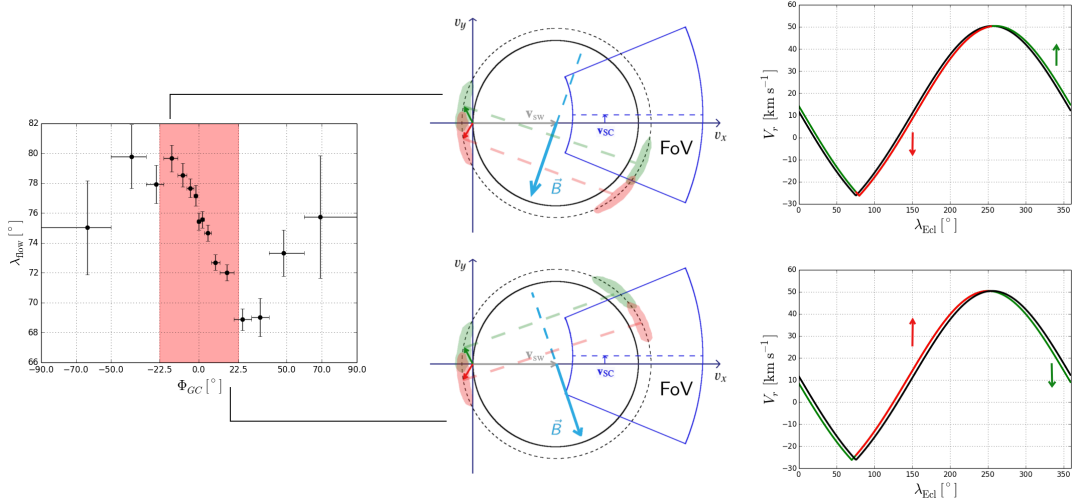


Figure 22: Illustration of an alternative mechanism that could lead to the observed shift of the λ_{flow} result with IMF orientation, which is not related to transport. The signature, which is commonly called the torus VDF, is smeared out and it has a non-zero angular width. Due to the tangential injection velocity, the location of the torus signature varies in location. Therefore, more or less PUIs from the torus VDF are sampled depending on ecliptic longitude. The ratio of measured torus VDF and isotropic background affects the determined cutoff speed. At ecliptic longitudes, where the tangential injection speed shifts the torus more inside of the FoV (for example the green torus signature in the top middle panel) a higher cutoff speed is determined and vice versa. This introduces an asymmetry in the cutoff speeds, which leads to a shift of the determined λ_{flow} .

pronounced torus signature is observed, the determined cutoff speed is increased and vice versa. Anyhow, if this would only be related to the IMF orientation with stochastically distributed variations depending on the solar wind conditions, no shift of the determined λ_{flow} would be expected. There has to be a systematic dependence on ecliptic longitude that introduces an asymmetry with respect to the real λ_{flow} . Here, the tangential velocity component of the interstellar neutrals, V_t , comes into play. The tangential velocity does not systematically influence the injection speed in the solar wind frame itself, but it has an impact on the location of the torus VDF in velocity space. For positive tangential velocities, the torus VDF is "lifted-up" in velocity space, for negative speeds it is "pushed-down" (see middle panels of Fig. 22). For example, at $\lambda \approx 135^\circ$ the neutral tangential velocity is negative and for $\lambda \approx 30^\circ$ this component is positive. This means, that for a given IMF orientation the FoV covers more or less PUIs from the torus VDF depending on ecliptic longitude. In one half of the orbit, the initial torus is systematically shifted out of the FoV and vice versa. This introduces an asymmetry of the determined cutoff speeds with respect to λ_{flow} , which could lead to the observed trend of determined λ_{flow} with Φ_{GC} .

The additional observational constraints presented in Sec. 5.3.1 can also be explained by this mechanism. An increased solar wind speed would weaken the effect, as the angular shift of the torus VDF in velocity space due to tangential injection speed is decreased with increasing solar wind speed. Furthermore, an increased pitch-angle scattering rate due to a variable IMF would broaden the torus

VDF. Then, a shift of the torus **VDF** in velocity space would have a decreased impact on the number of **PUIs** that fall into the **FoV**. This mechanism also explains the observation of a steeper trend with a restricted **FoV**. If the torus is located just at the edge of the **FoV** in velocity space, the largest shift of λ_{flow} is expected. Then the change of the tangential injection velocity has the largest impact on the number of **PUIs** from the torus that fall into the **FoV**. Assuming the ideal torus **VDF** created from neutrals at rest and neglecting the spacecraft eigen-velocity, the torus would be located just at the edge of the unrestricted **FoV** at an **IMF** orientation with $\Phi_{\text{GC}} = 22.5^\circ$. With a restricted **FoV**, this angle is decreased accordingly. Therefore a steeper signature of λ_{flow} as a function of Φ_{GC} is expected.

Two conditions must be fulfilled, so that this mechanism can create the observed asymmetry of the determined cutoff speeds:

1. The determined cutoff speed must depend on the strength of the observed torus **VDF** signature.
2. The tangential injection velocity must have a significant impact on the orientation of the torus **VDF** in velocity space.

To investigate the first condition, we consider data collected in the crescent range of ecliptic longitude, 230° to 280° . From previous determinations of λ_{flow} , we estimate the crescent location to be $\lambda_{\text{cr.}} \approx 255^\circ$ (Wood et al., 2015; Schwadron et al., 2015). The main reason, why we choose this range in ecliptic longitude is, that in this range a very small variation of the cutoff speed ($\Delta V_r < 5 \text{ km s}^{-1}$) with ecliptic longitude is expected (see e.g. left panel of Fig. 24). Therefore, we can test how the orientation of the torus **VDF** that is defined by the **IMF** orientation affects the determined cutoff speed. The results are displayed in Fig. 23. On the left hand side, the **IMF** orientation has been restricted to orientations close to the ecliptic plane and the Φ_{GC} angle has been varied. A systematic trend of the determined cutoff speed with **IMF** orientation is found, that is asymmetric with respect to $\Phi_{\text{GC}} = 0^\circ$. On

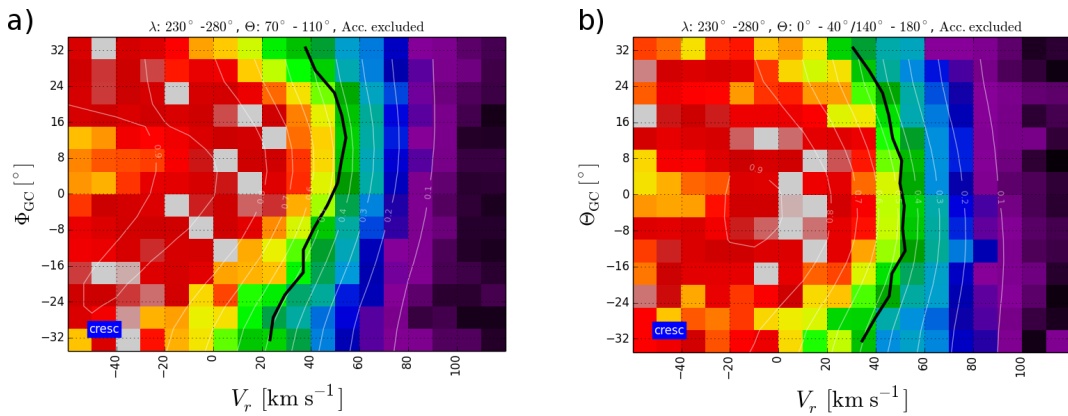


Figure 23: 2D He^+ count histograms as a function of V_r and the **IMF** orientation. The counts have been normalized to the maximum counts in each bin of **IMF** orientation. The ecliptic longitude has been restricted to $230^\circ < \lambda < 280^\circ$ and acceleration sites have been excluded from the data for both figures. The solid black line shows the cutoff speed in each **IMF** orientation bin determined from a tanh-fit of the histogram. a) Here, **IMF** orientation lying approximately within the ecliptic plane are chosen and the variation of Φ_{GC} is considered. Thus, the torus is running through the aperture in azimuthal direction (see also Fig. 20). b) **IMF** orientations approximately normal to the ecliptic plane are chosen and the variation of Θ_{GC} is considered. The torus is running through the aperture in latitudinal direction.

the one hand, this is due to the spacecraft eigen-velocity of $v_{SC} \approx 30 \text{ km s}^{-1}$ which shifts the FoV in velocity space (see e.g. middle panels of Fig. 21 and 22). On the other hand, this is due to the sensor's detection efficiency, which is a function of incident angle. The position bins and their coverage in velocity space are illustrated in Fig. 20 and an estimate for the position bin efficiency is given in Sec. 5.3.3 and Fig. 25. Somehow, the position bins around bin ~ 12 show an increased efficiency. Furthermore, also selection effects may play a role in the creation of this structure. IMF orientation with $\Phi_{GC} < 0^\circ$ preferentially occur in rarefaction regions, where an enhanced cooling of the PUI VDF is expected that could lead to a decreased cutoff speed. On the right hand side of Fig. 23, the IMF has been restricted to angles that are approximately normal to the ecliptic plane and the cutoff has been considered as a function of Θ_{GC} . Here, a symmetric decrease of the determined cutoff speed is observed. The advantage of this configuration is that the detection efficiency in latitudinal direction is anticipated to be symmetric and that no selection effects are expected to occur. Anyhow, both figures indicate that the determined cutoff speed is related to the ambient IMF orientation. Therefore, the abundance of measured PUIs from the torus VDF is very likely to have an effect on the determined cutoff speeds.

For the investigation of the second condition, we consider ranges of ecliptic longitude, in which a high tangential velocity of the interstellar neutrals is expected: 100° to 200° for negative V_t , 310° to 360° and 0° to 50° for positive V_t . In these ranges, the orientation of the PUI torus VDF in velocity space is studied. For this task, an analysis concept developed by Drews et al. (2015) is utilized. As already mentioned, PLASTIC has the ability to measure 3D VDFs, because of its position sensitive detection system. However, in particular the efficiency in azimuthal direction is not sufficiently known to derive these VDFs in a straight-forward way. Nevertheless, in Drews et al. (2015) a method has been developed to derive differences of the 2D PUI VDF as a function of IMF orientation. With the help of this method, one can compare the 2D VDF under various IMF orientations.

In the two top panels of Fig. 24 the results of this analysis for the two ranges of ecliptic longitude and various IMF orientations are shown. The displayed color code is a probability density that indicates how many PUIs were measured in the given velocity space volume compared to other IMF orientations. One can see that the main increase in probability density due to the initial torus VDF is shifted with respect to the expected position according to the considered tangential injection speeds. In other words: for negative tangential injection speeds, the torus VDF is located below the expected location in velocity space, for positive speeds above the expected location. In the bottom panel of Fig. 24, the difference between the two signs in tangential injection speed is directly shown as a 1D representation of the plots above. For this plot, only the speed range, in which the torus is expected ($-30 \text{ km s}^{-1} < V_r < 60 \text{ km s}^{-1}$) is taken into account, and the probability density is shown as a function of incident angle in the solar wind frame, β . To guide the eye, a 3-bin running average has been calculated. The torus signature is clearly shifted with respect to each other according to the tangential injection speed. This shows, that this velocity component has a significant impact on the location of the torus VDF in velocity space.

With both conditions fulfilled, this strongly indicates that the latter mechanism is the main driver of the observed trend of the determined λ_{flow} as a function of Φ_{GC} .

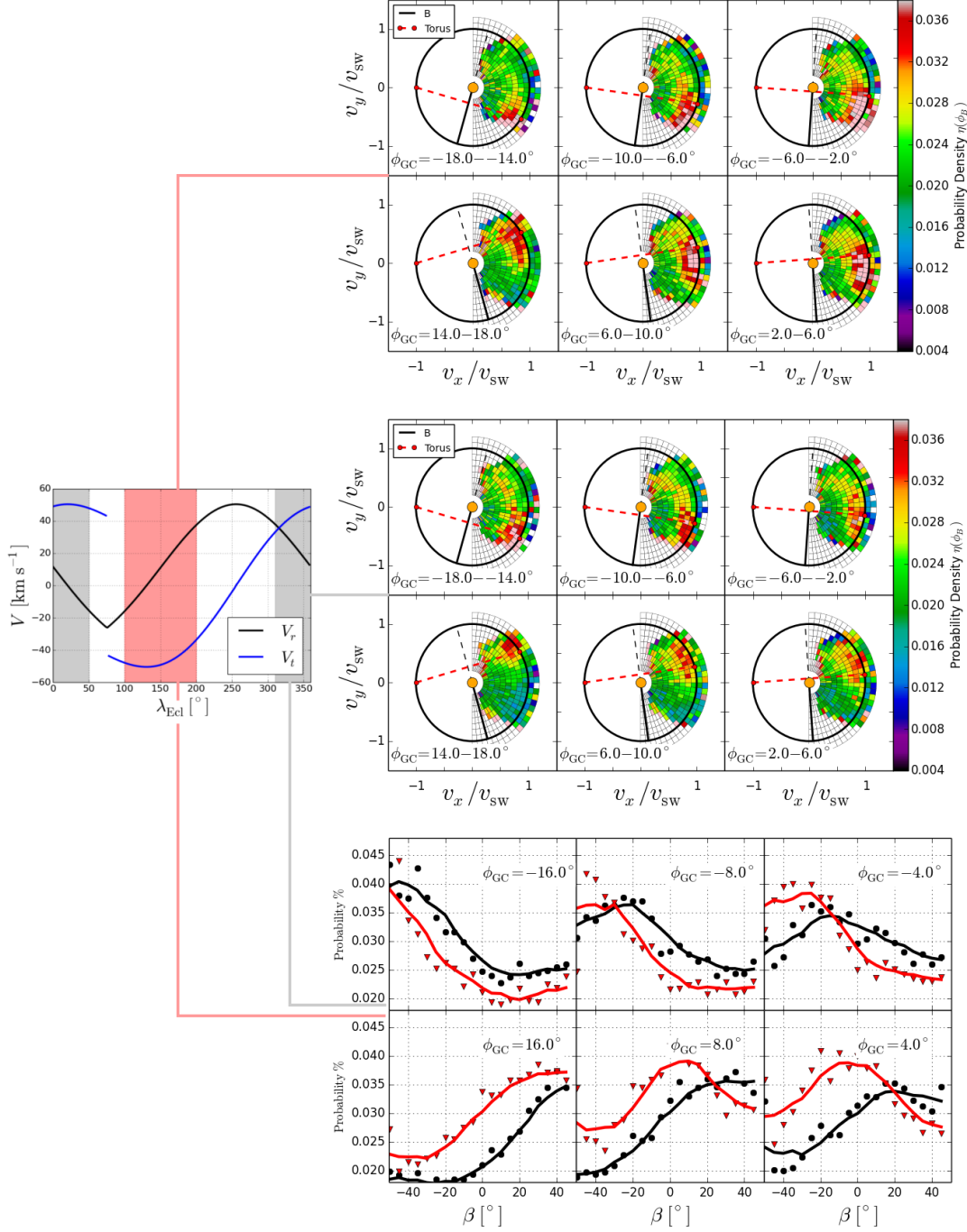


Figure 24: Measurements of the location of the torus VDF signature in velocity space. The panel on the left-hand side, shows the theoretical radial and tangential velocities of neutral helium at the orbit of STA as a function of ecliptic longitude calculated from Eqn. 5 of Taut et al. (2018) ($\lambda_{\text{flow}} = 75^\circ$, $v_{\text{ISN},\infty} = 26.2 \text{ km s}^{-1}$). The top two panels show the results for the 2D He^+ probability density in velocity space for different IMF orientations from the analysis developed by Drews et al. (2015). The red dashed line depicts the expected orientation of the torus VDF of freshly injected PUIs. The bottom panel shows a 1D projection of the panels above for the speed range $-30 \text{ km s}^{-1} < V_r < 60 \text{ km s}^{-1}$ plotted as a function of β , the azimuthal incident angle in the solar wind frame. The red and black curve correspond to the ranges of ecliptic longitude marked in the figure on the left-hand side.

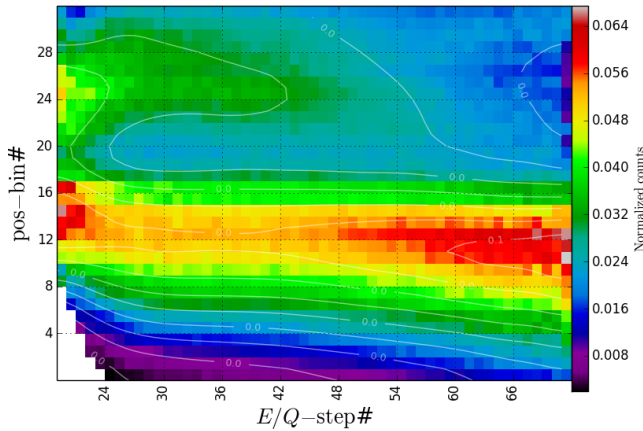


Figure 25: 2D count histogram of He^+ in parallel IMF orientations ($|\Phi_{\text{GCL}}| > 50^\circ$) as a function of E/Q step and position bin. Furthermore accelerated He^+ has been excluded $V_r < 60 \text{ km s}^{-1}$ and solar wind background is suppressed.

5.3.3 Improved Result for λ_{flow}

With an improved understanding of the mechanism creating the effect discussed in the previous section, we aim to obtain a result for λ_{flow} that is not influenced by this systematic error anymore. Apparently, the location of the torus VDF in velocity space is crucial for the determined cutoff speeds and this location is always affected by the tangential injection speed.

One challenge in this task poses the unknown position bin efficiency that needs to be considered. As we assume that the systematic motion of the torus VDF signature inside the FoV creates the systematic error that has been addressed in the previous section, knowledge about the position bin efficiency is required to correct for this effect. To estimate the position bin efficiency from in-flight data, we assume that at IMF orientations with $|\Phi_{\text{GCL}}| > 50^\circ$ only the isotropic part of the He^+ PUI VDF is sampled. As observed in Taut et al. (2016), accelerated PUIs preferentially stream along the field lines and, thus, introduce an anisotropy at these angles. We aim to minimize this effect by requiring $V_r < 60 \text{ km s}^{-1}$. Furthermore, we expect the position bin efficiency to depend on the incident ion's energy. Therefore, we consider the position bin efficiency of He^+ as a function of PLASTIC's E/Q steps. If we assume that the VDF that is measured by PLASTIC is isotropic, the observed count rates of every position bin at a given E/Q step are expected to be equal. Hence, we can estimate the relative position bin efficiency by considering a 2D He^+ count histogram of the data described above as a function of E/Q step and position bin normalized to the sum of all counts in each E/Q step. This is shown in Fig. 25. For each count measured at a given E/Q step and position bin, the inverse of the corresponding histogram value is taken as weighting, which serves as the position bin efficiency correction. This is, however, likely to be an oversimplified approach. The main assumption that at these IMF orientations only an isotropic VDF is sampled is not necessarily true. In Drews et al. (2015) also signatures of decelerated PUIs streaming along the IMF were observed, which contradict our assumption. A more sophisticated approach to correct for the position bin efficiency would involve comparing data before and after July 2015, where the STA spacecraft was flipped. This means that also the azimuthal position bins are mirrored from which a more realistic estimate of the position bin efficiency could be derived.

Another issue that needs to be considered for correcting this effect is the determination of the expected torus position in velocity space from the **IMF** orientation. The angles Φ_{GC} and Θ_{GC} utilized on Taut et al. (2018) denote the orientation of the torus with respect to the radial direction. But **STA** moves with a tangential speed of $v_{\text{STA}} \approx 30 \text{ km s}^{-1}$, which means that for $\Phi_{\text{GC}} = 0^\circ$ the torus is not located in the center of the **FoV** (see e.g. Fig. 20). As there is only a shift of the **FoV** in tangential direction, the angle Θ_{GC} is not affected. However, knowing the spacecraft and the solar wind speed, we can calculate Φ'_{GC} which denotes the location of the ideal torus with respect to the spacecraft's eigen-velocity. One problem that arises from this correction is, that it is only valid for **IMF** orientations that lie approximately in the ecliptic plane. In **IMF** orientations that are approximately normal to the ecliptic plane the torus **VDF** itself lies in the ecliptic plane and therefore covers every position bin even with every possible injection speed. These orientations correspond to $\Phi_{\text{GC}} \approx 0^\circ$. Nevertheless, considering the spacecraft velocity for these configurations $\Phi'_{\text{GC}} < 0^\circ$ is obtained. Although these **IMF** orientations occur rarely as the average **IMF** lies inside the ecliptic plane, they may contribute substantially to the outcome of the cutoff analysis. Therefore, **IMF** orientation approximately inside and normal to the ecliptic plane are considered separately in the following. One can easily distinguish between these **IMF** orientations by considering the Θ angle of the **IMF** which is the angle with respect to the normal direction. Consequently, the data set, preprocessed for **IMF** orientations in which the torus falls into the **FoV** and excluding acceleration sites according to Taut et al. (2018), is divided into two subsets with the conditions displayed in Tab. 4.

Table 4: Conditions of the **IMF** angle Θ with respect to the normal direction to divide the utilized data set into two basic orientations. In the *ecliptic* case, the **IMF** lies approximately inside the ecliptic plane and the torus **VDF** intersects with this plane at two locations. In the *normal* case, the **IMF** is normal to the ecliptic plane and the torus **VDF** lies inside the ecliptic plane therefore covering all azimuthal position bins.

Subset	Condition
<i>ecliptic</i>	$60^\circ < \Theta < 120^\circ$
<i>normal</i>	$\Theta < 20^\circ \wedge 160^\circ < \Theta$

If we expect the torus in the center of **PLASTIC**'s **FoV** considering the *ecliptic* **IMF** orientations ($\Phi'_{\text{GC}} = 0^\circ$), we expect the shift of the torus location due to the variation in injection speed to cancel out assuming a symmetric torus structure. Then for positive tangential injection velocities the torus is moved outside of the aperture in the same way as for negative injection velocities. Furthermore, we can additionally utilize the *normal* data set to obtain λ_{flow} as we do not expect any systematic influence of the injection speed in these **IMF** orientations. We developed two approaches to determine an unbiased value of λ_{flow} .

In the first approach, we utilize both data subsets, *ecliptic* and *normal*. Furthermore, the *ecliptic* data is filtered for a Φ'_{GC} range symmetric about $\Phi'_{\text{GC}} = 0^\circ$. The problem with setting such a restriction is that **IMF** orientations close to the Parker orientation are more frequently observed than other orientations, which would systematically shift the result for λ_{flow} to decreased values. Therefore, a Monte-Carlo technique has been utilized to choose time periods in such a fashion that every

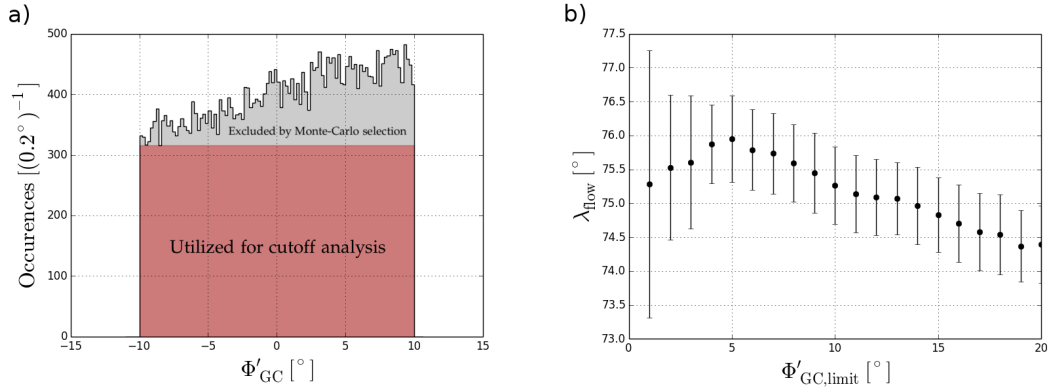


Figure 26: a) Example of IMF orientation occurrences as a function of Φ'_{GC} in the range $-10^\circ < \Phi'_{\text{GC}} < 10^\circ$ for IMF fulfilling the *ecliptic* condition (see Tab. 4). For the λ_{flow} determination, it is required that every Φ'_{GC} value occurs equally often. To ensure this, time periods are excluded randomly from the data set. b) λ_{flow} result as a function of width in the Φ'_{GC} range. $\Phi'_{\text{GC},\text{limit}} = 1^\circ$ corresponds to the range $-1^\circ < \Phi'_{\text{GC}} < 1^\circ$ and so on.

Φ'_{GC} value (rounded to a precision of 0.2°) for IMFs inside the ecliptic plane occurs equally often. An example for this is displayed in Fig. 26 a. By repeating this random selection, also an error estimate for the systematic influence of the Φ'_{GC} values is obtained. Furthermore, the stochastic errors are also calculated according to the method described in Taut et al. (2018). The results for λ_{flow} including the combined stochastic error and the error due to the Φ'_{GC} angle selection for increasing Φ'_{GC} ranges are displayed in Fig. 26 b.

On the one hand, in an increasing range for Φ'_{GC} a systematic trend to decreasing λ_{flow} values is observed. This is due to the selection effect which has already been mentioned in Sec. 5.3.2. In the range $\Phi'_{\text{GC}} < 0^\circ$ on average lower cutoff speeds are determined due to these angles occurring more frequently in rarefaction regions, where the PUIs appear to be decelerated more efficiently. This means that in a large Φ'_{GC} range around 0° the angles with $\Phi'_{\text{GC}} > 0^\circ$ dominate, because when two cutoff spectra are superposed our cutoff speed determination techniques are only sensitive to the higher cutoff speed. This leads to a decrease of the λ_{flow} result. On the other hand, the stochastic error is of course larger in small Φ'_{GC} ranges due to low statistics. A compromise between the stochastic error due to statistics and the systematic error due to the Φ'_{GC} range needs to be found. Hence, we choose the $-4^\circ < \Phi'_{\text{GC}} < 4^\circ$ range. Beyond this range the systematic trend to decreased λ_{flow} results seems to start and the stochastic error is comparatively small. The result obtained by this is: $\lambda_{\text{flow}} = (75.79 \pm 0.59)^\circ$.

The second approach to determine λ_{flow} is a fit of the curve of the determined λ_{flow} results as a function of Φ'_{GC} . For this we consider the *ecliptic* data set and sort this data into 16 ranges between -45° and $+45^\circ$. For the central range, $-2^\circ < \Phi'_{\text{GC}} < 2^\circ$, we also add the *normal* data. The resulting curve is fit with a third-order polynomial and a $1-\sigma$ confidence interval is calculated. In Fig. 27 the results are displayed.

The interception of the fitted polynomial with $\Phi'_{\text{GC}} = 0^\circ$ corresponds to the λ_{flow} result. In this case we find: $\lambda_{\text{flow}} = (75.60 \pm 0.40)^\circ$. However, for this approach we

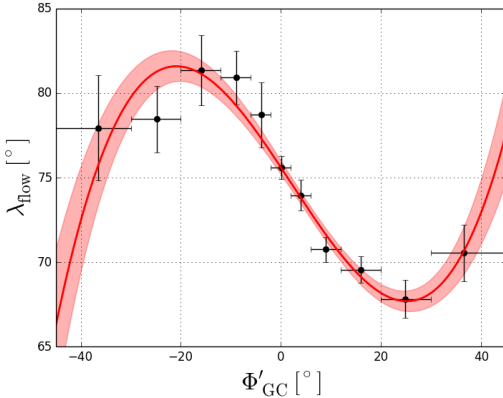


Figure 27: Results for λ_{flow} as a function of Φ'_{GC} . A third order polynomial is fit to the data and the $1-\sigma$ confidence interval is calculated.

made the implicit assumption that the determined λ_{flow} follows a smooth curve as a function of Φ'_{GC} , which is not necessarily justified. As already mentioned, the occurrence of certain IMF orientations can be related to special solar wind conditions that have influence on the general shape of the He⁺ PUI VDF. It is well possible, that this has an influence on the impact of the systematic error due to the tangential injection velocity. This in turn means that the individual data points displayed in Fig. 27 may not follow a smooth curve. Therefore, this approach needs to be investigated in more detail and, consequently, the obtained value for λ_{flow} and especially its error constitute only a preliminary result that needs to be reviewed more thoroughly.

In Tab. 5 the results obtained in this section are compared to former results derived from direct neutral particle measurements. Both values for λ_{flow} that have been obtained in this section are in good agreement with the values obtained from IBEX observations. They also agree well with recent results obtained from a neutral particle detector onboard the Ulysses spacecraft. The error bars of the result presented by Wood et al. (2015) appear to be underestimated as Bzowski et al. (2014) utilized the same data set for their analysis and yield errors about one order of magnitude larger. However, as can be seen from the different errors, the determination of λ_{flow} from PUI measurements in its current stage does not necessarily provide a substantially more precise method than direct neutral particle measurements.

Table 5: Compilation of selected results for λ_{flow} for comparison with the results obtained in this work utilizing PUIs. All other results were obtained from direct neutral particle measurements by detectors on the IBEX and Ulysses spacecraft.

Work	Spacecraft	λ_{flow} result [°]
This work - symmetric Φ'_{GC} range	STA	75.79 ± 0.59
This work - Φ'_{GC} fit (preliminary)	STA	75.60 ± 0.40
Schwadron et al. (2015)	IBEX	75.6 ± 1.4
Bzowski et al. (2015)	IBEX	75.8 ± 0.5
Bzowski et al. (2014)	Ulysses	$75.3 + 1.1(-1.2)$
Wood et al. (2015)	Ulysses	75.54 ± 0.19

Additionally, there are further systematic influences that may affect the result obtained by both approaches related to the PUI cutoff. For example, if we assume that the cutoff speed varies as a function of present PUIs from the torus VDF, then the cutoff speed is also influenced by the ambient ionization rate. If the ionization rate is increased, for example by an increased extreme ultra-violet radiation flux which is crucial for the photo-ionization rate, then more PUIs are created locally near the spacecraft. Indeed, the extreme ultra-violet radiation flux is increased in solar maximum compared to solar minimum which could introduce a systematic effect on the λ_{flow} determination. This effect is likely to be very small, but its impact needs to be quantified. Furthermore, both approaches presented in this section can only obtain a valid result for λ_{flow} if the torus VDF structure is itself symmetric. In [Drews et al. \(2015\)](#) observations are reported that show an asymmetric torus signature and it is argued that this stems from the fact, that more PUIs are injected at IMF orientations near the Parker angle. However, in Fig. 24 no such signatures showing a clear asymmetry are observed.

CONCLUSIONS & OUTLOOK

In this thesis, unresolved issues regarding the two global PUIs populations in the heliosphere have been investigated. Here, our findings are summarized and evaluated in the context of current research. Additionally, an outlook regarding future research is provided.

The three main questions that have been aimed to answer are introduced in Sec. 1.1. These questions are now addressed again:

1) What is the nature of the inner source for PUIs?

With the help of CTOF data, the composition of inner-source heavy PUIs has been investigated in Taut et al. (2015). The observed composition has been compared to the modeled composition from the solar wind neutralization scenario (Wimmer-Schweingruber and Bochsler, 2003). All deviations within the composition could be explained qualitatively. Furthermore, a significant trend of the inner-source O⁺/C⁺ abundance ratio as a function of solar wind speed was found. This trend was not expected and it poses a significant, additional restriction for inner-source PUIs production scenarios.

Together with the observation of an O⁶⁺-O⁺ flux correlation presented in Berger et al. (2015) and the observation of locally produced C⁺ ions in Drews et al. (2016), our work provided a significant extension of observational constraints for the inner-source PUIs production. A summarizing compilation of the observed properties of inner-source PUIs and their compatibility with the proposed inner-source PUIs production scenarios is provided in Tab. 3. This table is based on the compilation by Allegrini et al. (2005), but extended and updated for the new observations and the proposed production scenario by Schwadron and McComas (2010), who argued that energetic neutrals could also be responsible for the production of inner-source PUIs. As can be seen from the updated compilation in Tab. 3, especially the solar wind speed dependent composition and the O⁶⁺-O⁺ flux correlation exclude almost all proposed production scenarios as the main origin of inner-source PUIs. This leaves the solar wind neutralization scenario as the most likely candidate for the inner-source PUIs production.

However, there are still open questions connected to the observational constraints and their implications for the inner-source PUIs production. For example, the contamination of the inner-source O⁺ count rate by the interstellar component needs to be quantified. It might be possible, that due to higher solar wind speeds the charge-exchange ionization rate of oxygen decreases (Lindsay and Stebbings, 2005). This would have the consequence that interstellar oxygen atoms are ionized closer to the Sun, which means that they have more time to cool. This could significantly contaminate the measured inner-source O⁺ count rate, which could also explain the solar wind speed dependent inner-source O⁺/C⁺ abundance ratio. It is unlikely, that this effect is able to produce a factor of two in this abundance ratio, but nevertheless it is desirable to quantify its impact. This could be performed with the help of the EMMREM simulation code. In this thesis, we compared preliminary

results for the simulated C⁺ and O⁺ VDF to measured VDFs derived from CTOF data. Anyhow, this is an ongoing investigation and the final results will be published in Quinn et al. (2018) in the near future. Hopefully, these simulations will help to better understand the observed properties of inner-source PUIs with respect to the proposed production scenarios. However, the not well known properties of interplanetary dust grains pose a limit for the accuracy of such simulations of the inner-source PUIs production. In turn, this means once a dominant inner-source PUI production mechanism is identified, inner-source PUIs could serve as a diagnostic tool to derive the geometry and composition of the dust population in the inner heliosphere.

2) *What is the 3D VDF of PUIs at 1 AU and what are the implication for the stability of a torus VDF within the dynamic solar wind?*

We were able to contribute substantially to the progress of understanding the 3D VDF of PUIs. Historically, it had been assumed that the highly anisotropic initial PUIs VDF is almost instantaneously transformed into an isotropic distribution (Vasyliunas and Siscoe, 1976). The instability of such a VDF in the solar wind plasma with respect to the generation of waves was believed to lead to this rapid isotropization. Next to this process, fluctuations within the IMF also lead to pitch-angle scattering. However, first of all Möbius et al. (1998) measured differences in the VDF depending on the IMF orientation, which was assigned to an incomplete isotropization only in one hemisphere of velocity space (Isenberg, 1997). Then this picture was revised again by measurements of a torus VDF signature of He⁺ in Oka et al. (2002), which was subsequently confirmed by Drews et al. (2013) and Gershman et al. (2014). In Taut et al. (2016), we complemented on these findings with the observation of a clear torus-related signature within the He⁺ VDF observed by CTOF. This contradicts the theory of a rapid isotropization and also poses challenges for the cooling mechanism of PUIs. Furthermore an additional anisotropy concerning PUIs that must have undergone an acceleration mechanism has been observed. Accelerated PUIs seem to preferentially stream along the IMF lines, which means that the acceleration mechanisms must be more efficient along the field.

Also the findings presented in Chapter 5 are closely connected to the 3D PUI VDF. We were able to show, that not only the IMF orientation, but also the injection velocity substantially affects the location of the torus VDF in velocity space. The consequence of this is, that the result for λ_{flow} determined from the PUI cutoff speeds is shifted according to the selected IMF orientations. The fact that this effect is less pronounced in faster solar wind and more variable IMF orientations implies that in these solar wind conditions a more isotropic PUI VDF is observed. This means that not the instability of the anisotropic VDF is the main driver of the isotropization, but that it is more likely that wave activity inside the solar wind and fluctuations of the IMF lead to a gradually more isotropic VDF.

We are just beginning to understand the evolution of the PUI torus VDF and the anisotropy connected to it. It is planned to investigate the anisotropy of the PUI VDF with respect to wave activity, that can be derived from high resolution IMF data. Such studies could also be performed with respect to PUIs in SIRs. SIRs are in particular interesting, because of the compression that may affect the cooling of the distribution and the acceleration happening in the turbulent compressed fast wind.

3) How can we utilize the PUIs VDF to find the interstellar neutral flow longitude?

We have revisited the approach to determine the interstellar flow longitude, λ_{flow} , from measurements of the He⁺ VDF provided by PLASTIC presented in Möbius et al. (2015). We have been able to substantially improve this method, which can be seen at the significantly higher mirror-correlation coefficients presented in Taut et al. (2018) compared to the ones reached in Möbius et al. (2015). In general, our improvements involved the exclusion of sources for systematic errors that we implemented into the method. However, utilizing the enhanced data quality provided by our improvements, we were able to uncover another fundamental systematic influence on the result for λ_{flow} that is connected to the mix of measured IMF orientations. As the PUI VDF is closely connected to the ambient IMF orientation, it is apparent that this systematic influence might be connected to the PUI VDF. In Taut et al. (2018) it is surmized that again longitudinal transport could be capable to create these observations.

Within this thesis, we could show that this is most likely not the case. Our observations indicate that the observed trend of the determined λ_{flow} is more likely due to PLASTIC's limited FoV and the location of the torus VDF in velocity space. As shown in Fig. 24 the location of the torus depends on ecliptic longitude due to the tangential injection velocity. This introduces an asymmetry of the determined cutoff speeds, which leads to the observed shift of λ_{flow} . Having identified and understood this additional source for systematic errors, we are aiming to provide an improved value for λ_{flow} . For this several corrections had to be performed. Finally, our new estimate for λ_{flow} from PUI measurements reads: $\lambda_{\text{flow}} = (75.79 \pm 0.59)^\circ$.

However, there is still room for improvements in this method. The correction of the azimuthal position bin efficiency has been performed assuming the observation of an isotropic PUI VDF, if the torus does not fall into the FoV, which is likely to be oversimplified. Therefore, a more elaborate correction should be developed. The fact that the STA spacecraft has been flipped in July 2015, which means that also the position bins are mirrored since that day, could help to derive such a correction. Furthermore, the influence of solar cycle variations needs to be quantified. Another uncertain point is again the PUI VDF itself. Our correction for the found systematic error due to the IMF orientation works only, if the torus VDF is a symmetric structure. As the Parker angle is the most frequently observed IMF orientation, the torus VDF could be asymmetrically smeared out. Drews et al. (2015) reported on signatures implying this. Anyhow, in our observations presented in Fig. 24 no such feature can be seen. Finally, we have to admit that we do not yet understand the PUI VDF in sufficient detail to provide a precision measurement of λ_{flow} from PUI observations.

As shown, PUIs can serve as diagnostic tools in many ways, but the evaluation of PUI measurements is often complex and challenging. The inner-source PUIs provide potential information about how the solar wind interacts with interplanetary dust grains. The evolution of the PUI VDF serves as a tool to understand scattering, cooling, and acceleration processes in the solar wind plasma and interstellar PUIs carry information about the LISM. All this information is relevant for the understanding of the heliosphere on a global scale.

BIBLIOGRAPHY

- Acuña, M. H., D. Curtis, J. L. Scheifele, C. T. Russell, P. Schroeder, A. Szabo, and J. G. Luhmann. The STEREO/IMPACT magnetic field experiment. *Space Science Reviews*, 136:203–226, 2008.
- Aellig, M. R., H. Grünwaldt, P. Bochsler, P. Wurz, S. Hefti, R. Kallenbach, F. M. Ipavich, W. I. Axford, H. Balsiger, A. Bürgi, et al. Iron freeze-in temperatures measured by SOHO/CELIAS/CTOF. *Journal of Geophysical Research: Space Physics*, 103(A8):17215–17222, 1998.
- Alfvén, H.: Existence of electromagnetic-hydrodynamic waves. *Nature*, 150(3805): 405–406, 1942.
- Allegrini, F., N. A. Schwadron, D. J. McComas, G. Gloeckler, and J. Geiss. Stability of the inner source pickup ions over the solar cycle. *Journal of Geophysical Research: Space Physics*, 110(A5), 2005.
- Allegrini, F., R. W. Ebert, S. A. Fuselier, G. Nicolaou, P. Bedworth, S. Sinton, and K. J. Trattner. Charge state of 1 to 50 keV ions after passing through graphene and ultrathin carbon foils. *Optical Engineering*, 53(2):024101–024101, 2014.
- Anders, E. and N. Grevesse. Abundances of the elements: Meteoritic and solar. *Geochimica et Cosmochimica acta*, 53(1):197–214, 1989.
- Aschwanden, M.: *Physics of the solar corona: an introduction with problems and solutions*. Springer Science & Business Media, 2006.
- Bame, S. J., J. R. Asbridge, W. C. Feldman, and J. T. Gosling. Evidence for a structure-free state at high solar wind speeds. *Journal of Geophysical Research*, 82(10):1487–1492, 1977.
- Berger, L., R. F. Wimmer-Schweingruber, and G. Gloeckler. Systematic measurements of ion-proton differential streaming in the solar wind. *Physical review letters*, 106(15):151103, 2011.
- Berger, L., C. Drews, A. Taut, and R. F. Wimmer-Schweingruber. Short-term variability of inner-source pickup ions at 1 AU-SOHO/CELIAS observations. *Astronomy & Astrophysics*, 576:A54, 2015.
- Bertaux, J. L. and J. E. Blamont. Evidence for a source of an extraterrestrial hydrogen Lyman-alpha emission. *Astronomy and Astrophysics*, 11:200, 1971.
- Bochsler, P.: Minor ions in the solar wind. *The Astronomy and Astrophysics Review*, 14(1):1–40, 2007.
- Bochsler, P. and E. Möbius. Energetic neutral atoms: an additional source for heliospheric pickup ions. *The Astrophysical Journal Letters*, 721(1):L6, 2010.

- Bochsler, P. and P. Murdin. Solar wind composition. *Encyclopedia of Astronomy and Astrophysics*, page 2303, 2000.
- Bockelée-Morvan, D.: An overview of comet composition. *Proceedings of the International Astronomical Union*, 7(S280):261–274, 2011.
- Bzowski, M., J. M. Sokół, M. A. Kubiak, and H. Kucharek. Modulation of neutral interstellar He, Ne, O in the heliosphere. survival probabilities and abundances at IBEX. *Astronomy & Astrophysics*, 557:A50, 2013.
- Bzowski, M., M. A. Kubiak, M. Hłond, J. M. Sokół, M. Banaszkiewicz, and M. Witte. Neutral interstellar He parameters in front of the heliosphere 1994–2007. *Astronomy & Astrophysics*, 569:A8, 2014.
- Bzowski, M., P. Swaczyna, M. A. Kubiak, J. M. Sokół, S. A. Fuselier, A. Galli, D. Heirtzler, H. Kucharek, T. W. Leonard, D. J. McComas, et al. Interstellar neutral helium in the heliosphere from IBEX observations. iii. mach number of the flow, velocity vector, and temperature from the first six years of measurements. *The Astrophysical Journal Supplement Series*, 220(2):28, 2015.
- Bzowski, M. and M. Królikowska. Sungrazing comets as source of pickup ions at earth orbit and ulysses. *arXiv preprint astro-ph/0507065*, 2005.
- Cane, H. V. and I. G. Richardson. Interplanetary coronal mass ejections in the near-earth solar wind during 1996–2002. *Journal of Geophysical Research: Space Physics*, 108(A4), 2003.
- Chalov, S. V. and H. J. Fahr. Signatures of the interplanetary helium cone reflected by pick-up ions. *Solar Physics*, 187(1):123–144, 1999.
- Chen, J. H., N. A. Schwadron, E. Möbius, and M. Gorby. Modeling interstellar pickup ion distributions in corotating interaction regions inside 1 AU. *Journal of Geophysical Research: Space Physics*, 120(11):9269–9280, 2015.
- Chen, J. H., E. Möbius, G. Gloeckler, P. Bochsler, M. Bzowski, P. A. Isenberg, and J. M. Sokół. Observational study of the cooling behavior of interstellar helium pickup ions in the inner heliosphere. *Journal of Geophysical Research: Space Physics*, 118(7):3946–3953, 2013.
- Chen, P. F.: Coronal mass ejections: models and their observational basis. *Living Reviews in Solar Physics*, 8(1):1, 2011.
- Cranmer, S. R.: Self-consistent models of the solar wind. *Space science reviews*, 172(1):145–156, 2012.
- Dialynas, K., S. M. Krimigis, D. G. Mitchell, R. B. Decker, and E. C. Roelof. The bubble-like shape of the heliosphere observed by Voyager and Cassini. *Nature Astronomy*, 1, 2017.
- Dresing, N., R. Gómez-Herrero, B. Heber, A. Klassen, O. Malandraki, W. Dröge, and Y. Kartavykh. Statistical survey of widely spread out solar electron events observed with STEREO and ACE with special attention to anisotropies. *Astronomy & Astrophysics*, 567:A27, 2014.

- Drews, C., L. Berger, A. Taut, T. Peleikis, and R. F. Wimmer-Schweingruber. 2D He⁺ pickup ion velocity distribution functions: STEREO PLASTIC observations. *Astronomy & Astrophysics*, 575:A97, 2015.
- Drews, C.: Flux of suprathermal ions measured by STEREO PLASTIC: Pick-up ions at 1 AU, 2009.
- Drews, C.: *Interstellar Pickup Ions at 1 AU with STEREO/PLASTIC*. PhD thesis, Christian-Albrechts Universität Kiel, 2013.
- Drews, C., L. Berger, R. F. Wimmer-Schweingruber, A. B. Galvin, B. Klecker, and E. Möbius. Observations of interstellar neon in the helium focusing cone. *Journal of Geophysical Research: Space Physics*, 115(A10), 2010.
- Drews, C., L. Berger, R. F. Wimmer-Schweingruber, P. Bochsler, A. B. Galvin, B. Klecker, and E. Möbius. Inflow direction of interstellar neutrals deduced from pickup ion measurements at 1 AU. *Journal of Geophysical Research: Space Physics*, 117(A9), 2012.
- Drews, C., L. Berger, R. F. Wimmer-Schweingruber, and A. B. Galvin. Interstellar He⁺ ring-beam distributions: Observations and implications. *Geophysical Research Letters*, 40(8):1468–1473, 2013.
- Drews, C., L. Berger, A. Taut, and R. F. Wimmer-Schweingruber. Anisotropy of the He⁺, C⁺, N⁺, O⁺, and Ne⁺ pickup ion velocity distribution functions. *Astronomy & Astrophysics*, 588:A12, 2016.
- Ebert, R. W., D. J. McComas, H. A. Elliott, R. J. Forsyth, and J. T. Gosling. Bulk properties of the slow and fast solar wind and interplanetary coronal mass ejections measured by Ulysses: Three polar orbits of observations. *Journal of Geophysical Research: Space Physics*, 114(A1), 2009.
- Fahr, H. J.: On the influence of neutral interstellar matter on the upper atmosphere. *Astrophysics and Space Science*, 2(4):474–495, 1968.
- Fahr, H. J.: Revisiting the theory of the evolution of pick-up ion distributions: magnetic or adiabatic cooling? In *Annales Geophysicae*, volume 25, pages 2649–2659, 2008.
- Fisk, L. A. and G. Gloeckler. Acceleration and composition of solar wind suprathermal tails. *Space Science Reviews*, 130(1):153–160, 2007.
- Fisk, L. A. and G. Gloeckler. Particle acceleration in the heliosphere: implications for astrophysics. *Space science reviews*, 173(1-4):433–458, 2012.
- Fisk, L. A. and M. A. Lee. Shock acceleration of energetic particles in corotating interaction regions in the solar wind. *The Astrophysical Journal*, 237:620–626, 1980.
- Fleck, B.: The SOHO mission. *Coronal Magnetic Energy Releases*, pages 233–244, 1995.
- Florinski, V., G. P. Zank, J. Heerikhuisen, Q. Hu, and I. Khazanov. Stability of a pickup ion ring-beam population in the outer heliosheath: Implications for the IBEX ribbon. *The Astrophysical Journal*, 719(2):1097, 2010.

- Forsyth, R. J., A. Balogh, E. J. Smith, G. Erdős, and D. J. McComas. The underlying parker spiral structure in the Ulysses magnetic field observations, 1990–1994. *Journal of Geophysical Research: Space Physics*, 101(A1):395–403, 1996.
- Frisch, P. C., S. Redfield, and J. D. Slavin. The interstellar medium surrounding the Sun. *Annual Review of Astronomy and Astrophysics*, 49:237–279, 2011.
- Galli, A., P. Wurz, N. A. Schwadron, H. Kucharek, E. Möbius, M. Bzowski, J. M. Sokół, M. A. Kubiak, S. A. Fuselier, H. O. Funsten, et al. The downwind hemisphere of the heliosphere: Eight years of IBEX-lo observations. *The Astrophysical Journal*, 851(1):2, 2017.
- Galvin, A. B., L. M. Kistler, M. A. Popecki, C. J. Farrugia, K. D. C. Simunac, L. Ellis, E. Möbius, M. A. Lee, M. Boehm, J. Carroll, et al. The plasma and suprathermal ion composition (PLASTIC) investigation on the STEREO observatories. In *The STEREO Mission*, pages 437–486. Springer, 2008.
- Geiss, J., G. Gloeckler, L. A. Fisk, and R. von Steiger. C⁺ pickup ions in the heliosphere and their origin. *Journal of Geophysical Research: Space Physics*, 100(A12):23373–23377, 1995a.
- Geiss, J., G. Gloeckler, and R. von Steiger. Origin of the solar wind from composition data. *Space Science Reviews*, 72(1-2):49–60, 1995b.
- Gershman, D. J., L. A. Fisk, G. Gloeckler, J. M. Raines, J. A. Slavin, T. H. Zurbuchen, and S. C. Solomon. The velocity distribution of pickup He⁺ measured at 0.3 AU by MESSENGER. *The Astrophysical Journal*, 788(2):124, 2014.
- Gloeckler, G., N. A. Schwadron, L. A. Fisk, and J. Geiss. Weak pitch angle scattering of few MV rigidity ions from measurements of anisotropies in the distribution function of interstellar pickup H⁺. *Geophysical research letters*, 22(19):2665–2668, 1995.
- Gloeckler, G., L. A. Fisk, J. Geiss, N. A. Schwadron, and T. H. Zurbuchen. Elemental composition of the inner source pickup ions. *Journal of Geophysical Research: Space Physics*, 105(A4):7459–7463, 2000a.
- Gloeckler, G., J. Geiss, N. A. Schwadron, L. A. Fisk, T. H. Zurbuchen, F. M. Ipavich, R. Von Steiger, H. Balsiger, and B. Wilken. Interception of comet Hyakutake's ion tail at a distance of 500 million kilometres. *Nature*, 404(6778):576–578, 2000b.
- Gloeckler, G., E. Möbius, J. Geiss, M. Bzowski, S. Chalov, H. Fahr, D. R. McMullin, H. Noda, M. Oka, D. Ruciński, et al. Observations of the helium focusing cone with pickup ions. *Astronomy & Astrophysics*, 426(3):845–854, 2004.
- Gosling, J. T., J. R. Asbridge, S. J. Bame, and W. C. Feldman. Solar wind stream interfaces. *Journal of Geophysical Research: Space Physics*, 83(A4):1401–1412, 1978.
- Gosling, J. T., E. Hildner, R. M. MacQueen, R. H. Munro, A. I. Poland, and C. L. Ross. Direct observations of a flare related coronal and solar wind disturbance. *Solar Physics*, 40(2):439–448, 1975.

- Grün, E., B. A. S. Gustafson, S. Dermott, and H. Fechtig. *Interplanetary dust*. Springer Science & Business Media, 2012.
- Grünwaldt, H., M. Neugebauer, M. Hilchenbach, P. Bochsler, D. Hovestadt, A. Bürgi, F. M. Ipavich, K.-U. Reiche, W. I. Axford, H. Balsiger, et al. Venus tail ray observation near earth. *Geophysical research letters*, 24(10):1163–1166, 1997.
- Heerikhuisen, J., N. V. Pogorelov, G. P. Zank, G. B. Crew, P. C. Frisch, H. O. Funsten, P. H. Janzen, D. J. McComas, D. B. Reisenfeld, and N. A. Schwadron. Pick-up ions in the outer heliosheath: A possible mechanism for the interstellar boundary explorer ribbon. *The Astrophysical Journal Letters*, 708(2):L126, 2009.
- Hefti, S., H. Grünwaldt, P. Bochsler, and M. R. Aellig. Oxygen freeze-in temperatures measured with SOHO/CELIAS/CTOF. *Journal of Geophysical Research: Space Physics*, 105(A5):10527–10536, 2000.
- Hefti, S.: *Solar wind freeze-in temperatures and fluxes measured with SOHO/CELIAS/CTOF and calibration of the CELIAS sensors*. PhD thesis, Universität Bern, 1997.
- Hovestadt, D., M. Hilchenbach, A. Bürgi, B. Klecker, P. Laeverenz, M. Scholer, H. Grünwaldt, W. I. Axford, S. Livi, E. Marsch, et al. CELIAS—charge, element and isotope analysis system for SOHO. In *The SOHO Mission*, pages 441–481. Springer, 1995.
- Isenberg, P. A.: A hemispherical model of anisotropic interstellar pickup ions. *Journal of Geophysical Research: Space Physics*, 102(A3):4719–4724, 1997.
- Janitzek, N. P.: Solar wind heavy ion measurements with SOHO/CELIAS/CTOF. Master’s thesis, Institute of Experimental and Applied Physics, Kiel University, 2014.
- Jian, L., C. T. Russell, J. G. Luhmann, and R. Mz. Skoug. Properties of stream interactions at one AU during 1995–2004. *Solar Physics*, 239(1):337–392, 2006.
- Kaiser, M. L., T. A. Kucera, J. M. Davila, O. C. St. Cyr, M. Guhathakurta, and E. Christian. The STEREO mission: An introduction. *Space Science Reviews*, 136(1-4):5–16, 2008.
- Kaiser, M. L.: The STEREO mission: an overview. *advances in Space Research*, 36(8): 1483–1488, 2005.
- Kallenbach, R., J. Geiss, G. Gloeckler, and R. Von Steiger. Pick-up ion measurements in the heliosphere—a review. *Astrophysics and Space Science*, 274(1-2):97–114, 2000.
- Lee, M. A., R. A. Mewaldt, and J. Giacalone. Shock acceleration of ions in the heliosphere. *Space science reviews*, 173(1-4):247–281, 2012.
- Lepping, R. P., M. H. Acuña, L. F. Burlaga, W. M. Farrell, J. A. Slavin, K. H. Schatten, F. Mariani, N. F. Ness, F. M. Neubauer, Y. C. Whang, et al. The Wind magnetic field investigation. *Space Science Reviews*, 71(1-4):207–229, 1995.

- Lindsay, B. G. and R. F. Stebbings. Charge transfer cross sections for energetic neutral atom data analysis. *Journal of Geophysical Research: Space Physics*, 110 (A12), 2005.
- Mann, I. and A. Czechowski. Dust destruction and ion formation in the inner solar system. *The Astrophysical Journal Letters*, 621(1):L73, 2005.
- McComas, D. J., N. A. Schwadron, F. J. Crary, H. A. Elliott, D. T. Young, J. T. Gosling, M. F. Thomsen, E. Sittler, J.-J. Berthelier, K. Szego, et al. The interstellar hydrogen shadow: Observations of interstellar pickup ions beyond Jupiter. *Journal of Geophysical Research: Space Physics*, 109(A2), 2004.
- McComas, D. J., H. O. Funsten, S. A. Fuselier, W. S. Lewis, E. Möbius, and N. A. Schwadron. IBEX observations of heliospheric energetic neutral atoms: Current understanding and future directions. *Geophysical Research Letters*, 38(18), 2011.
- McComas, D. J., D. Alexashov, M. Bzowski, H. Fahr, J. Heerikhuisen, V. Izmodenov, M. A. Lee, E. Möbius, N. Pogorelov, N. A. Schwadron, et al. The heliosphere's interstellar interaction: No bow shock. *Science*, 336(6086):1291–1293, 2012.
- McComas, D. J., M. Bzowski, S. A. Fuselier, P. C. Frisch, A. Galli, V. V. Izmodenov, O. A. Katushkina, M. A. Kubiak, M. A. Lee, T. W. Leonard, et al. Local interstellar medium: six years of direct sampling by IBEX. *The Astrophysical Journal Supplement Series*, 220(2):22, 2015.
- Möbius, E., D. Hovestadt, B. Klecker, M. Scholer, G. Gloeckler, and F. M. Ipavich. Direct observation of He^+ pick-up ions of interstellar origin in the solar wind. *Nature*, 318(6045):426–429, 1985.
- Möbius, E., D. Rucinski, D. Hovestadt, and B. Klecker. The helium parameters of the very local interstellar medium as derived from the distribution of He^+ pickup ions in the solar wind. *Astronomy and Astrophysics*, 304:505, 1995.
- Möbius, D. Rucinski, M. A. Lee, and P. A. Isenberg. Decreases in the antisunward flux of interstellar pickup He^+ associated with radial interplanetary magnetic field. *Journal of Geophysical Research: Space Physics*, 103(A1):257–265, 1998.
- Möbius, E., Y. Litvinenko, H. Grüwaldt, M. R. Aellig, A. Bogdanov, F. M. Ipavich, P. Bochsler, M. Hilchenbach, D. Judge, B. Klecker, et al. Direct evidence of the interstellar gas flow velocity in the pickup ion cut-off as observed with SOHO CELIAS CTOF. *Geophysical research letters*, 26(20):3181–3184, 1999.
- Möbius, E., M. Bzowski, S. Chalov, H.-J. Fahr, G. Gloeckler, V. Izmodenov, R. Kallenbach, R. Lallement, D. McMullin, H. Noda, et al. Synopsis of the interstellar He parameters from combined neutral gas, pickup ion and UV scattering observations and related consequences. *Astronomy & Astrophysics*, 426(3):897–907, 2004.
- Möbius, E., M. A. Lee, and C. Drews. Interstellar flow longitude from the symmetry of the pickup ion cutoff at 1 AU. *The Astrophysical Journal*, 815(1):20, 2015.

- Oka, M., T. Terasawa, H. Noda, Y. Saito, and T. Mukai. ‘torus’ distribution of interstellar helium pickup ions: Direct observation. *Geophysical research letters*, 29(12), 2002.
- Opher, M., E. C. Stone, and T. I. Gombosi. The orientation of the local interstellar magnetic field. *Science*, 316(5826):875–878, 2007.
- Opher, M., J. F. Drake, B. Zieger, M. Swisdak, and G. Toth. Magnetized jets driven by the Sun: The structure of the heliosphere revisited—updates. *Physics of Plasmas*, 23(5):056501, 2016.
- Pagel, A. C., N. U. Crooker, T. H. Zurbuchen, and J. T. Gosling. Correlation of solar wind entropy and oxygen ion charge state ratio. *Journal of Geophysical Research: Space Physics*, 109(A1), 2004.
- Parker E. N.: The stellar-wind regions. *The Astrophysical Journal*, 134:20, 1961.
- Pizzo, V.: A three-dimensional model of corotating streams in the solar wind, 1. theoretical foundations. *Journal of Geophysical Research: Space Physics*, 83(A12):5563–5572, 1978.
- Quinn, P. R., N. A. Schwadron, and E. Möbius. Transport of helium pickup ions within the focusing cone: Reconciling stereo observations with IBEX. *The Astrophysical Journal*, 824(2):142, 2016.
- Quinn, P. R., N. A. Schwadron, E. Möbius, A. Taut, and L. Berger. Abundance of C⁺/O⁺ inner-source pickup ions produced by solar wind recycling, neutralization, backscattering, and sputtering. *in preparation*, 2018.
- Ratkiewicz, R. and J. Kotlarz. Does the interstellar bow shock exist around the heliosphere? *Prace Instytutu Lotnictwa*, (4 (245)):178–188, 2016.
- Lukas Saul, Peter Wurz, and Reinald Kallenbach. A measurement of the adiabatic cooling index for interstellar helium pickup ions in the inner heliosphere. *The Astrophysical Journal*, 703(1):325, 2009.
- Scherer, K. and H. Fichtner. The return of the bow shock. *The Astrophysical Journal*, 782(1):25, 2014.
- Schwadron, N. A., L. Townsend, K. Kozarev, M. A. Dayeh, F. Cucinotta, M. Desai, M. Golightly, D. Hassler, R. Hatcher, M.-Y. Kim, A. Posner, M. PourArsalan, H. E. Spence, and R. K. Squier. Earth-moon-mars radiation environment module framework. *Space Weather*, 8(1):n/a–n/a, 2010. ISSN 1542-7390. doi: 10.1029/2009SW000523. URL <http://dx.doi.org/10.1029/2009SW000523>. SooEo2.
- Schwadron, N. A. and D. J. McComas. Pickup ions from energetic neutral atoms. *The Astrophysical Journal Letters*, 712(2):L157, 2010.
- Schwadron, N. A., L. A. Fisk, and G. Gloeckler. Statistical acceleration of interstellar pick-up ions in co-rotating interaction regions. *Geophysical research letters*, 23(21):2871–2874, 1996.

- Schwadron, N. A., J. Geiss, L. A. Fisk, G. Gloeckler, T. H. Zurbuchen, and R. von Steiger. Inner source distributions: Theoretical interpretation, implications, and evidence for inner source protons. *Journal of Geophysical Research: Space Physics*, 105(A4):7465–7472, 2000.
- Schwadron, N. A., M. Bzowski, G. B. Crew, M. Gruntman, H. Fahr, H. Fichtner, P. C. Frisch, H. O. Funsten, S. Fuselier, J. Heerikhuisen, et al. Comparison of interstellar boundary explorer observations with 3D global heliospheric models. *Science*, 326(5955):966–968, 2009.
- Schwadron, N. A., E. Möbius, T. Leonard, S. A. Fuselier, D. J. McComas, D. Heirtzler, H. Kucharek, F. Rahmanifard, M. Bzowski, M. A. Kubiak, et al. Determination of interstellar he parameters using five years of data from the IBEX: beyond closed form approximations. *The Astrophysical Journal Supplement Series*, 220(2):25, 2015.
- Shearer, P., R. von Steiger, J. M. Raines, S. T. Lepri, J. W. Thomas, J. A. Gilbert, E. Landi, and T. H. Zurbuchen. The solar wind neon abundance observed with ACE/SWICS and Ulysses/SWICS. *The Astrophysical Journal*, 789(1):60, 2014.
- Stone, E. C., A. C. Cummings, F. B. McDonald, B. C. Heikkila, N. Lal, and W. R. Webber. Voyager 1 explores the termination shock region and the heliosheath beyond. *Science*, 309(5743):2017–2020, 2005.
- Stone, E. C., A. C. Cummings, F. B. McDonald, B. C. Heikkila, N. Lal, and W. R. Webber. An asymmetric solar wind termination shock. *Nature*, 454(7200):71–74, 2008.
- A Taut, L Berger, C Drews, and RF Wimmer-Schweingruber. Composition of inner-source heavy pickup ions at 1 au: Soho/celias/ctof observations-implications for the production mechanisms. *Astronomy & Astrophysics*, 576:A55, 2015.
- Taut, A., L. Berger, C. Drews, and R. F. Wimmer-Schweingruber. Challenges in the determination of the interstellar flow longitude from the pickup ion cutoff. *Astronomy & Astrophysics*, 2018.
- Taut, A.: Pickup ions at 1 AU. Master's thesis, Institute of Experimental and Applied Physics, Kiel University, 2014.
- Taut, A., L. Berger, P. Bochsler, C. Drews, B. Klecker, and R. F. Wimmer-Schweingruber. Observations of the He^+ pickup ion torus velocity distribution function with SOHO/CELIAS/CTOF. In *AIP Conference Proceedings*, volume 1720, page 050001. AIP Publishing, 2016.
- Treumann, R. A. and C. H. Jaroschek. The heliospheric termination shock. *arXiv preprint arXiv:0807.4170*, 2008.
- Tu, C.-Y. and E. Marsch. MHD structures, waves and turbulence in the solar wind: Observations and theories. *Space Science Reviews*, 73(1-2):1–210, 1995.
- Vasyliunas, V. M. and G. L. Siscoe. On the flux and the energy spectrum of interstellar ions in the solar system. *Journal of Geophysical Research*, 81(7):1247–1252, 1976.

- von Steiger, R., N. A. Schwadron, L. A. Fisk, J. Geiss, G. Gloeckler, S. Hefti, B. Wilken, R. F. Wimmer-Schweingruber, and T. H. Zurbuchen. Composition of quasi-stationary solar wind flows from Ulysses/Solar wind ion composition spectrometer. *Journal of Geophysical Research: Space Physics*, 105(A12):27217–27238, 2000.
- Weller, C. S. and R. R. Meier. Observations of helium in the interplanetary/interstellar wind-the solar-wake effect. *The Astrophysical Journal*, 193:471–476, 1974.
- Wimmer-Schweingruber, R. F. and P. Bochsler. On the origin of inner-source pickup ions. *Geophysical research letters*, 30(2), 2003.
- Wimmer-Schweingruber, R. F., R. Steiger, and R. Paerli. Solar wind stream interfaces in corotating interaction regions: SWICS/Ulysses results. *Journal of Geophysical Research: Space Physics*, 102(A8):17407–17417, 1997.
- Witte, M.: Kinetic parameters of interstellar neutral helium-review of results obtained during one solar cycle with the Ulysses/GAS-instrument. *Astronomy & Astrophysics*, 426(3):835–844, 2004.
- Wood, B. E., H.-R. Müller, and M. Witte. Revisiting Ulysses observations of interstellar helium. *The Astrophysical Journal*, 801(1):62, 2015.
- Wu, Co. S. and R. C. Davidson. Electromagnetic instabilities produced by neutral-particle ionization in interplanetary space. *Journal of Geophysical Research*, 77(28): 5399–5406, 1972.
- Xu, F. and J. E. Borovsky. A new four-plasma categorization scheme for the solar wind. *Journal of Geophysical Research: Space Physics*, 120(1):70–100, 2015.
- Ziegler, J. F. and J. P. Biersack. Srim-2008, stopping power and range of ions in matter. 2008.

ERKLÄRUNG

Hiermit erkläre ich, dass die Abhandlung – abgesehen von der Beratung meines Betreuers – nach Inhalt und Form die eigene Arbeit ist und dass die Arbeit unter Einhaltung der Regeln guter wissenschaftlicher Praxis der Deutschen Forschungsgemeinschaft entstanden ist. Die Arbeit oder ein Teil daraus wurde nicht an einer anderen Stelle im Rahmen eines Prüfungsverfahrens vorgelegt.

Kiel, Januar 2018

Andreas Taut

ACKNOWLEDGMENTS

Ich möchte mich zunächst bei meinen Eltern bedanken, die es mir ermöglicht haben, diesen Weg zu gehen. Des Weiteren bedanke ich mich herzlich bei meiner Frau Sonja, die mich die letzten Wochen aushalten musste.

Besonderer Dank gilt Prof. Dr. R. F. Wimmer-Schweingruber für die Möglichkeit, dass ich mich auf diesem Forschungsgebiet entfalten konnte, und die stets gute Betreuung. Durch das stetige kritische Hinterfragen von Dr. Lars Berger und Dr. Christian Drews hat diese Arbeit deutlich an Qualität gewonnen. Außerdem bedanke ich mich herzlich bei Prof. Dr. E. Möbius, Jonathan Bower, und Phil Quinn für die gute Zusammenarbeit und besonders nocheinmal für die Woche in Durham, NH. Aus der Sonnenwindgruppe sind Nils Janitzek, Dr. Verena Heidrich-Meisner, Duncan Keilbach, Dr. Thies Peleikis und Jia Yu hervorzuheben, die erheblich zu dieser Arbeit beigetragen haben. Des Weiteren danke ich Robert Elftmann, Dr. Patrick Kühl, Henning Lohf, Nina & Jan Gieseler und der gesamten ET für eine stets familiäre Arbeitsatmosphäre.

Für eine ausgeprägte Studienzeit und Erholung von der Doktorarbeit danke ich Sebastian Groth, Frederik Woltering, Steven Huth, Dr. Torben Dankwort, Kathleen & Tobias Gehrke und der UT Twee.